Thèse n° 7430

Experimental study of impulse waves generated by viscoplastic fluid

Présentée le 14 décembre 2020

à la Faculté de l'environnement naturel, architectural et construit
Laboratoire d'hydraulique environnementale
Programme doctoral en mécanique

pour l'obtention du grade de Docteur ès Sciences

par

Zhenzhu MENG

Acceptée sur proposition du jury

Prof. W. Curtin, président du jury
Prof. C. Ancey, directeur de thèse
Prof. V. Heller, rapporteur
Dr G. Zitti, rapporteur
Dr G. De Cesare, rapporteur

École
polytechnique
fédérale
de Lausanne

2020

Acknowledgements

First, I would like to thank my supervisor Prof. Christophe Ancey, for his help and support, for trusting me and allowing me to do most work independently. I would also like to offer my sincere thanks to all the members of my jury, Prof. Valentin Heller, Dr. Giovanni De Cesare, and Dr. Gianluca Zitti, for their recommendations to improve this manuscript, and the president of the jury, Prof. William Curtin, for his report on the thesis examination.

Again, I am very grateful to my supervisor Christophe Ancey, without whom I could not have accomplished this PhD thesis. When I arrived at LHE in 2015, I have no experience of experiments and programming, and I almost knew nothing about fluid mechanics. The first year was not easy, but fortunately Christophe was really a good supervisor. He had faith in me and allowed me to continue my research at LHE. I am fortunate to have had such a trusting supervisor, who is not only academically rigorous, but also has an open mind.

I also wish to thank all the members of the LHE, who were always ready to help me: Bob for the technical work; Barbara for her valuable assistance; Thomas, Daniels, Ivans, Yating, Mehrdad, Zhipeng, Gauthier, Kasper, and Blaise for their help and the good atmosphere in the lab. I love the days at LHE, and all of the above-mentioned people were very nice and generous. I also want to thank my students for giving me the opportunity to experience the joy of supervising and teaching. All of their work was important for this thesis.

I would then like to thank my friends for the good times: the skiing or hiking in most weekends during the past years, the experiences of travelling, particularly the impressive travels to Egypt, the tour of Mont Blanc, Andalusia, Provence (including an impressive car crash), Bulgaria, Turkey, and etc. Special thanks to Chenfei, who had helped me get through a difficult time and influenced me greatly.

Finally, I would like to thank my parents for their unconditional love and support. I was far away from them during the years in Europe. As I have came back to China, I look forward to spending more time with my parents in the upcoming years.

Lausanne, November 17, 2020 Z. M.

Abstract

Landslide-generated waves, also called impulse waves, occur as a result of the intrusion of landslides (such as rock falls, debris flows, and avalanches) into bodies of water (such as lakes, reservoirs, and seas). The objective of this thesis was to study the momentum transfer from the slide material to the body of water, in order to develop a better understanding of how the slide material's properties affect the wave generation and to discover alternative modeling approaches to existing empirical equations.

Previous experimental studies have usually used blocks and granular materials to mimic natural landslides. However, many landslides in real worlds have been idealized as viscoplastic fluids in theoretical and numerical studies. No studies have used viscoplastic material in experimental studies of landslide-generated waves. The originality of this thesis lies in the use of a viscoplastic material called *Carbopol Ultrez 10*, an artificial aqueous micro-gel whose rheological behavior can be described using the Herschel-Bulkley model. Carbopol's cohesive and deformable properties are different to both block and granular slides. Further, Carbopol is transparent and can easily be seeded with micro-seeding particles, so its velocity field can be measured using particle image velocimetry (PIV). As a comparison of Carbopol, I also used a granular material named *polymer-water balls* whose density is close to that of Carbopol. The investigations of this thesis are as follows:

- I conducted two series of experiments. First, I observed waves generated by Carbopol, water balls, and mixtures of them using high-speed cameras, to investigate the role of slide material's properties in wave prediction. Second, I conducted PIV experiments with Carbopol to investigate the internal dynamic of slide-water interaction.
- I developed a theoretical model that combined the momentum conservation of two-phase flow in a control volume (Zitti et al., 2016) and viscoplastic theory (Ancey et al., 2012). With the experimental results obtained from PIV measurements, I analyzed the drag force and hydrostatic force that act on stopping the sliding mass, and validated the theoretical model.
- I developed empirical equations using the dimensionless groups that emerged from the governing equations to quantify the wave characteristics (for example, maximum wave amplitude and height) as functions of the slide parameters. Using empirical equations, I compared the characteristics of waves generated by cohesive Carbopol and cohesionless water balls, and discussed the effect of slide cohesion on wave generation.
- Taking advantage of a purely data-driven approach that strictly relies on the dataset and does not need any physical constraints in advance, I applied an *artificial neural*

network method to predict wave characteristics under complex configurations, such as dealing with an experimental dataset with several different slide materials (Carbopol, water balls, and mixtures of them).

- Using a panel data model called *random coefficient model*, I predicted the time series data of wave characteristics from the time series data of slide parameters on impact. Given the slide parameters on impact by the viscoplastic theory, the temporal wave characteristics were quantified from the parameters of the slide material at the initial stage (at rest on the slope and then starting to move).

Keywords: landslide-generated waves, momentum transfer, impulse waves, viscoplastic fluid, Carbopol, granular slide, wave prediction, data-driven approaches.

Résumé

Les vagues générées par glissements de terrain, aussi appelées vagues d'impulsion, sont produites par l'intrusion de glissements de terrain (par exemple chutes de pierres, coulées de débris, avalanches, etc.) dans une étendue d'eau (par exemple lacs, réservoirs, mers, etc.). L'objectif de cette thèse est d'étudier le mécanisme physique régissant l'impact, en particulier le transfert de quantité de mouvement du corps glissant vers l'eau, afin d'obtenir une meilleure compréhension de l'influence des propriétés du matériau glissant sur la formation de la vague et de développer de nouveaux modèles par rapport aux équations empiriques existantes.
Dans les études expérimentales précédentes, les blocs et les matériaux granulaires étaient souvent utilisés pour simuler des glissements de terrain naturels. Toutefois, dans les études théoriques et numériques, de nombreux glissements de terrain sont considérés comme des fluides viscoplastiques. Aucune matériau viscoplastique n'a été utilisée dans l'étude expérimentale des vagues générées par les glissements de terrain. L'originalité de cette thèse réside dans l'utilisation d'un matériau viscoplastique appelé *Carbopol Ultrez 10*, un micro-gel aqueux artificiel dont le comportement rhéologique peut être exprimé par le modèle Herschel-Bulkley. Par rapport aux blocs et aux matériaux granulaires traditionnellement utilisés dans ce genre d'expériences, le Carbopol est cohésif et déformable. De part sa transparence et de sa compatibilité aux microparticules, il est possible de mesurer la dynamique interne et les champs de vitesse du Carbopol et de l'eau pendant l'impact en utilisant la PIV. En plus du Carbopol, j'ai utilisé un matériau granulaire, des *boules d'eau en polymère* dont la masse volumique est proche de celle du Carbopol. Les contributions de cette thèse se résument comme suit :

- J'ai fait deux séries d'expériences : d'abord, j'ai utilisé des caméras à grande vitesse pour observer les vagues crée par Carbopol, boules d'eau et des mélanges de ceux-ci, afin d'étudier le rôle des matériaux des glissières dans la prévision des caractéristiques des vagues. Ensuite, j'ai utilisé PIV pour observer les vagues crée par Carbopol, afin d'étudier la dynamique interne de l'interaction entre l'eau et Carbopol.
- J'ai développé un modèle théorique basé sur les équations de conservation de la quantité de mouvement du matériau glissant et de l'eau, dans lequel le mouvement du matériau glissant a été modélisé avec un modèle viscoplastique. À partir des résultats expérimentaux obtenus par PIV, j'ai analysé la force de traînée et la force hydrostatique qui arrêtent la masse glissante, et puis validé le modèle théorique.
- À l'aide des variables adimensionnels issus de l'analyse dimensionnelle des équations du mouvement, j'ai développé des équations empiriques pour quantifier les

caractéristiques des vagues (par exemple l'amplitude maximale des vagues, la hauteur, et etc) en fonction des paramètres de glissement. J'ai étudié l'influence de la cohésion du matériau glissant sur la génération de vagues, en comparant les caractéristiques des vagues générées par le Carbopol (avec cohésion) et les boules d'eau (sans cohésion) en utilisant des équations empiriques.

- Profitant de l'approche purement statistique qui repose uniquement sur l'ensemble des données et ne nécessite aucune notion physique préalable, j'ai utilisé un approche appelé « artifical neural network » pour prédire les caractéristiques des vagues en configurations complexes, par exemple en prédisant les vagues générées par les matériaux différents (Carbopol, les boules d'eau, et des mélanges de ceux-ci).
- En utilisant un modèle de données de panel appelé « random coefficient model », j'ai prédit des caractéristiques des vagues des séries temporelles à partir des données de séries temporelles des paramètres de glissement à l'impact. En estimant l'épaisseur et la vitesse de glissement au moment de l'impact avec la théorie viscoplastique, j'ai quantifié les caractéristiques des vagues des séries temporelles à partir des réglages de glissement au départ.

Contents

List of Figures

List of Tables

1 Introduction

This chapter details the context of the research topic, the knowledge that previous studies have gathered, the remaining research gaps in the domain, as well as the approaches and strategies adopted by this thesis to fill these gaps.

1.1 Context

Landslides such as avalanches, debris flows, mud flows, glacier calving, and rockfalls are common in mountainous regions and coastal areas. When these masses intrude the surrounded bodies of water (such as mountain lakes, reservoirs, rivers, and oceans), they can generate large impulse waves (also called landslide-generated waves or landslide-tsunamis or landslide-waves) that can have devastating effects.

A typical example of landslide-waves occurred at Lituya Bay, on the southern coast of Alaska, in 1958: an earthquake triggered a major subaerial landslide into the Lituya Bay and the associated waves reached an elevation of 524 m, causing forest destruction and erosion down to the bedrock (Miller, 1960; Fritz et al., 2009). Another example occurred at the Vajont reservoir in Italy in 1963: a block landslide formed an impulse wave that over-topped the dam and swept through two villages downstream of the reservoir, causing 1,910 deaths (Ciabatti, 1964; Genevois and Ghirotti, 2005). An example in Switzerland was a cohesive avalanche that exerted impacts on a lake close to Göschenen in February 1999 (Ammann, 2000). The resulting snow-water mixture flowed out of the lake as a thick viscous fluid, over-topped a 6-m protection wall, and damaged the village structures (see Figure 1.1).

The probability of such events is increasing due to the effects of global warming. A recent example occurred in Lake Askja in Iceland in 2014, where an approximately 20×10^6 m^3 landslide generated a 50 m large wave that inundated the shoreline up to 80 m (Gylfadóttir et al., 2017). Another recent example was a rapid rock avalanche that occurred in 2017 in Greenland, where approximately 50 Mm^3 of slide material impacted the Karrat Fjord and created a wave that propagated 32 km to the village of Nuugaatsiaq (Gauthier et al., 2018;

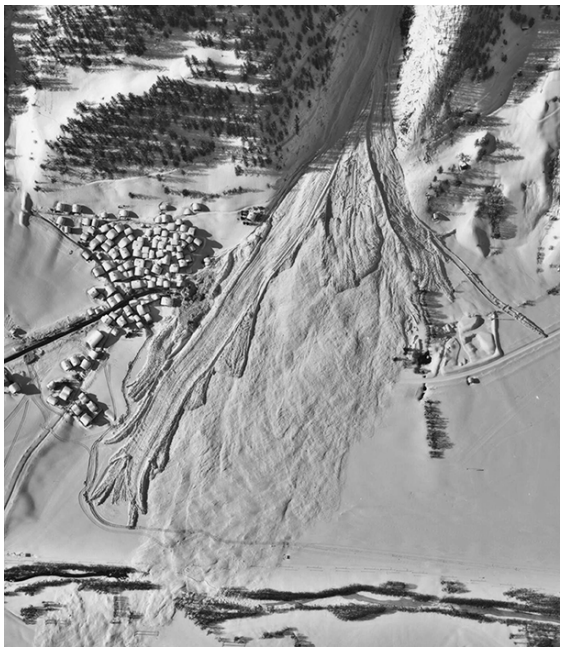

Figure 1.1 – Snow-water mixtures resulting from the intrusion of an avalanche into a lake near Göschinen, Switzerland in 1999 (photo taken from Swiss Federal Topography Agency).

Bessette-Kirton et al., 2017). On a global scale, considering regions such as China with over 80,000 reservoirs, Norway with 1190 fjords, and numerous hydropower project worldwide, it is necessary to predict and evaluate the possible landslides-waves (Liu et al., 2013; Greeman, 2015).

The problem of impulse waves generated by subaerial landslides has attracted considerable attention in recent decades. Many of the physical insights into this phenomena have come from laboratory scale-down experiments (Kamphuis and Bowering, 1970; Huber and Hager, 1997; Fritz, 2002a; Panizzo et al., 2005; Zweifel et al., 2006; Fuchs and Hager, 2015; Heller et al., 2016; Mulligan and Take, 2017; Evers, 2017; Jing et al., 2020), and to a lesser extent from theoretical models (Kranzer and Keller, 1959; Le Méhauté and Wang, 1996; Zitti et al., 2016), numerical simulations (Watts, 1997; Abadie et al., 2010; Zhao et al., 2016; Yavari-Ramshe and Ataie-Ashtiani, 2017; Ruffini et al., 2019), and field data surveys (Fritz et al., 2013; Grilli et al., 2016; Engel et al., 2016; Poupardin et al., 2017).

As illustrated in Figure 1.2, subaerial landslides generating waves can be divided into three phases: (1) the landslide enters the body of water and generates waves; (2) the waves propagate over the body of water; (3) the waves run-up on the opposite shore and, in some cases, over-top the dam (Fritz, 2002a; Heller, 2007). This thesis focuses on the first phase: the formation of the impulse waves as a result of momentum transfer from the sliding mass to the body of water.

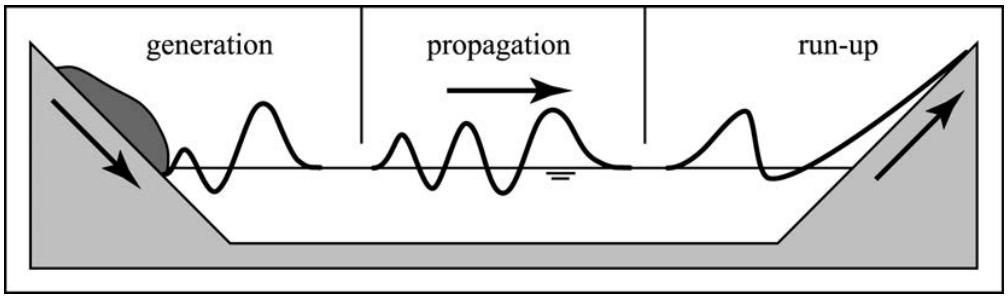

Figure 1.2 – The three phases of impulse waves generated by a subaerial landslide: (1) wave generation, (2) wave propagation, and (3) wave run-up on the opposite shore (Fritz, 2002a).

1.2 Knowledge gaps

1.2.1 Slide materials

The choice of material used for the landslide is a problem that needs to be considered in all experimental studies. Blocks and granular materials have been routinely used for mimicking landslides at the laboratory scale (Fritz, 2002a; Noda, 1970; Kamphuis and Bowering, 1970; Huber, 1980; Huber and Hager, 1997; Viroulet et al., 2013; Heller and Spinneken, 2015; Heller et al., 2016; Tang et al., 2018; Heller et al., 2019). A series of comparisons have been conducted for experiments with different slide materials such as rigid blocks and granular slides (Zweifel, 2004; Ataie-Ashtiani and Nik-Khah, 2008), blocks with different shapes (Heller and Spinneken, 2013), granular slides with different grain diameters (Lindstrøm, 2016), etc. The results indicate that the wave's characteristics depend heavily on the material's properties.

The differences in the characteristics of waves generated by different slide materials have been interpreted as a consequence of material deformability (Yavari-Ramshe and Ataie-Ashtiani, 2016; McFall et al., 2018; Yavari-Ramshe and Ataie-Ashtiani, 2019): by changing the shape of the slide during the impact, a deformable mass would be less prone to impart its momentum to the water. The differences also have been explained with slide porosity (Lindstrøm, 2016), slide mobility (Bullard et al., 2019), etc. One may also suppose that the material's cohesion plays a key part in the momentum transfer from the sliding material to the body of water: a rigid block moves as one element when immersed in water, whereas granular material consists of numerous particles when striking the free surface (Fritz et al., 2004; Meng and Ancey, 2019).

Any hypothesis (either the slide material's deformability, porosity or cohesion dominates the wave generation) on the basis of reliable experimental data is plausible. However, most scientific data could swing the balance of evidence to favor one hypothesis over another. It is difficult to assess the influence of each factor, if one merely works with rigid blocks and granular materials, as the differences between these two materials are manifold; for example, blocks not only retain their shape, but also have infinitely large cohesion, whereas granular materials are deformable and cohesionless. The controversy regrading the effect of slide materials on wave characteristics is not only a tell-tale sign that the physics behind the

slide-water interaction are more complicated than commonly believed, but also urges us to introduce slide materials whose properties are distinguishable from both block and granular materials into experiments rather than trap in an endless loop of comparing between block and granular materials.

To investigate the rheology of gravity-driven flows such as mud flows, debris flows, and avalanches, in addition to granular flows, scientists have developed an analogy with yield-stress fluids (Ancey, 2007); that is, materials that behave like fluids when their stress state exceeds a critical stress called *yield stress* and like solids when they are not sufficiently stressed (Balmforth et al., 2014). The analogy has made it possible to develop flow-dynamics models and run experiments in the laboratory to understand how the material properties (yield stress, viscosity, and if applicable friction) affect the bulk dynamics. Dent and Lang (1983) demonstrated that viscoplastic models such as the Bingham model and the Herschel–Bulkley model approximately describe the flow behavior of snow avalanches flowing down on an inclined flume. Laboratory experiments have also shown the possibility of describing the motion of clay and mud flow by viscoplastic models (Ancey and Cochard, 2009; Andreini et al., 2012; Chanson et al., 2006; Chambon et al., 2014). The analogy has also been regarded as a crude over-simplification of natural gravity-driven flows (Iverson, 1997; Iverson and Vallance, 2001). We will not engage in this debate here.

In the domain of landslide-generated waves, viscoplastic models have been widely used in numerical simulations (Skvortsov and Bornhold, 2007; Bonn et al., 2017; Cremonesi et al., 2011; Zhao et al., 2016), while none has used viscoplastic materials in experiments. Even some numerical studies have modelled the landslide with a viscoplastic model, while their models were validated using experimental data obtained with granular materials. Introducing viscoplastic material into experiments will help us gain a better understanding of the role of slide material's properties in wave generation.

1.2.2 Predicting wave characteristics from slide parameters

Laboratory experiments not only make it possible to shed light on the physical processes that govern the wave generation, but also allow us to quantify how waves' features (such as amplitude and height) depend on the initial conditions (for example, the mass, density, and velocity of the incoming flow). In most earlier studies, these quantitative analyses combined dimensional analysis and non-linear regression techniques (Fritz et al., 2003; Heller, 2007; Heller and Hager, 2014; Zitti et al., 2015; McFall and Fritz, 2017; Mohammed and Fritz, 2012). The studies have occasionally involved a scale analysis of the governing equations (Walder et al., 2003; Fernández-Nieto et al., 2008; Zitti et al., 2016, 2017); for instance, Zitti et al. (2016, 2017) studied how mass and momentum were exchanged between the incoming sliding material flow and the outgoing impulse wave by using a control volume surrounding the impact zone. By scaling the mass and momentum balance equations, they obtained dimensionless numbers that could subsequently be used for correlating wave features with

initial parameters.

For both of the two above-mentioned approaches, the modeling of the wave characteristics mostly relied on empirical equations in the form of power functions of several selected dimensionless parameters that pertained to the momentum flux of the incoming sliding mass. The most commonly used dimensionless parameters include the slide Froude number, the relative slide thickness, and the relative slide mass (Heller and Hager, 2010, 2014). In recent years, more and more parameters were implemented into the predictive equations to predict the wave features under different configurations; these included the grain diameter of granular slides, and the front angle of block slides, the slide width and length. When integrating new parameters into the empirical equations, most researchers chose to presume the functional form as a power function in advance, which well followed the assumptions of previous studies. This functional form usually suited the experimental data well (Mohammed and Fritz, 2012; Bolin et al., 2014; Heller and Spinneken, 2015; McFall and Fritz, 2017). However, the possibility of over-fitting behind the high performance of empirical equations would be largely increased, with more and more parameters included in the equations. We can neither confirm if the presumed functional form is the best fitting one nor verify whether all the selected parameters are necessary.

On many occasions, researchers have developed empirical equations that have fit well with their own experimental data, but these equations then exhibited large deviations from the datasets obtained by other teams, especially when different slide materials were involved in these datasets. The performances of the different equations on a given dataset remain uncertain. This uncertainty reflects the limitations of empirical equations with a given functional form. Heller and Spinneken (2013) developed generic empirical equations for blocks of various shapes, and discussed the data discrepancies between using blocks and granular slides. In fact, none of the existing empirical equations can account for the full range of materials used in experiments. Applying empirical equations may be difficult when, for instance, the slide material involves different components. A typical example is Tang et al. (2018), who conducted experiments using blocks, granular slides, and a mixture of block and granular slides. The representative parameters of blocks and granular slides were the aspect ratio and the grain diameter, respectively. Without knowing how these two materials interact with the body of water, integrating these two parameters into one equation might be problematic if we have presumed a functional form for that equation in advance. For more complex landslide materials, providing physical constraints on the mathematical operators of prediction equations formulation of empirical equations becomes more challenging. This creates the need to develop predictive models that do not to need presume the functional from in advance and have high adaptabilities to cope with complex configurations.

Another interesting issue is that no studies have yet examined how the time series data of wave characteristics depend on the slide parameters. All previous predictive equations have focused on the relation between the slide parameters at impact and the maximum values of wave characteristics. The momentum transfer between the sliding mass and the body of water

lasts from the point at which the front of the slide material touches the shoreline until the point at which the slide stops moving. Miller et al. (2017) demonstrated that only the frontal part of the slide mass, rather than the whole slide mass, is involved in the wave generation, showing the need to consider the impacting time and the time series relation between the slide features and wave characteristics. A recent experimental study measured the time series data of the slide's thickness and velocity passing through the shoreline (Bullard et al., 2019). There remains a gap in how the temporal wave characteristics depend on the time series data of slide parameters.

1.2.3 Experimental difficulties

One laboratory challenge is to measure the internal velocities of the sliding mass and the water body during the intrusion of the slide; this is important for understanding the physical mechanism governing the slide-water interaction and for building the time series relation between the wave characteristics and slide features. Using PIV, Fritz (2002b) measured the near-field velocity field of the body of water during the intrusion of granular slides. PIV is a laser optical measurement technique that can be used to measure the velocity field of an entire region within a flow (Santiago et al., 1998). The major difficulty in measuring water's velocity field during the impact came from the reflective index differences between air and water. As observed from laboratory experiments, when granular particles entered the body of water, a large amount of air bubbles intruded into the water body along with the slide particles (see Figure 1.3). As the reflective index of air is different from that of water, the reflections from the surface of the air bubbles made it arduous to trace the motion of seeding particles in water.

Further, the velocity field of the submerged slide material is lacking to date, due to the difficulty of finding a slide material that is transparent and can be traced using PIV. Previous studies have approximated the velocity of the slide material by its frontal velocity passing through the shoreline. It was logical to assume that the block slide passing through the shoreline at a constant velocity. Yet, for slide material that behaves like a long and thin train of material (such as granular slides and viscoplastic slides), the velocity at shoreline was found to vary with time (Bullard et al., 2019).

1.3 Objectives

This thesis provides insights into impulse waves generated by viscoplastic fluid. The thesis objectives are as follows:

- Analyze the effect of slide material's cohesion on wave generation by comparing characteristics of waves generated by viscoplastic and granular slides.
- Develop a theoretical model for viscoplastic fluid interacting with water, based on the

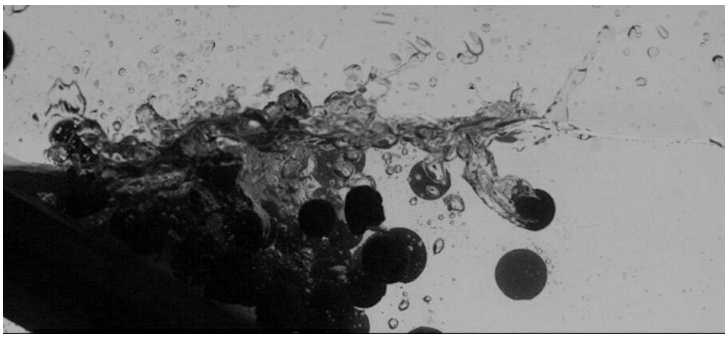

Figure 1.3 – The intrusion of granular particles into water.

mass and momentum conservations of two-phase flow in a control volume and the viscoplastic theory.

- Develop a predictive model that is adaptable to an experimental dataset with several different slide materials (for example, viscoplastic material, granular material, and mixtures of them).
- Quantify the temporal wave characteristics from the time series data of slide parameters.

1.4 View of approaches taken in this thesis

With the objectives in mind, I conducted experiments using a viscoplastic material called Carbopol, and observed the internal dynamic of how submerged Carbopol interact with the water body with the support of the PIV technique. The analysis of how the wave characteristics depend on the slide parameters relied on a theoretical model and two data-driven approaches.

1.4.1 Slide materials and experimental method

Carbopol Ultrez 10 is an artificial aqueous micro-gel whose rheological behavior can be described using the Herschel-Bulkley model (Contreras et al., 2001; Fresno et al., 2002, 2001). In recent years, it has been increasingly used to mimic landslides over a wide range of shear rates in various studies, such as standard rheological measurements, channel configurations, and more complex hydrodynamics such as gravity-driven flows and fingering instabilities (Bonacucina et al., 2004; Freydier et al., 2016; Luu et al., 2015; Møller et al., 2006). Using Carbopol, the Environmental Hydraulic Laboratory (LHE) at EPFL has conducted a number of experimental studies on several topics, such as dam break problems (Cochard and Ancey, 2009), internal dynamics of flowing viscoplastic fluid (Andreini et al., 2012), and physical entrainment problems (Bates et al., 2016; Ancey and Bates, 2017; Bates and Ancey, 2017).

The present thesis introduced Carbopol into experimental study of landslides-generated waves. For comparison purposes, a granular material called *polymer-water balls* was used.

The densities of both Carbopol and water balls were lower than that of most natural landslides and close to that of water (about 1000 kg·m^{-3}). Previous studies have shown that the material density may influence wave features, especially when the slide penetrates the body of water at a low Froude number (Zitti et al., 2016). Independently of this, it would have been difficult to find materials with the same properties as water balls and Carbopol, but with higher densities.

One advantage of Carbopol is its cohesive and deformable properties, which are distinguishable from both block and granular materials, and can serve to study the effect of the slide cohesion on wave generation. Another advantage is that Carbopol is transparent and can be easily seeded with tracing particles without changing the rheological properties, so that its internal velocity can be measured using PIV. Further, in contrast to granular materials that separate into numerous particles once immersed into water, Carbopol moves as a whole. The quantity of air bubbles induced by the intrusion of Carbopol are fairly small compared with granular slides, so the noises due to air bubbles when measuring water's velocity are greatly reduced.

In addition to record the impacting process using high-speed cameras, the PIV system was built in our laboratory. Using Carbopol as the slide material, I measured the near-field velocity fields of both the submerged slide and the body of water. With the experimental results obtained from PIV, the interaction forces between the slide material and the body of water were determined, and the momentum variations of the slide and water were analyzed.

1.4.2 Wave characteristics analysis

A theoretical model for viscoplastic fluid interacting the body of water was developed in this thesis. I first revisited the governing equations developed by Zitti et al. (2016), which was based on the mass and momentum conservations of two-phase flow in a control volume. The slide thickness and velocity at the left boundary of the control volume were given by the lubrication model and kinematic wave model (Ancey and Cochard, 2009; Ancey et al., 2012). Using the dimensionless groups extracted from the momentum conservation equations, empirical equations in the form of power functions were developed. Using these empirical equations, the characteristics of waves generated by Carbopol and water balls were compared, which quantified the effect of slide cohesion on wave generation.

With increasingly complex configurations and slide materials involved in experiments, it becomes challenging to provide physical constraints on the mathematical operators of empirical equations. It would be preferable to use an approach that did not assume the functional form of the equation in advance and relied strictly on the data alone. Considering the high adaptabilities of data-driven approaches (Panizzo et al., 2005), I applied an artificial neural network (ANN) method to cope with complex configurations that run into difficulty when modelled using empirical equations: (i) predicting wave features from subaerial landslide parameters at their initial stage (with the mass beginning to move down the slope) rather than from the parameters at impact; and (ii) predicting waves generated by different

slide materials, specifically, viscoplastic slides, granular slides, and viscoplastic–granular mixtures. Unlike empirical equations, in which mathematical dependence was fixed in advance, the ANN method provides an approach in which both the explanatory and explained variables in the data ultimately define their internal relationship without any prior assumptions about the equation's functional form or physical constraints. Moreover, the model can be easily calibrated when new data or parameters become available, which makes it powerful in terms of solving complex problems.

In addition to predicting the maximum values of wave characteristics from the slide parameters on impact, we quantified the temporal wave amplitude and height from the momentum flux of the sliding mass (that is, time series data of the slide velocity and thickness passing through the shoreline) using a panel data model. Assuming the incoming landslide as a viscoplastic fluid, the time evolutions of the depth-averaged velocity and thickness of the sliding mass were estimated from the initial slide parameters using the lubrication model and kinematic wave model. Combining the panel data model with the viscoplastic theory, we estimated the time series data of wave characteristics from the landslide parameters at their initial stage when the mass beginning to move down the slope.

1.5 Thesis layout

The thesis is structured as follows:

- Chapter 2 presents the physical model of the problem and the experimental method.
- Chapter 3 displays the modeling approaches including a theoretical model, an artificial neural network method, and a panel data model.
- Chapter 4 studies the effect of slide material's cohesion on wave characteristics, by comparing features of waves generated by Carbopol and water balls using empirical equations. The artificial neural network model is then used to cope with complex configurations, including predicting wave characteristics when the experimental dataset consists of several different slide materials.
- Chapter 5 exhibits the results of the PIV experiments, including the interaction forces between the slide phase and the water phase, and the momentum variations of the two phases. The theoretical model is validated with the experimental results. The time series data of wave characteristics are predicted with the slide parameters using a random coefficient panel data model.
- Chapter 6 outlines the concluding remarks of the thesis.

2 Experimental methods

This chapter presents the methods used for the two-dimensional experimental investigation. Section 2.1 illustrates the simplified physical model of the impacting process. Section 2.2 introduces the two slide materials used in experiments: a viscoplastic material called *Carbopol* and a granular material called *water balls*. Section 2.3 presents the experimental instrumentations including the flume, the high-speed cameras, and the particle image velocimetry (PIV) system. Section 2.4 discusses the experimental settings and scale effects. Section 2.5 shows how the images recorded from the experiments are processed.

2.1 Physical model

Figure 2.1 illustrates the two-dimensional physical model of a landslide moving down a slope and intruding into a body of water. The whole process can be divided into three stages. In the first stage, the slide is at rest in the container box, and then it starts moving. In the second stage, it moves down the slope and reaches the shoreline. In the third stage, it enters the body of water and generates waves.

We consider a slope with an inclination of θ entering a horizontal flume filled with water. The still water depth is denoted by h_0, and the water density is denoted by ρ_f. A coordinate system (x, y) is defined with its origin located at the shoreline, with the x-axis proceeding out across the water, stream-wise, and the y-axis pointing directly upward.

A slide mass, with volume of V_I and density of ρ_s, is released at a distance l_s from the shoreline. The slide's initial shape is idealized as a trapezoid limited by a height of s_g and length of l_0 with the top surface parallel to the free water surface. When the sliding mass moves down the slope, its thickness $s(l, t)$ and depth-averaged velocity $u(l, t)$ vary as a function of l and t. The volume of the immersed slide is denoted by V_s. The free water surface $\eta(x, t)$ depends on the horizontal coordinate x and time t. The wave created by the incursion of the sliding mass is mainly evaluated quantitatively by its height h and amplitude a. The gravity acceleration is denoted by g.

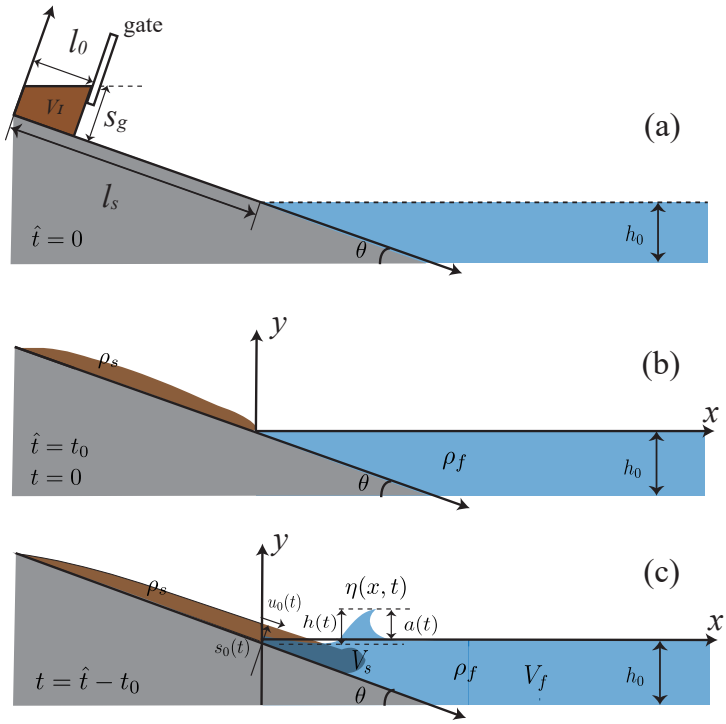

Figure 2.1 – Sketch of the physical model.

2.2 Slide materials

We used two slide materials with the same density: one was an artificial viscoplastic material called Carbopol Ultrez 10; another was granular slide called polymer-water balls (see Figure 2.2).

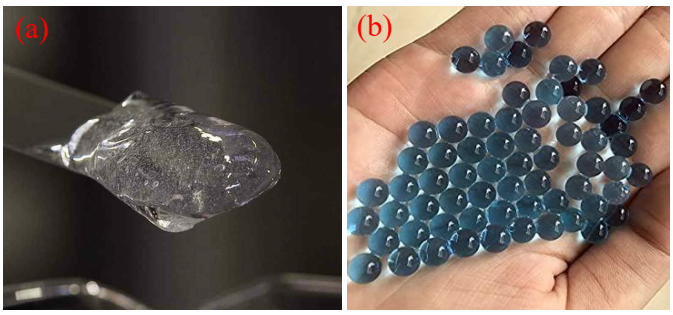

Figure 2.2 – Photos of (a) Carbopol and (b) polymer-water balls.

The rheological behavior of Carbopol gels can be described using the Herschel-Bulkley model, whose expression for simple-shear flows is:

$$\tau = \tau_c + \mu \dot{\gamma}^n \tag{2.1}$$

where τ_c is the yield stress (that is, the stress threshold below which the material behaves like a solid and above which it flows like a fluid), $\dot{\gamma}$ is the shear rate, μ is the consistency and n is a power-law index that reflects shear thinning (or shear thickening when $n > 1$) (Balmforth et al., 2007; Bonn et al., 2017). We conducted the rheological measurements using a Bohlin Gemini rheometer equipped with striated parallel plates (diameter: 25 mm, gap size: 1 mm). The Herschel-Bulkley equation was fitted with these measurements. Table 2.1 shows the rheological parameters τ_c, μ, n of the Carbopol gels used in this thesis. The rheological behavior of Carbopol depended on its concentration c: the yield stress τ_c increased as a power-law function of c (see Figure 2.3).

Table 2.1 – Rheological characteristics of Carbopol used in this thesis

c [%]	Ultrez 10 [g]	NaOH [g]	H_2O [L]	τ_c [Pa]	μ [Pa · s^n]	n [-]
1.5	45	18.0	30	38	10.3	0.289
1.6	50	20.7	30	43	12.3	0.293
1.7	53	22.0	30	49	14.4	0.295
1.8	55	22.8	30	53	16.2	0.315
1.9	58	24.0	30	55	17.1	0.321
2.0	60	24.9	30	58	18.9	0.330
2.1	62	25.9	30	59	19.2	0.331
2.2	65	26.9	30	60	19.8	0.333
2.3	68	28.2	30	65	23.2	0.339
2.4	70	29.0	30	68	24.6	0.348
2.5	75	31.0	30	74	29.1	0.364
2.6	75	32.1	30	75	30.9	0.387
2.7	80	33.2	30	78	32.1	0.388
2.8	85	35.0	30	80	35.8	0.390
2.9	85	36.1	30	83	38.9	0.391
3.0	90	37.3	30	85	42.1	0.392

To produce Carbopol gels, first, the powder of Carbopol Ultrez 10 was poured into demineralized water heated at 50 – 70°C, and the dispersion was left to rest for a few hours. The pH was adjusted by adding a sodium hydroxide solution. See Cochard (2007) for further information. As the powder density was close to that of water, the resulting gel density was approximately 1000 kg m^{-3}, regardless of its concentration c.

For the granular material, we used polymer-water balls that were approximately 15 mm in diameter. To create the water balls, we soaked initially dry beads of a water-absorbent polymer in water. After about four hours, the beads had swelled into balls with a density very close to that of water. Excess liquid was finally removed by draining the balls.

The densities of these two materials were close to 1000 kg m^{-3}, which is lower than that of the usual materials involved in debris flows or rockfalls (over 2000 kg m^{-3}), but similar to that of ice (910 kg m^{-3}). Zweifel (2004) found that buoyancy plays a crucial role in the momentum transfer of slides with low densities when Fr < 2. Zitti et al. (2016) also found that low-density

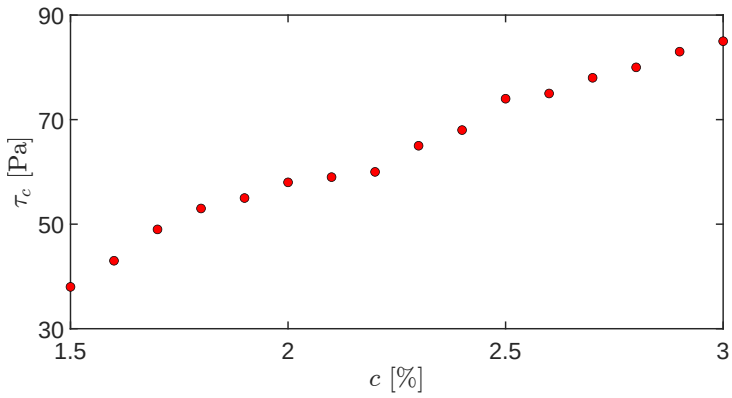

Figure 2.3 – The concentration of Carbopol c versus its yield stress τ_c.

avalanches generated impulse waves whose amplitudes were half as large as those created by high-density avalanches. As it is difficult to find materials with rheological properties similar to those of Carbopol gels and polymer-water balls, but with higher densities, we were unable to test density effects.

2.3 Experimental facilities

I conducted two series of experiments. One was performed with high-speed cameras (non-PIV experiments), which recorded the fluctuation of the water surface and the slide parameters on impact. The other was performed with PIV, which observed the internal motion of the slide-water interaction. For slide materials of the non-PIV experiments, I used Carbopol, water balls, and mixtures of them. For the PIV experiments, only Carbopol was used as the slide material.

2.3.1 Flume

Experiments were conducted in a two-part, two-dimensional flume (see Figure 2.4 (a) and (d)) located in a temperature- and humidity-controlled room. The first part was a chute, 1.5 m long and 0.12 m wide, which could be tilted at angles θ, ranging from 30° to 50°. Its bottom was lined with sandpaper (P180) whose mean surface roughness $R_a = 27.28$ μm. The side walls of the slope were made of PVC. The second part was a water-filled, transparent, glass-sided flume, 2.5 m long, 0.4 m deep and 0.12 m wide. The body of water was backlit using a light panel placed parallel to the rear of the flume. The slide material was initially contained in a box located at the chute entrance, closed by a locked gate 0.2 m high and 0.12 m wide. This gate could be opened in less than 0.1 s owing to two pneumatically-driven pistons. The distance from the gate to the shoreline ranged from 0.5 m to 1.5 m. Once released, the material accelerated energetically under gravity and reached velocities as high as 2.5 m/s. A 0.2×0.4 m^2 mesh grid was used to calibrate the raw images and determine the size conversion factor between the images and the real world.

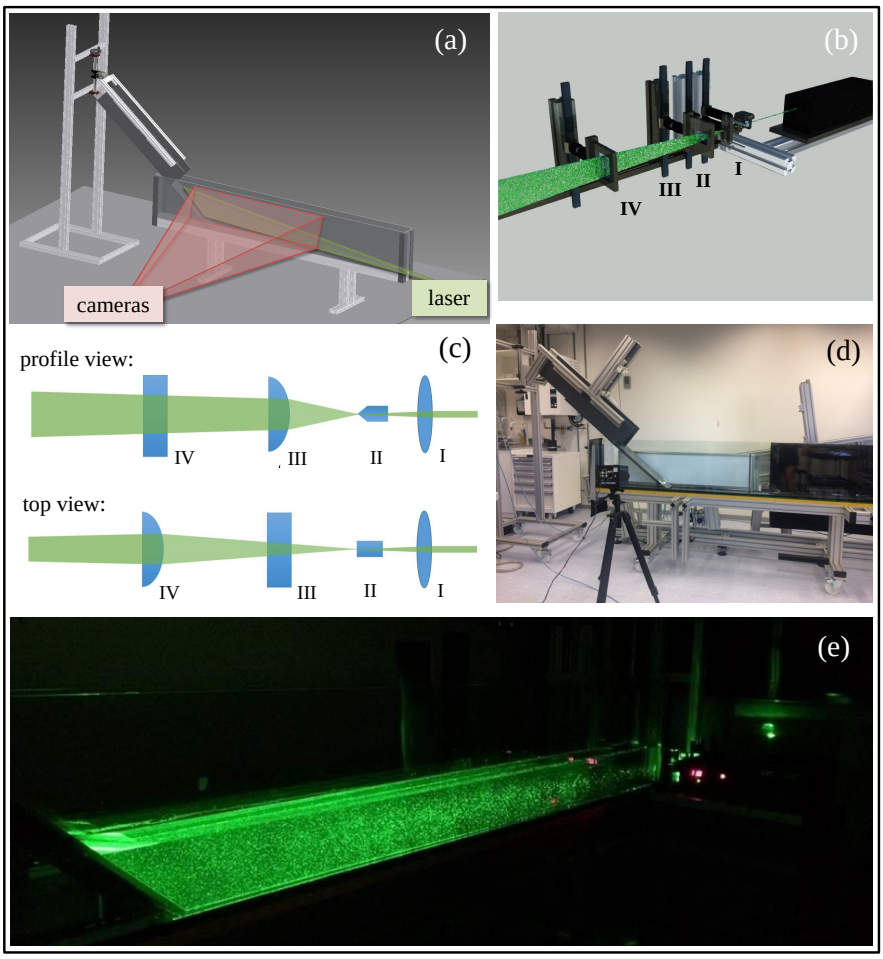

Figure 2.4 – (a) Sketch of the facilities, (b) settings of the laser and the lenses (I denotes a circular lens, II is a laser line generator lens, III is a rectangular lens, IV is an oblong lens), (c) optical design of the laser illumination, (d) photo of the facilities in the lab, and (e) photo of the operating PIV device.

2.3.2 High-speed cameras

Two high-speed cameras were placed in front of the shoreline with their optical axis perpendicular to the side-wall (see Figure 2.4 (a)). A black-and-white camera with a frequency of 400 frames per second (fps) and a resolution of 1280 × 1024 pixels was used to record the motion of water. A color camera with the same frequency and with a resolution of 600 × 800 pixels was used to record the motion of the sliding mass. For the experiments with high-speed cameras (non-PIV experiments), each experiment was repeated twice. I first colored the slide material by Methylene blue and recorded the motion of the submerged sliding mass using the color high-speed camera. I then repeated the experiment with the same controlled variables while coloring the water body by Methylene blue, and then recorded the wave formation using the black-and-white camera. Figure 2.5 shows an example of raw images observed with the high speed cameras. The initial settings of the selected test were: the concentration of

Carbopol $c = 2.5\%$, the slope length $l_s = 0.85$ m, the slope angle $\theta = \pi/4$, the initial slide mass $m_I = 4.0$ kg, and the still water depth $h_0 = 0.2$ m.

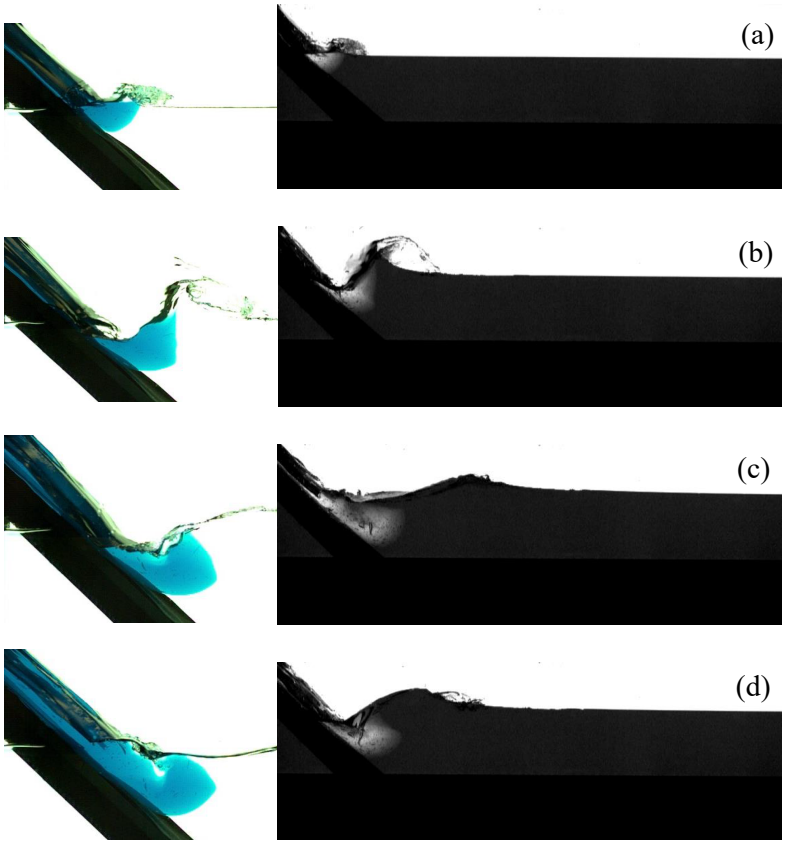

Figure 2.5 – Raw images of Carbopol intruding the body of water recorded by high-speed cameras: (a) $t = 0.1$ s, (b) $t = 0.2$ s, (c) $t = 0.3$ s, and (d) $t = 0.4$ s.

2.3.3 Particle Image Velocimetry

Figure 2.6 displays the principle of the PIV measurement. The particle-seeded flow was illuminated in a target area with a light sheet, and the velocity vectors were derived from sub-sections of the target area by measuring the movement of seeding particles between two image frames. I only used Carbopol as the slide material in PIV experiments. I was unable to trace the interaction between water balls and water with the current PIV setup, due to the effect of air entrainment (see section 1.2.3). The water body was seeded by poly-amides seeding particles with a diameter of 50 μm, and Carbopol was seeded by fluorescent seeding particles with a diameter of 20 μm. The fluorescent seeding particles were produced with poly-amide seeding particles and Rhodamine B dye in the laboratory (see Müller et al. (2013) for details).

The PIV system consisted of a laser, four lenses, and two high-speed cameras (see Figure 2.4

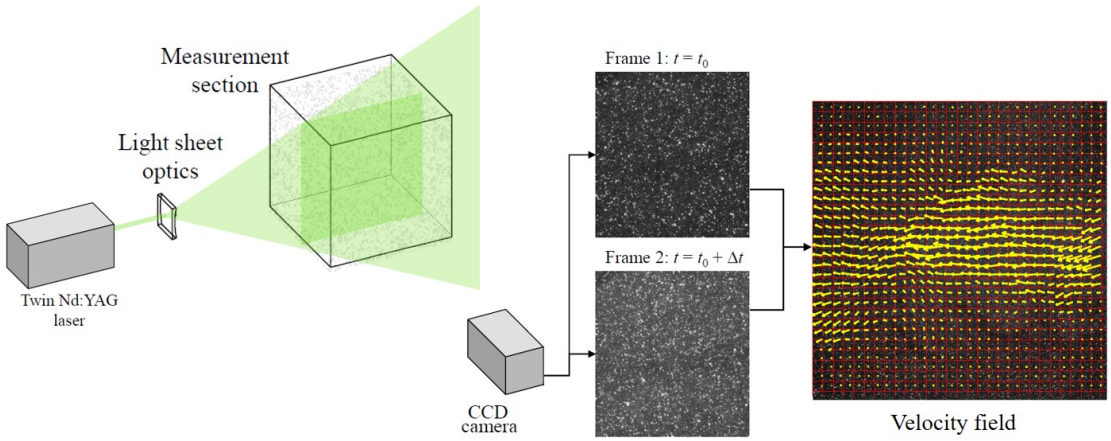

Figure 2.6 – The principle of the PIV measurement.

(a) and (b)). The same cameras were used as in the non-PIV experiments. The laser generated a green laser beam with a wavelength of 527 nm, a maximum output of 150 W, and a pulse duration of 100 ns/CW. As shown in Figure 2.4 (b) and (c), the laser beam first passed a circular lens (I) with a focal length of d = 90 mm; it then passed through a laser line generator lens (II) with a divergence angle of 30° and became a laser sheet; afterwards, the laser sheet passed through a rectangular lens (III) with a focal length of d = 200 mm in the vertical direction; finally, it passed by an oblong lens (IV) with a focal length of d = 1.5 m in the horizontal direction. Figure 2.4 (e) exhibits the operating PIV system.

2.4 Experimental settings and scale effects

As shown in Table 2.2, for non-PIV experiments (i.e., experiments using high-speed cameras), we conducted experiments using Carbopol with concentrations ranging from 1.5% to 3.0%, water balls, and mixtures of them (20% Carbopol + 80% water balls, 80% Carbopol + 20% water balls, 50% Carbopol + 50% water balls). For PIV experiments, we only used Carbopol with a concentration of 2.0% as the slide material.

Table 2.2 – List of materials used in the present study.

Experimental technique	Materials	Number of tests
Non-PIV experiments	Carbopol	291
	20% Carbopol + 80% Water balls	35
	50% Carbopol + 50% Water balls	35
	80% Carbopol + 20% Water balls	35
	Water balls	65
PIV experiments	Carbopol	92

In this thesis, the still water depth h_0 was fixed at 0.2 m. As the slide material was initially

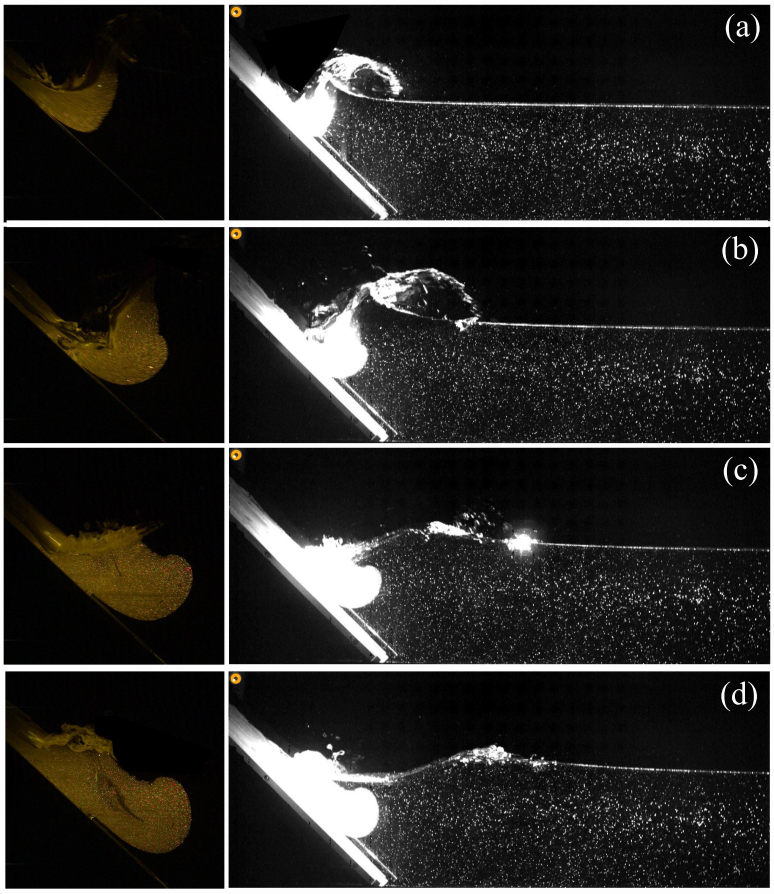

Figure 2.7 – Raw images of Carbopol (left) and water (right) observed from the PIV measurement: (a) $t = 0.1$ s, (b) $t = 0.2$ s, (c) $t = 0.3$ s, and (d) $t = 0.4$ s.

contained in a box located at the chute entrance and accelerated under gravity, both the parameters of the slide material on impact were controlled by varying slope length l_s, slope angle θ, and initial slide mass m_I. The initial slide mass m_I ranged from 2.0 to 5.8 kg for Carbopol, 0.5–5.0 kg for Carbopol-water balls mixtures, and 0.2–3.5 kg for polymer-water balls. The slope lengths l_s ranged from 0.85 to 1.05 m. The slope angle θ ranged from $\pi/6$ to $\pi/4$. The maximum slide velocity on impact u_0 was 2.5 m/s. Slide thicknesses on impact s_0 ranged from 2 to 5 cm.

The scale factor between the experimental set-up and the real-world scenarios was approximately $\lambda_L \sim 100$. The set up was originally devised to mimic landslides striking into a body of water. The main parameters representing the motion of a landslide such as avalanche include volume of the slide, flow depth (also called thickness), and velocity. The mechanism governing the generating wave process is the momentum transfer from the frontal part of the sliding mass to the water body. Hence, the dominant factors controlling the slide-water interaction for the slide part involve its height and frontal velocity. Taking avalanches as an example, the velocity of many avalanches in the natural world ranges from 5 to 25 m/s, and

the height of a large avalanche typically ranges from 2 to 5 m. In our experiments, the slide thickness at impact ranged from 0.02 to 0.05 m ($\lambda_L \sim 100$), and the frontal velocity ranged from 0.5 to 2 m/s ($\lambda_V = \lambda_L^{0.5} \sim 10$). The diameter of water balls was 15 mm, corresponding to big rock avalanches with a diameter of 1.5 m. The still water depth was held at 0.2 m in experiments, representing a water basin with a depth of 20 m in real-world with the scale factor $\lambda_L \sim 100$. There was a fairly good match between experiments and real scenarios. As presented in section 2.2, the densities of Carbopol and the water balls (about 1000 kg/m^3) are lower than most natural landslides, and close to that of ice. As it is difficult to find materials whose rheological properties are similar to those of Carbopol gels and polymer-water balls, but with higher densities, we were unable to test density effects.

Physical modeling of impulse waves is commonly based on the Froude similitude. If the model dimensions applied are too small, scale effects may arise as a consequence of surface tension in the impact zone and fluid viscosity. The influence of surface tension on wave dynamics can be assessed using the Weber number We= $\rho_f g h_0^2/\sigma_f$ and the fluid viscosity effects can be estimated using the Reynolds number Re= $g^{1/2} h_0^{3/2}/\mu_f$. As Re > 3000,000 and We > 5000 in our experiments, the scale effects resulting from surface tension and fluid viscosity are negligible for the slide impact zone. Further, as h_0 = 0.2 m and 0.38 s < T < 2.24 s in our experiments, we think that the disrupting effect of surface tension was not a confounding factor during the wave propagation (Heller et al., 2008). To avoid significant scale effects using scale series, the slide Froude number Fr, scaled slide mass M and scaled slide thickness S are identical between the prototype and the real scenarios. In our experiments, the dimensionless parameters are controlled in the ranges as follows: the slide Froude number 0.05 < Fr < 2.78, the scaled effective mass 0.03 < M_E < 0.33, and scaled slide thickness 0.12 < S < 0.25 (see the details in section 3.1.3).

In addition, a laboratory-numerical approach is used to quantify scale effects in relation to the slide. Numerical simulation using Gerris shows excellent agreement with the laboratory experiment for slide frontal velocity, and the simulation with *Gerris* did not capture any scale effect at a scale range from λ = 0.5 to λ = 2 compared to the experimental scale. With regard to the side wall effect, the flow front of the Carbopol in our experiments is relatively flat, suggesting that the slump is largely two dimensional and the side wall does not have much effect (Balmforth et al., 2007).

2.5 Image processing

2.5.1 Images recorded with high speed cameras

For each image, we measured (1) the position of the free surface when the leading wave reached its maximum amplitude, (2) the velocity and thickness of the sliding mass upon impact, and (3) the mass of the slide's immersed part. To that end, we first located the interface between the water and surrounding air for each image (see Figure 2.8 (a)). We then deduced

the time variation of the wave features including the wave height and amplitude from the position of the free water surface. To estimate the velocity of the sliding mass on impact, we tracked its front during its course down the chute. The front's velocity was averaged over a time length $\delta t = 0.03$ s (6 frames). The slide material's thickness was defined as the mean thickness in the observation window. For polymer-water balls, we defined an effective immersed volume by integrating the flux of particles (crossing the water interface) over time. For the Carbopol and mixtures of Carbopol and water balls, we first extracted the interface between the sliding material and the surrounding water (see Figure 2.8 (b)), and then measured the immersed part's volume by counting the number of its pixels in the image.

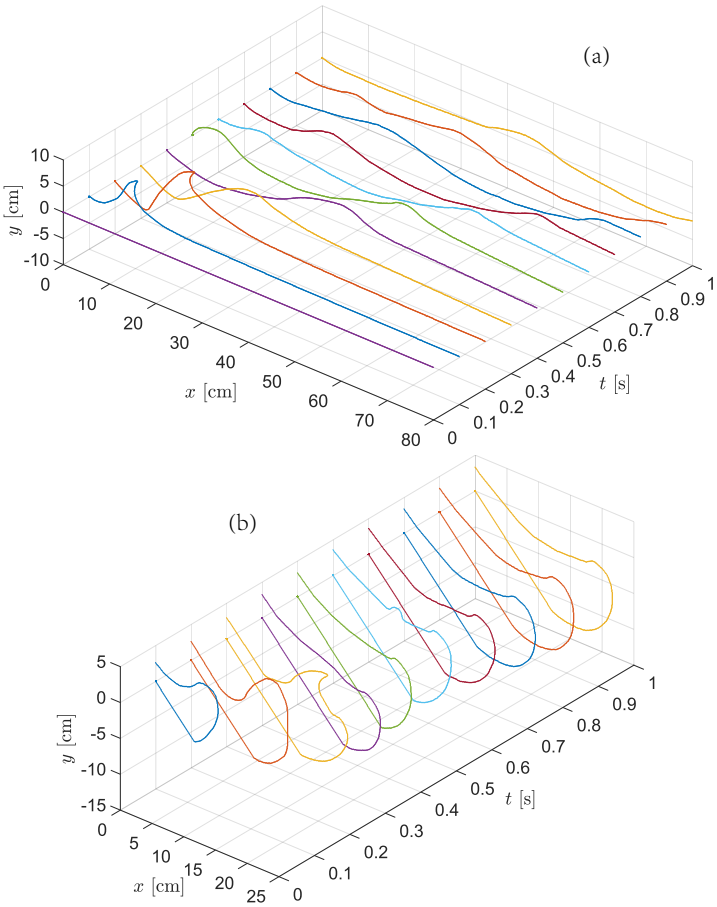

Figure 2.8 – Evolution of the (a) free water surface and (b) slide-water interface from $t = 0.1$ s to 1.0 s. Initial settings of the selected test were the same as those of Figure 2.5.

Open-channel flows of viscoplastic material are subjected to side-wall effects, which explains why the measurements along the centerline are not fully representative of the whole flow. To quantify how the position of the laser plane affects the measurements error, we lit five equispaced parallel cross-sections and compared the wave and slide features under these measurement planes. From this comparison, we deduced that the error was negligibly small (less than 1%). The maximum uncertainties in the image processing were 0.18 mm/s for

the sliding mass' velocity on impact, 0.9 mm for the free surface position and slide material thickness, and 20 g for the immersed mass. I conducted reproducibility tests and found that the observations can be reproduced closely from one to the next, for example, within 2 pixels for the free surface for both PIV and non-PIV experiments.

2.5.2 Images recorded with PIV

In addition to the slide and water parameters extracted from non-PIV experiments, PIV experiments provided velocity fields of the slide and the near-field water body. With the velocity fields, we estimated (1) the depth-averaged velocity of the sliding mass passing through the shoreline, and (2) the momentum of the submerged sliding mass and water body in the observation window.

Using a toolbox in Matlab named *Mat*PIV, the velocity fields were determined from images recorded with PIV. We used a 32 × 32-pixel interrogation windows and 50% overlap between adjacent windows. To remove the spurious velocity vectors, a range validation filter was used, i.e., all the velocity vectors larger than 3 m/s were discarded. Using a moving average validation filter, the velocity vectors that deviate 15% from the average value of its surrounding 3 × 3 vectors fields was substituted by interpolation. The velocity vectors were converted into the velocities by calibrating the physical size of a pixel in an image. Figure 2.10 and 2.9 display the velocity fields of the submerged slide and the near-field water body, respectively. The initial settings of the selected test were the same as those of Figure 2.5. The momentum was calculated by integrating the velocity at each interrogation window. The slide's depth-averaged velocity passing through the shoreline was estimated by the average velocity of the interrogation windows near the shoreline.

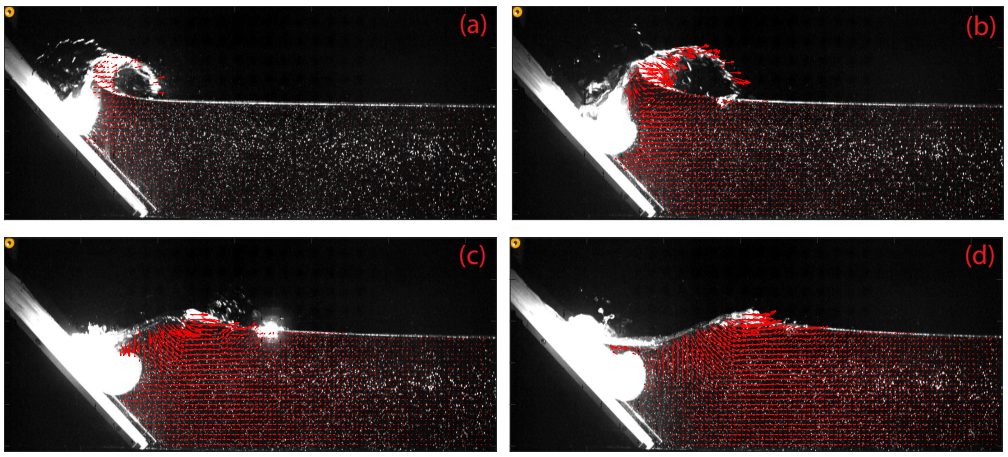

Figure 2.9 – Velocity fields of the body of water at: (a) $t = 0.1$ s, (b) $t = 0.2$ s, (c) $t = 0.3$ s, and (d) $t = 0.4$ s.

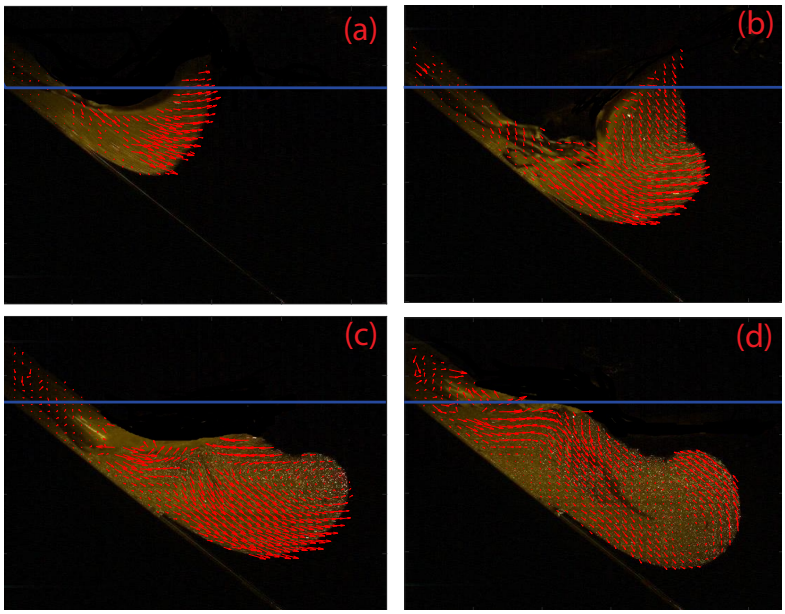

Figure 2.10 – Velocity fields of the submerged sliding mass at: (a) $t = 0.1$ s, (b) $t = 0.2$ s, (c) $t = 0.3$ s, and (d) $t = 0.4$ s. The blue line indicates the position of the free water surface.

3 Modeling

This chapter presents the modeling approaches used in this thesis including a theoretical model and two data-driven methods. Section 3.1 presents the theoretical model, which expressed the momentum transfer between an incoming viscoplastic flow and a body of water. Section 3.2 presents the data-driven approaches: an artificial neural network method was used for wave prediction under complex configurations, and a panel data model was used to predict the time series data of wave characteristics.

3.1 Theoretical model

This section provides a two-dimensional theoretical model to express the physical mechanism governing the slide-water interaction. Zitti et al. (2016) studied how mass and momentum were exchanged between the incoming sliding mass and the outgoing impulse wave using a control volume surrounding the impact zone. They developed mass and momentum balance equations for both the slide phase and water phase in the control volume. The left boundary of the selected control volume was overlapped with the shoreline. The unknown parameters at the left boundary of the control volume involve the thickness and depth-averaged velocity of the slide mass. Zitti et al. (2016) assumed the slide velocity as a constant and the slide thickness following a parabolic curve. The theoretical model proposed in this section followed Zitti et al. (2016), with the slide parameters at the left boundary given by the lubrication model and kinematic wave model (Ancey et al., 2012).

3.1.1 Governing equations

Following Zitti et al. (2016), we now consider the mass and momentum balance equations in a control volume V (see Figure 3.1). The control volume V consists of three phases: the slide phase, the water phase, and the air phase. Neglecting the influence of the air phase, I developed governing equations for the slide phase and the water phase.

The integral form of mass and momentum balance equations at time t for each phase can be

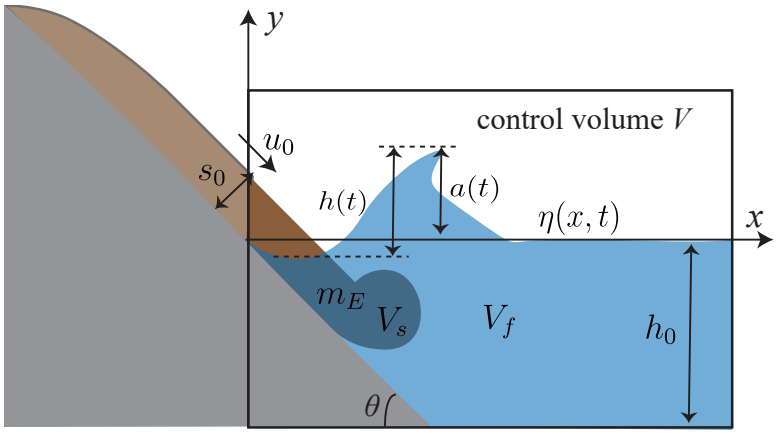

Figure 3.1 – Sketch of the control volume.

written as:

$$\frac{d}{dt}\int_V \alpha_i \rho_i dV = \frac{d}{dt}\int_V \alpha_i \rho_i dV + \int_S \alpha_i \rho_i (\mathbf{u}_i \cdot \mathbf{n})\, dS = 0 \tag{3.1}$$

$$\frac{d}{dt}\int_V \alpha_i \rho_i \mathbf{u}_i dV = \frac{d}{dt}\int_V \alpha_i \rho_i \mathbf{u}_i dV + \int_S \alpha_i \rho_i \mathbf{u}_i (\mathbf{u}_i \cdot \mathbf{n})\, dS = \mathbf{F} \tag{3.2}$$

where the subscript $i = s, f$ refers to the slide or fluid phase, α_i is the fraction of the volume occupied by phase i, ρ_i denotes the density of each phase, and $\mathbf{u}_i$ denotes the velocity. $\mathbf{F}$ are the forces applied on the control volume V.

Equations (3.1) and (3.2) can be written in a manner that is easier to interpret. The volume-averaged slide and fluid velocities are denoted by:

$$\bar{\mathbf{u}}_i = \frac{1}{V_i}\int_V \mathbf{u}_i dV \tag{3.3}$$

where the subscript $i = s, f$. The depth-averaged velocities at the left and right boundaries of the control volumes are defined similarly, for example, the depth-averaged velocity of the water phase at the right boundary can be written as:

$$\bar{\mathbf{u}}_{f,r} = S_r^{-1}\int_{S_r} \mathbf{u}_{f,r} dS \tag{3.4}$$

where $S_r = B(h_0 + \eta_r)$ is the surface of the outgoing flow with B denoting the width of the flume. Thus, the mass balance Equation (3.1) for the slide phase becomes:

$$\rho_s \frac{dV_s}{dt} - \rho_s B s_0(t) u_0(t) = 0 \tag{3.5}$$

and for the water phase becomes:

$$\rho_f \frac{dV_f}{dt} + \rho_f \bar{u}_{f,r}(t)(h_0 + \eta_r)B = 0 \tag{3.6}$$

where ρ_s and ρ_f denote the slide density and water density, respectively; V_s and V_f represent the volume of slide phase and water phase in V, respectively; $s_0(t)$ and $u_0(t)$ denote the thickness and depth-averaged velocity of the sliding mass passing through the left boundary of the control volume V, respectively; B denotes the flume width, t is the time, l_s is the slope length, h_0 is the still water depth, η_r is the water surface perturbation at the right boundary, and $\bar{u}_{f,r}$ denotes the depth-averaged water velocity at the right boundary.

On the left-hand side of Equations (3.5) and (3.6), the first terms represent the rate of change of the mass of slide and fluid in the control volume V, respectively. The second term of Equation (3.5) reflects the slide material's mass flux across the left boundary of V, and the second term of Equation (3.6) the fluid mass across the right boundary of V.

The momentum balance Equation (3.2) for the slide phase in the x-direction is then expressed as:

$$\rho_s \frac{dV_s \bar{u}_s}{dt} - \rho_s B s u_0^2 \cos\theta = -F_{D,x} + F_{P,x} \tag{3.7}$$

and in the y-direction:

$$\rho_s \frac{dV_s \bar{v}_s}{dt} - \rho_s B s u_0^2 \sin^2\theta / \cos\theta = -F_{D,y} + F_{P,y} - \rho_s V_s g \tag{3.8}$$

For the water phase, we can write the momentum balance in the x-direction as:

$$\rho_f \frac{dV_f \bar{u}_f}{dt} + \rho_f \bar{u}_{f,r}^2 (h+\eta_r) B = F_{D,x} - \frac{1}{2}\rho_f g B \left[(h+\eta_r)^2 - (h+\eta_l)^2\right] \tag{3.9}$$

and in the y-direction as:

$$\rho_f \frac{dV_f \bar{v}_f}{dt} = F_{D,y} \tag{3.10}$$

where η_l and η_r are the water surface perturbation at the left and right boundary, respectively; $(\bar{u}_s, \bar{v}_s)$ are the slide's mean velocity in V in the x- and y-direction, respectively; $(\bar{u}_f, \bar{v}_f)$ are the water's mean velocity in V in the x- and y-direction, respectively; and $(F_{D,x}, F_{D,y})$ is the drag force and $(F_{P,x}, F_{P,y})$ is the hydrostatic force applied on the slide material. Equations (3.5) to (3.10) form a system of 6 coupled equations describing the interplay between the slide phase and the fluid phase. The dependence variables include $\bar{u}_s$, $\bar{v}_s$, $\bar{u}_f$, $\bar{v}_f$, V_s and V_f.

On the left-hand side of Equation (3.7) to (3.10), the first terms represent the rate of change in the side's (or fluid's) momentum in the x- (or y-) direction inside V, the second terms reflect the solid's (or fluid's) momentum flux across the boundary of the control volume V. The right-hand sides of Equation (3.7) to (3.10) reveal that two mechanisms are at play in the momentum change and transfer to the fluid phase: the momentum imparted by the slide phase through the drag force and the pressure force difference. For the momentum balance equation of the slide phase in y-direction (Equation (3.8)), the hydrostatic force is assumed to be balanced with the gravity force, as the density of the slide material used in experiments is close to that of water. For the momentum balance of the water phase in x-direction (Equation (3.9)), the hydrostatic force applied to water by the submerged slide is considered balanced

with the hydrostatic force at the right boundary.

The hydrostatic force $\mathbf{F}_\mathrm{P}$ can be written in an integral form:

$$\mathbf{F}_\mathrm{P} = \int_{A_s} -\rho_f g h_{sf} \mathbf{n} dA_s \tag{3.11}$$

where A_s denotes the area of the slide-water interface, h_{sf} is the vertical distance between the slide-water interface and the free-water surface, and $\mathbf{n}$ denotes the normal vector. We approximate the drag force $\mathbf{F}_D$ by:

$$\mathbf{F}_D = \frac{1}{2} C_d \rho_f A_f \left(\bar{\mathbf{u}}_s - \bar{\mathbf{u}}_f\right) | \bar{\mathbf{u}}_s - \bar{\mathbf{u}}_f | \tag{3.12}$$

where A_f is the effective cross-sectional area of the slide-water interface, C_d is the drag coefficient (we take $C_d = 0.5$); and $\bar{\mathbf{u}}_s$ and $\bar{\mathbf{u}}_f$ are idealized by the mean velocity of the slide phase and water phase in the control volume, respectively. Here, A_f, $\bar{\mathbf{u}}_s$ and $\bar{\mathbf{u}}_f$ are unknown.

3.1.2 Boundary conditions

For the right boundary, I assumed that the depth-averaged outgoing velocity in the $y-$direction $\bar{v}_{f,r} = 0$ and considered that the water pressure difference has a neglectable effect on the wave generation; that is, $\eta_r - \eta_l = 0$. The $\bar{u}_{f,r}$ is unknown. Analogous to solitary waves generated by a piston wave maker, the depth-averaged velocity can be related to the free surface perturbation, that is, $\bar{u}_f = C\frac{\eta}{h_0+\eta}$, with the phase speed $C = \sqrt{g\left(h_0 + a\right)}$ and the wave amplitude a. Assuming the phase speed at the right boundary is $C = \sqrt{g\left(h_0 + \eta_r\right)}$ and the outgoing velocity is close to the volume-averaged velocity ($\bar{u}_{f,r} = \bar{u}_f$), the closure equation can be written as:

$$\bar{u}_f = \eta\sqrt{\frac{g}{h_0 + \eta}} \tag{3.13}$$

and thus the free-water surface perturbation:

$$\eta_r = \frac{1}{2g}\left(\bar{u}_f^2 + u_f\sqrt{\bar{u}_f^2 + 4gh_0}\right) \tag{3.14}$$

For the left boundary, the slide thickness $s_0(t)$ and the depth-averaged velocity $u_0(t)$ crossing the boundary must be given. As shown in Figure 3.2, I used a coordinate system $(\hat{x}, \hat{y})$, where $\hat{x}$ denotes the downstream coordinate measured from the top of the plane and $\hat{y}$ denotes the coordinate normal to the slope. The initial flow depth is given by:

$$s(\hat{x}) = s_g + (\hat{x} - l_0)\tan\theta \tag{3.15}$$

and the initial flow depth at the lock gate s_g is given by:

$$s_g = V_I / l_0 + \frac{1}{2} l_0 \tan\theta \tag{3.16}$$

where V_I is the volume of the slide material in the reservoir and l_0 denotes the length of the slide material in the reservoir.

The interest is to determine $s(\hat{x} = l_s, \hat{t})$ and $u(\hat{x} = l_s, \hat{t})$, where l_s is the distance from the origin to the left boundary of the control volume V, and $\hat{t}$ is time. The time difference between Figure 3.1 and 3.2 is $t = \hat{t} - t_0$, with t_0 as the time taken from the slide starts moving till the front touches the left boundary of V.

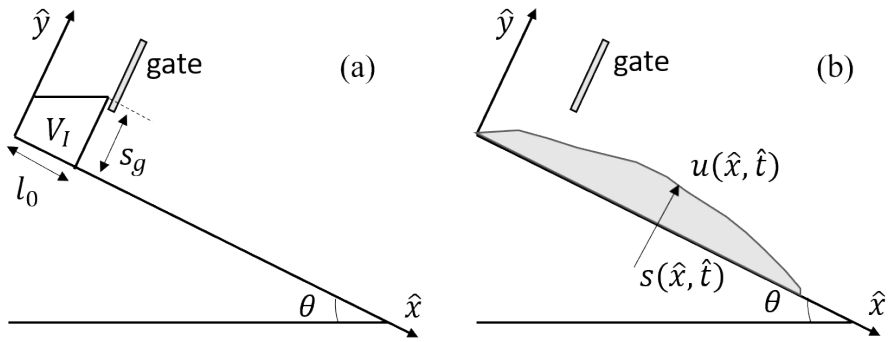

Figure 3.2 – Sketch of the sliding mass (a) at rest and (b) moving along the slope.

I first considered a steady uniform flow of viscoplastic fluid over an inclined surface. The rheological behavior of the viscoplastic fluid is described by the Herschel-Bulkley equation (see Equation (2.1)). Independently of the constitutive equation, the shear stress distribution throughout the depth is:

$$\tau(\hat{y}) = \rho_s g (s - \hat{y}) \sin\theta \tag{3.17}$$

where s denotes the flow depth, ρ_s is the density of the slide material, and g is the gravitational acceleration. The no-slip condition was assumed for the stream-wise velocity component u at the bottom (i.e., $u(\hat{y} = 0) = 0$). The integration of the constitutive Equation (2.1) provides the cross-stream velocity profile:

$$u(\hat{y}) = \frac{nA}{n+1} \begin{cases} \left(Y_0^{1+1/n} - (Y_0 - \hat{y})^{1-1/n}\right) & \hat{y} \le Y_0 \\ Y_0^{1+1/n} & \hat{y} \ge Y_0 \end{cases} \tag{3.18}$$

with

$$Y_0 = s - s_c, \quad A = \left(\frac{\rho_s g \sin\theta}{\mu}\right)^{1/n}, \quad s_c = \tau_c / \left(\rho_s g \sin\theta\right) \tag{3.19}$$

where s_c denotes the critical flow depth, that is, no steady uniform flow is possible for $s < s_c$ and Y_0 denotes the position of the yield surface with $\hat{y} < Y_0$ the sheared region and $\hat{y} > Y_0$ the

unyielding region. A further integration leads to the depth-averaged velocity:

$$\bar{u} = \frac{nA}{(n+1)(2n+1)} \frac{s(n+1)+ns_c}{s} Y_0^{1+1/n} \tag{3.20}$$

When the flow is slightly non-uniform, the shear stress alters as a result of the changes in the free-surface gradient. A common approach is to start from the Cauchy momentum balance equation, in which the inertia terms have been neglected together with the normal stress gradient (Balmforth and Provenzale, 2001). With the assumption of negligible inertia, the downstream projection of the momentum balance equation reads: $0 = \rho_s g \sin\theta - \frac{\partial p}{\partial \hat{x}} + \frac{\partial \tau}{\hat{y}}$, and the pressure is found to be hydrostatic to leading order: $p = \rho_s g(s-\hat{y})\cos\theta$. Then, the shear stress distribution reads:

$$\tau = \rho_s g(s-\hat{y})\cos\theta \left(\tan\theta - \frac{\partial s}{\partial \hat{x}}\right) \tag{3.21}$$

Substituting Equation (3.21) into Equation (2.1) and integrating it yields:

$$u(\hat{y}) = \frac{nK}{n+1}\left(\tan\theta - \frac{s}{\hat{x}}\right)^{1/n} \begin{cases} \left(Y_0^{1+1/n} - \left(Y_0-\hat{y}\right)^{1+1/n}\right) & \hat{y} \le Y_0 \\ Y_0^{1+1/n} & \hat{y} \ge Y_0 \end{cases} \tag{3.22}$$

with the parameter K and the updated yield surface position Y_0:

$$K = \rho g \sin\theta / k, \quad Y_0 = \max(0, s - \tau_c/(\rho g \cos\theta(\tan\theta - \partial_x s))) \tag{3.23}$$

The critical depth is $s_c = \tau_c / \left(\rho_s g \sin\theta\right)$. A further integration leads to the depth-averaged velocity for non-uniform flow:

$$\bar{u} = \frac{nK}{(n+1)(2n+1)}\left(\tan\theta - \frac{\partial s}{\partial \hat{x}}\right)^{1/n} \frac{s(n+1)+ns_c}{s} Y_0^{1+1/n} \tag{3.24}$$

Using Equation (3.24) requires an equation specifying the gradient of the free surface $\partial_x s(\hat{x},\hat{t})$. I used the kinematic wave model to evaluate $s(\hat{x},\hat{t})$. The kinematic wave approximation assumes that the fluid is locally uniform; that is, $\bar{u}$ is given by Equation (3.20). The bulk mass balance $\frac{\partial s}{\partial \hat{t}} + \frac{\partial s\bar{u}}{\hat{x}} = 0$ provides the governing equation for s:

$$\frac{\partial s}{\partial \hat{t}} + f'(s)\frac{\partial s}{\partial \hat{x}} = 0 \tag{3.25}$$

$$\text{with} \quad f'(s) = As(s-s_c)^{1/n}, \quad \text{and} \quad A = \left(\frac{\rho g \sin\theta}{\mu}\right)^{1/n} \tag{3.26}$$

This hyperbolic nonlinear advection equation can be solved easily using the method of characteristics. Equation (3.25) can be put into a characteristic form $\frac{ds}{d\hat{t}} = 0$ along the characteristic curve $\frac{d\hat{x}}{d\hat{t}} = f'(s)$. These initial characteristic curves are straight lines whose

slope is dictated by the initial depth:

$$\hat{x} = f'(s(\hat{x}_0))\hat{t} + \hat{x}_0 \tag{3.27}$$

with $s_0(\hat{x}_0)$ the initial value of s at $\hat{x}_0$ is given be Equation (3.15) and (3.16). As $h = h_0$ along the characteristic curve, using Equation (3.15) to eliminate $\hat{x}_0$, an implicit equation for s can be obtained:

$$\hat{x} = As(s - s_c)^{1/n}\hat{t} + (s - s_g)\cot\theta + l_0 \tag{3.28}$$

The starting time counted for Equation (3.28) is given by $x_f(t) = l_s$ (details see Ancey et al. (2012)). Then, with Equations (3.24) and (3.28), $u_0(t)$ and $s_0(t)$ at the left boundary of the momentum balance equations (Equations (3.5) to (3.10)) are given.

3.1.3 Dimensional analysis

Following common practice in this field, some dimensionless groups have been introduced directly: the slide material thickness s_0 was scaled as $S = s_0/h_0$, where h_0 is the original still-water depth. The initial slide mass m_I was scaled as $M = m_I/\rho_f B h_0^2$, where ρ_f is the water density and B is the flume width. The slide velocity upon impact u_0 was scaled by the water wave velocity $\sqrt{gh_0}$, resulting in the classic Froude number $\mathrm{Fr} = u_0/\sqrt{gh_0}$.

In this study, the dimensionless groups were derived by scaling the mass and momentum balance equations. Using the following change in the variables in Equation (3.7):

$$\begin{aligned} &V_f \to Bh_0^2 V_f', \quad V_s \to V_E V_s', \quad t \to \sqrt{h_0/g}\,t' \\ &(u_s, u_f) \to u_0(u_s', u_f'), \quad s \to s_0 s', \end{aligned} \tag{3.29}$$

where B is the flume width, V_E is the slide's volume when the wave height reaches its maximum, and s_0 is the mean slide thickness when it penetrates the water. The momentum balance equation of the slide phase (Equation (3.7)) was considered as the most important equation governing the momentum transfer from the slide phase to the water phase. The scaled momentum balance equation of the slide phase in the x-direction is:

$$\rho_s\sqrt{\frac{g}{h_0}}u_0 V_E \frac{\mathrm{d}u_s' V_s'}{\mathrm{d}t} - \rho_s s_0 u_0^2 B\cos\theta = -F_x. \tag{3.30}$$

We then cast it in the following form:

$$\frac{V_E}{Bh_0^2}\frac{\mathrm{d}u_s' V_s'}{\mathrm{d}t} - \frac{s_0}{h_0}\frac{u_0}{\sqrt{gh_0}}\cos\theta = -\frac{F}{h_0 B u_0\sqrt{gh_0}\rho_s}. \tag{3.31}$$

Three dimensionless groups appear in Equation (3.31):

$$\Pi_1 = \frac{V_E\rho_s}{Bh_0^2\rho_s} = \frac{m_E}{\rho_s B h_0^2} \tag{3.32}$$

where m_E is the effective slide mass (related to V_E). The dimensionless group Π_1 corresponds to the scaled effective mass M. The second group is:

$$\Pi_2 = s_0 / h_0 \tag{3.33}$$

which corresponds to the scaled slide thickness S. The third dimensionless group is the slide Froude number:

$$\Pi_3 = \mathrm{Fr} = u_0 / \sqrt{g h_0} \tag{3.34}$$

The dimensionless groups obtained from the dimensional analysis of governing equations were the same as those commonly used in previous studies. In this study, the slide Froude number Fr, scaled effective mass Π_1, and scaled thickness Π_2 varied within: $0.05 < \mathrm{Fr} < 2.78$, $0.03 < \Pi_1 < 0.33$, and $0.12 < \Pi_2 < 0.25$.

3.2 Data driven analysis

3.2.1 Artificial neural network

The artificial neural network (ANN) has been successfully employed in many other fields to cope with complex dependence in experimental data processing and to develop highly accurate predictive models (Abraham, 2005; Kim and Park, 2005; Yegnanarayana, 2009; Lee et al., 2016; Armaghani et al., 2016; Gedik, 2018). In contrast to empirical equations in which mathematical dependence is fixed in advance, the internal relation between the explanatory and explained variables in the ANN model is defined without any prior assumptions about the equation's functional form or physical constraints. Thus, the model can be easily calibrated when new parameters are available, making it powerful for solving complex problems (Dou et al., 2015).

As shown in Figure 3.3, the ANN method is inspired by how the human brain processes information and is constructed from interconnected processing elements called neurons (Liu et al., 2000). A typical ANN model consists of three parts: learning rules, network structure, and activation function. The network structure comprises several layers: one input layer, one output layer, and one or several hidden layers with each layer containing several neurons. Each of the neurons in a layer is connected to neurons of the adjacent layers via coefficients called weightings.

From a mathematical perspective, the principle of neural networks involves the composition of non-linear functions. Starting with a linear model, considering a dataset z and a vector of inputs x, a linear model for the output $\hat{z}(x)$ can be constructed considering $\hat{z}(x) = Wx + \beta$, where the weighting matrix W and the bias vector β are obtained by solving an optimization problem that minimizes the overall difference between z and $\hat{z}$. This process is called model training. Such a simple model may lack the flexibility to represent complex functional mapping, so intermediate variables (layers) y are introduced: $y = \sigma(W^{(1)}x + \beta^{(1)})$ and

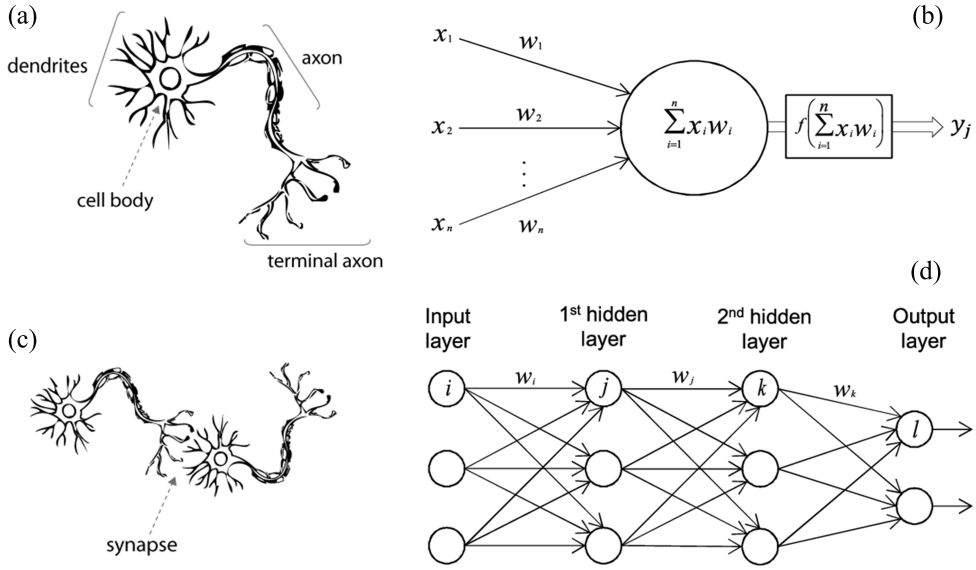

Figure 3.3 – A biological neuron in comparison to an artificial neural network: (a) human neuron; (b) artificial neuron; (c) biological synapse; and (d) ANN synapses (Suzuki, 2013).

$z = W^{(2)} y + \beta^{(2)}$, where σ is a user-specified activation function, like the hyperbolic tangent. The composition of several intermediate layers results in a neural network capable of efficiently representing arbitrarily complex function forms.

In this thesis, I selected a one-hidden-layer network, and adopted a feed-forward back-propagation algorithm to train the network. The algorithm programming was developed using Matlab. Establishing an ANN model consists of three steps: (i) preparing the required data for training the network; (ii) evaluating neural networks with different structures and choosing the optimal one; and (iii) testing the neural network's performance using data that have not been used previously for training the network.

The feed-forward path is expressed by Equations (3.35) and (3.36):

$$y_i = f\left(X_j\right) = f\left(W_{oj} + \sum_{i=1}^{I} W_{ij} x_i\right) \tag{3.35}$$

$$Z_k = f\left(Y_k\right) = f\left(W_{ok} + \sum_{j=1}^{J} W_{jk} y_i\right) \tag{3.36}$$

where x_i, y_j, and Z_k represent the input, hidden, and output layers, respectively, W_{oj} and W_{ok} are the bias weightings for setting the threshold values, X_j and Y_k temporarily represent computing results before using the activation function, and f is the activation function applied in the hidden and output layers.

For the activation function, I chose the Sigmoid function, which ranges between 0 and 1 (see

Equation (3.37)). The activation function is defined on each layer's neurons and is applied to the sum of the weighted inputs and to each neuron's bias to generate the neuron output.

$$f(a) = \frac{e^a}{e^a + 1} \quad (a = X_j, Y_k) \tag{3.37}$$

Equation (3.38) displays the residual function for residual back-propagation training.

$$E = \frac{1}{2}\sum_{k=1}^{K} e_k^2 = \frac{1}{2}\sum_{k=1}^{K} (t_k - z_k)^2 \tag{3.38}$$

where t_k is the predefined target value and e_k is the residual of each output node. E is the residual between the expected and actual output values.

I used a gradient-descent strategy to adjust the weightings, aiming to obtain a minimum E. Equations (3.39) to (3.42) express the weightings between the hidden and output layers:

$$\frac{\partial E}{\partial w_{jk}} = -e_k \frac{\partial F(Y_k)}{Y_k} y_j = -\delta_k y_j \tag{3.39}$$

and hence

$$\delta_k = e_k F'(Y_k) = (t_k - z_k) F'(Y_k) \tag{3.40}$$

Therefore, the weighting adjustments in the hidden and output link Δw_{jk} can be expressed by:

$$\Delta w_{jk} = \eta \times y_j \times \delta_k \tag{3.41}$$

where η is the learning rate ranging between 0 and 1. With a lower learning rate, the network model will take a longer time to converge. Conversely, a higher learning rate may lead to a widely oscillating network. In addition, maintaining a consistent learning rate across the model is preferable. The new weighting w_{jk} is updated by Equation (3.42), where r is the number of iterations.

$$w_{jk}(r+1) = w_{jk}(r) + \Delta w_{jk}(r) \tag{3.42}$$

Similarly, the error gradient in the links between the input and hidden layers can be derived from the partial derivative with respect to w_{ij}.

$$\frac{\partial E}{\partial w_{ij}} = \left(\sum_{k=1}^{K} \frac{\partial E}{\partial z_k} \frac{\partial z_k}{\partial Y_k} \frac{Y_k}{y_j}\right) \times \frac{\partial y_i}{\partial X_j} \times \frac{\partial X_j}{\partial w_{ij}} = -\Delta j x_i \tag{3.43}$$

where

$$\Delta j = F'(X_j) \sum_{k=1}^{K} \delta_k w_{jk} \tag{3.44}$$

The new weighting dominates the link between the input layer and the hidden layer, δw_{ij}, and can be updated as:

$$\delta w_{ij} = \eta \times x_i \times \delta_j \tag{3.45}$$

$$w_{ij}(r+1) = w_{ij}(r) + \delta w_{ij}(r) \tag{3.46}$$

All of the input data were normalized in the range between 0 and 1 using the following equation:

$$Y = \frac{X - X_{min}}{X_{max} - X_{min}} \tag{3.47}$$

where X is the raw data and Y is the normalized data. The initial parameter settings are shown in Table 3.1.

Table 3.1 – Initial settings for the parameters in the ANN model.

Parameters	Initial setting
Initial weightings	0.2-0.5
Learning rate	0.1
Maximum number of epochs	200
Objective mean square error	0.00001
Training function	traingdx
Momentum parameters	0.9
Activation function	Sigmoid function

The performance of predictive models can be evaluated by the coefficient of determination (R^2), mean square error (MSE), and its sum of squares due to error (SSE):

$$R^2 = 1 - \sum_{i=1}^{\epsilon} \left(\frac{\left(y_{p,i} - y_{o,i}\right)^2}{\left(y_{p,i} - \bar{y}_o\right)^2} \right) \tag{3.48}$$

$$\text{MSE} = \sqrt{\frac{\sum_{i=1}^{\epsilon} \left(y_{p,i} - y_{o,i}\right)^2}{\epsilon}} \tag{3.49}$$

$$\text{SSE} = \sum_{i=1}^{\epsilon} (y_{o,i} - y_{p,i}) \tag{3.50}$$

where ϵ is the number of series of experimental data, $y_{p,i}$ and $y_{o,i}$ are the predicted and observed data, respectively, and $\bar{y}_o$ is the average of observed data.

3.2.2 Panel data analysis

A panel data model was used to solve the problem of predicting the temporal wave characteristics from the time series data of slide parameters. As shown in Figure 3.4, the experimental dataset can be considered as a data panel with three dimensions that contains a time series t and a cross-sectional panel $x - y$. The cross-sectional panel includes a counter for experiments y and the parameters recorded in each experiment x (e.g., slide velocity, slide thickness, wave amplitude). For example, a data $N(x_a, y_b, t_c)$ represents the experimental

data of the ath parameter of the bth test at time c. The idea was to quantify the relation between the time series data of wave characteristics and time series data of slide parameters.

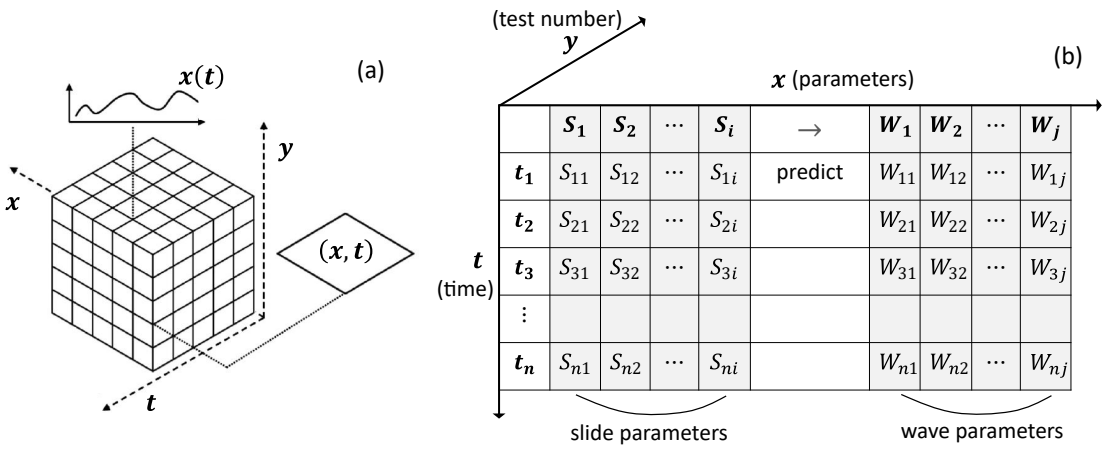

Figure 3.4 – The (a) three-dimensional and (b) two-dimensional structures of data panel.

Random coefficient panel data

For the panel data model, I selected the random coefficient model and started from a two dimensional dataset. Equation (3.51) expresses the regression coefficients of a two-dimensional panel, a $x-y$ panel without time variation.

$$y_{it} = \sum_{i=1}^{K} \beta_{ki} x_{kit} + u_{it} = \sum_{k=1}^{K} (\beta_k + \gamma_{ki}) x_{kit} + u, \tag{3.51}$$

where y_{it} is the cross-sectional data, x_{kit} denotes the explanatory variables, t is the time index; i is the index of the tests, k is the explanatory variables index, β_{ki} includes β_k and γ_{ki}, $\beta = (\beta_1, \cdots, \beta_K)'$ is the common mean coefficient vector, $\gamma = (\gamma_{1i}, \cdots, \gamma_{Ki})'$ is the operator from individual data to the common mean value, and u is a random interference term. Assuming $\beta_i = \beta + \gamma_i$ as a random variable (Swamy, 1970):

$$\begin{aligned}
&E(\gamma_i) = 0, \\
&E(\gamma_i \gamma_j') = \begin{cases} \Delta, & i = j, \\ 0, & i \neq j, \end{cases} \\
&E(x_{it} \gamma_j') = 0, \\
&E(u_i u_j') = \begin{cases} \sigma_i^2 I_T & i = j, \\ 0, & i \neq j. \end{cases}
\end{aligned} \tag{3.52}$$

Integrating the NTth observation data, Equation (3.53), which is in the form of the matrix can

be obtained.

$$y = X\beta + \widetilde{X}\gamma + u, \tag{3.53}$$

where $y_{NT\times 1} = (y_1^{'}, \cdots, y_N^{'})^{'}$, $X_{NT\times K} = \begin{bmatrix} X_1 \\ X_2 \\ \vdots \\ X_N \end{bmatrix}$, $\widetilde{X}_{NT\times NK} = \begin{pmatrix} X_1 & & & 0 \\ & X_2 & & \\ & & \ddots & \\ 0 & & & X_N \end{pmatrix}$, $u = (u_1', \cdots, u_N')'$, $\gamma = (\gamma_1', \cdots, \gamma_N')'$, N counts the number of the cross-sectional panel, T is the test number in each panel, the compound error term $\widetilde{X}\gamma + u$ is a diagonal matrix, and the ith diagonal block is $\psi_i = X_i \Delta X_i' + \sigma_i^2 I_T$. According to Swamy (1970), the estimation of β with ordinary least squares is biased. Once $\frac{1}{NT} X'X$ converges into a non-zero constant matrix, we can obtain a consistent non-effective estimation. The optimal linear unbiased estimator of β is eliminated from the generalized least squares:

$$\begin{aligned} \hat{\beta}_{GLS} &= \left(\sum_{i=1}^{N} X_i^{'} \psi_i^{-1} X_i \right)^{-1} \left(\sum_{i=1}^{N} X_i^{'} \psi_i^{-1} y_i \right) = \sum_{i=1}^{N} W_i \hat{\beta}_i, \\ W_i &= \left\{ \sum_{i=1}^{N} \left[\Delta + \sigma_i^2 (X_i^{'} X_i)^{-1} \right]^{-1} \right\}^{-1} \left[\Delta + \sigma_i^2 (X_i^{'} X_i)^{-1} \right]^{-1}, \\ \hat{\beta}_i &= \left(X_i^{'} X_i \right)^{-1} X_i^{'} y_i. \end{aligned} \tag{3.54}$$

The variance of the estimator is:

$$Var\left(\hat{\beta}_{GLS}\right) = \left(\sum_{i=1}^{N} X_i^{'} \psi_i^{-1} X_i \right)^{-1} = \left\{ \sum_{i=1}^{N} \left[\Delta + \sigma_i^2 (X_i^{'} X_i)^{-1} \right]^{-1} \right\}^{-1}. \tag{3.55}$$

$\hat{\beta}_{GLS}$ follows an asymptotic normal distribution and is an effective estimation of β. The random coefficient model limits the explanatory variables coefficients by constraining the coefficients of the explanatory variables following asymptotic normal distributions.

Classification of the dataset

As observed from experiments, large waves and small waves often have different tends in time variation of wave features. This difference may induce uncertainties in predicting wave characteristics of time series. To avoid these uncertainties, we used a Gaussian mixture model to classify the dataset into several groups based on the properties of the data samples. Here, I selected the slide Froude number Fr, scaled thickness S and scaled effective mass M as the evaluation criteria to classify the dataset into several groups. I then used the random coefficient panel data model to model each sub-dataset separately.

For multivariate continuous data, the parametrized component density mostly is a multivariate Gaussian density. For a one-dimensional dataset, the probability distribution of a

random variable x follows a mixture of two Gaussian distributions:

$$P\left(x|\mu_1,\mu_2,\sigma\right)=\sum_{k=1}^{2}p_k\frac{1}{\sqrt{2\pi\sigma^2}}\exp\left(-\frac{\left(x-\mu_k\right)^2}{2\sigma^2}\right), \tag{3.56}$$

where $k=1$ and $k=2$ represent two Gaussian distributions, the kth prior probability is $\left\{p_1=1/2,p_2=1/2\right\}$, and $\left\{\mu_k\right\}$ and σ are the mean value and variance of the two Gaussian distributions, respectively. We use $\theta\equiv\left\{\left\{\mu_k\right\},\sigma\right\}$ to simplify these parameters. The dataset $\{x_n\}_{n=1}^N$ containing N tests is assumed as an independent sample from the distribution. k_n denotes the unknown class tag for the nth test. In the case when $\left\{\mu_k\right\}$ and σ are known, the posterior probability of the class tag of the nth test k_n can be written as:

$$P\left(k_n|x_n,\theta\right)=\frac{1}{1+\exp\left[-\left(\omega_1x_n+\omega_0\right)\right]}. \tag{3.57}$$

If the case when $\left\{\mu_k\right\}$ is unknown but σ is known, we can deduce $\left\{\mu_k\right\}$ from the data series $\{x_n\}_{n=1}^N$. We then derive the iterative algorithm of $\left\{\mu_k\right\}$ to maximize the likelihood estimation:

$$P\left(\{x_n\}_{n=1}^N|\left\{\mu_k\right\},\sigma\right)=\prod_n P\left(x_n|\left\{\mu_k\right\},\sigma\right). \tag{3.58}$$

The natural logarithm of the likelihood L can then be expressed as:

$$\frac{\partial}{\partial\mu_k}L=\sum_n p_{k|n}\frac{x_n-\mu_k}{\sigma^2}, \tag{3.59}$$

where $p_{k|n}\equiv P\left(k_n=k|x_n,\theta\right)$ is the Gaussian density (see Equation (3.57)). Ignoring the items in $\frac{\partial}{\partial\mu_k}P\left(k_n=k|x_n,\theta\right)$, the second derivative versus $\left\{\mu_k\right\}$ can be approximated as:

$$\frac{\partial^2}{\partial\mu_k^2}L=-\sum_n p_{k|n}\frac{1}{\sigma^2}. \tag{3.60}$$

μ_1' and μ_2' can be obtained by iterating the initial μ_1 and μ_2 using the approximate Newton–Raphson steps.

$$\mu_k'=\frac{\sum_n p_{k|n}x_n}{\sum_n p_{k|n}}. \tag{3.61}$$

The Gaussian mixture density of a multidimensional dataset (i.e., multiple Gaussian distribution) can be written as:

$$p_{k|n}=\frac{\pi_k\frac{1}{\prod_{i=1}^I\sqrt{2\pi}\sigma_i^{(k)}}\exp\left(-\sum_i^I\left(\mu_i^{(k)}-x_i^{(n)}\right)^2/2\left(\sigma_i^{(k)}\right)^2\right)}{\sum_{k'}\pi_{k'}\frac{1}{\prod_{i=1}^I\sqrt{2\pi}\sigma_i^{(k')}}\exp\left(-\sum_i^I\left(\mu_i^{(k')}-x_i^{(n)}\right)^2/2\left(\sigma_i^{(k')}\right)^2\right)}, \tag{3.62}$$

with k the serial number of the Gaussian distribution, i the serial number of the data's dimension, n the serial number of the data sequence, I the total number of the data's

dimension, π_k the weighting, $\mu_i^{(k)}$ the mean value of the Gaussian distribution, $\sigma_i^{(k)}$ the variance of the Gaussian distribution, and $x_i^{(n)}$ a parameter in an experiment. The iterative formula of μ_i^k has been presented in Equation (3.61). The iterative formulas of the variance $\sigma_i^{(k)}$ and the weighting π_k are as follows:

$$\sigma_i^{2(k)} = \frac{\sum_n p_{k|n} \left(x^{(n)} - \mu_i^{(k)} \right)^2}{\sum_n p_{k|n}}, \tag{3.63}$$

$$\pi_k = \frac{\sum_n p_{k|n}}{\sum_k \sum_n p_{k|n}}. \tag{3.64}$$

4 Role of slide material's properties in wave prediction

This chapter presents the role of the slide material's properties in wave prediction. The results were obtained from the experiments conducted with high-speed cameras. Section 4.1 examines how the viscoplastic slide's parameters on impact depend on the initial settings of experiments. Section 4.2 investigates the effect of slide cohesion on wave generation by comparing waves generated by Carbopol and water balls. Section 4.3 applies a purely data-driven approach to predict wave characteristics under complex configurations, such as integrating the parameters of different categories of slide material into one model (the Bingham number for viscoplastic material and the grain diameter for granular material).

4.1 Slide parameters on impact

As analyzed in section 3.1.3, the momentum transfer from the slide to water greatly depend on three slide parameters: the slide velocity on impact u_0, the slide thickness on impact s_0, and the effective slide mass m_E. In this section, with the support of the experiments conducted using Carbopol, I examine how these parameters depend on the initial parameters for impulses waves generated by viscoplastic fluids.

4.1.1 Slide velocity and thickness

The slide thickness on impact s_0 and velocity on impact u_0 were estimated by Carbopol's frontal velocity and thickness when the front of slide reaches the shoreline. Figure 4.1 (a) and (b) shows the variations of s_0 and u_0 to the initial settings of experiments, respectively. The initial parameters were varied symmetrically: the slope length l_s = 0.85, 0.95, and 1.05 m, the initial slide mass m_I varied from 2 to 5.8 kg, the slope angle $\alpha = 6/\pi$ and $4/\pi$, and the yield stress of Carbopol τ_c = 60, 75, and 90 Pa. The yield stress τ_c represents the rheological properties of Carbopol (see Table 2.1). Within the set of range used in the experiments, s_0 varied between 0.025 and 0.05 m and u_0 varied from 1.1 to 2.4 m/s. In general, s_0 increases with the increase of m_I, α and τ_c and with the decrease of l_s. u_0 increases with the increase of

m_I, α and with the decrease of τ_c and l_s.

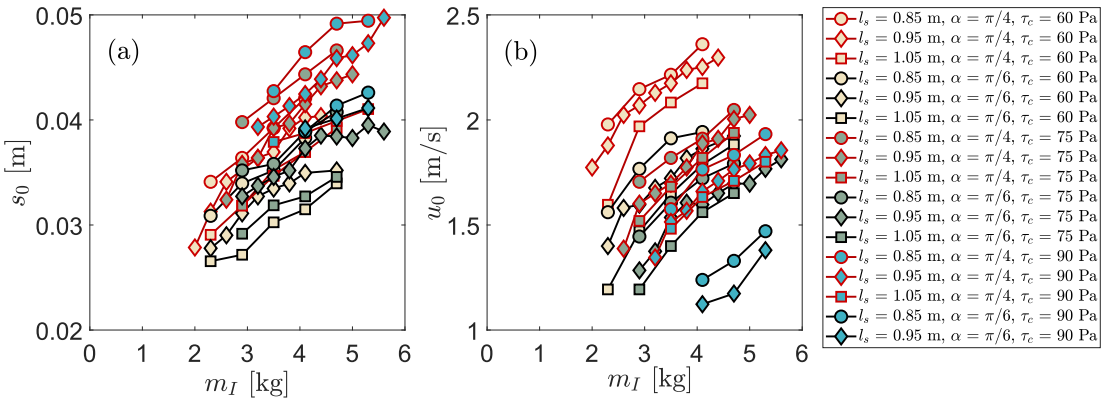

Figure 4.1 – Variation of (a) s_0 and (b) u_0 with the initial settings of the experiments.

4.1.2 Effective mass

In most previous experiments with blocks or granular slide materials, the sliding mass intruded into the body of water at very high velocities in a very short time. Thus, the mass of the slide material at impact was often approximated with its initial mass. Carbopol gels flowed downstream more slowly than most granular materials used in previous studies and spread themselves more uniformly along the chute. Part of the gel volume could deposit along the chute. Whereas the granular particles penetrated quickly into the body of water, the Carbopol gels entered and interacted more smoothly with the water phase. Thus, only a fraction of the sliding mass engages in the leading wave generation.

When analyzing the momentum conservation equations of the sliding mass, I found that the momentum transfer between slide and water depends on the mass of the submerged slide material rather than the initial slide mass (Equations (3.31) and (3.32)). In addition, when analyzing the experimental data, I found it more convenient to relate wave features to the immersed masses rather than the initial masses. I defined the *effective mass* m_E, defined as the immersed part's mass when the wave height reached its maximum. This definition also more closely reflects the physics of the problem at hand.

I examined the use of the effective mass and initial slide mass in predicting wave characteristics, using the empirical equations of Heller and Hager (2010) with the impulse product parameter P. In these equations, the scaled maximum wave amplitude $A_m = \frac{4}{9}\mathrm{P}^{4/5}$ and the scaled maximum wave height $H_m = \frac{5}{9}\mathrm{P}^{4/5}$, with:

$$\mathrm{P} = \mathrm{Fr} S^{1/2} M^{1/4} \cos(6/7\theta)^{1/2} \tag{4.1}$$

where Fr is the slide Froude number, M is the scaled slide mass, S is the scaled thickness, and θ is the slope angle. See Equations (3.32), (3.33), and (3.34) for the expressions of M, S and

Fr, respectively. By using the effective slide mass m_E instead of the initial slide mass m_I to calculate M, we were able to obtain better correlations between the scaled maximum wave amplitude A_m (or the scaled maximum wave height H_m) and the slide mass (see Figure 4.2). While the question of effective mass primarily concerned viscoplastic flows, it also affected polymer-water balls, but to a lesser extent. The effective mass of water balls varied almost linearly with their initial slide mass, so I used this variable for both materials.

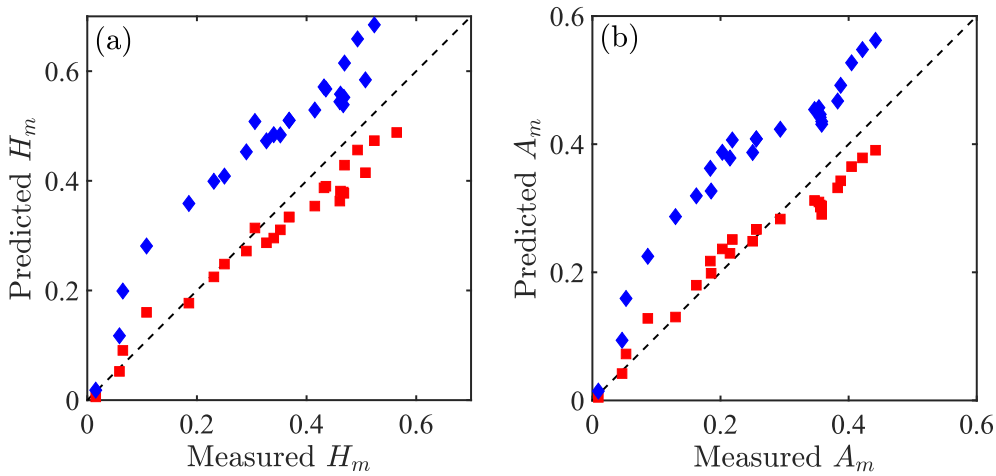

Figure 4.2 – Comparison of (a) H_m and (b) A_m predicted using m_E and m_I. Blue diamonds and red squares denote the predicting results obtained with m_E and m_I, respectively.

Figure 4.3 shows the effective mass m_E in response to the initial slide mass m_I, with the slope length l_s ranging between 0.85 and 1.05 m, the yield stress τ_c = 60, 75, and 90 Pa corresponding to the concentration of Carbopol c = 2.0%, 2.5%, and 3.0%, initial slide mass $2.0 < m_I < 5.8$ kg, and slope angle $\theta = \pi/4$ and $\pi/6$. Within this set of range of experiments, the ratio of the effective mass to the initial slide mass as the *effective ratio* R_E varied in the range of 10% to 30%, that is, 10% to 30% of the slide material engaged in the leading wave generation. R_E increases with the increase of the slope angle θ, and with the decrease of the slope length l_s and the yield stress τ_c. Carbopol gels with higher concentrations (and thus yield stress) deposited more material along the chute, so the effective mass entering into the basin was reduced. In addition, the effective mass reduced with longer slope length or lesser initial slide mass.

4.2 Comparison of waves generated by viscoplastic and granular slides

The slide material's properties significantly affect the momentum transfer from the slide material to the body of water. One major hypothesis from previous comparisons of waves generated by rigid blocks and granular slides was that the material's deformability plays a key part in wave formation. Indeed, blocks are not only rigid, but they are also cohesive, whereas

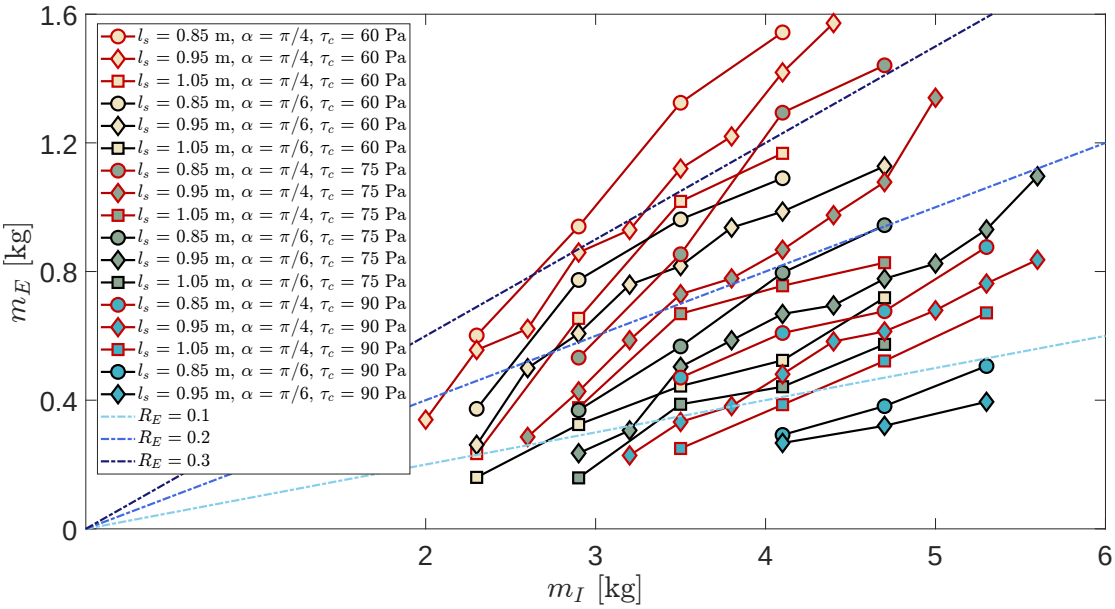

Figure 4.3 – The effective mass m_E versus the initial mass m_I with l_s = 0.85 m, 0.95 m, 1.05 m; $\alpha = \pi/6, \pi/4$; τ_c = 60 Pa, 75 Pa, 90 Pa; $2 < m_I < 5.8$ kg.

granular media are deformable and cohesionless. I compared waves generated by Carbopol (viscoplastic material) and water balls (granular material), to shed light on the effect of slide cohesion on wave features.

4.2.1 Empirical equations

Following the tradition used by a number of authors, we aggregated the dimensionless numbers into a power product of the Π_i groups, and looked for the best linear correlation between this aggregated number and a single wave feature:

$$X_n = \delta \prod_{i=1}^{N} \Pi_i^{\beta_i} \tag{4.2}$$

where X represents the scaled wave characteristics (for example, the scaled maximum wave amplitude, wave height, wave length, and wave period); Π_i indicates the explanatory variables selected, where N is the number of explanatory variables.

As presented in section 3.1.3, several dimensionless groups have been emerged from the dimensional analysis of the governing equations (see Equations (3.32) to (3.32)): the dimensionless group $\Pi_1 = \frac{m_E}{\rho_s B h_0^2}$ is the scaled effective mass M; the second group $\Pi_2 = s_0/h_0$ corresponds to the scaled slide thickness S; the third dimensionless group $\Pi_3 = u_0/\sqrt{g h_0}$ is the slide Froude number Fr. We used the maximum wave height h_m and maximum wave amplitude a_m to characterise the leading wave's features. We studied the wave features in terms of scaled variables: the scaled maximum wave height $H_m = h_m/h_0$ and scaled

maximum wave amplitude $A_m = a_m / h_0$. Thus, Equation (4.2) became:

$$X_{1,2} = \delta \Pi_X = \delta \Pi_1^{\beta_1} \Pi_2^{\beta_2} \Pi_3^{\beta_3} \tag{4.3}$$

where δ and $\beta_{1,2,3}$ denote the regression parameters, and $X_{1,2} = H_m, A_m$. In addition, many other combinations are possible. For instance, Zitti et al. (2016) showed that regressions $X = aQ^b$, with $Q = \Pi_1 \mathrm{Fr}$, closely captured their experimental trends.

4.2.2 Wave characteristics

Wave amplitude and height

We first studied how the slide's rheological behavior affected wave formation. Figure 4.4 shows how the scaled maximum wave amplitude A_m and height H_m varied with the dimensionless group $Q = \Pi_1 \mathrm{Fr}$ for Carbopol at concentrations of 2.0%, 2.5% and 3.0%. As underlined above, we used effective slide masses rather than initial slide masses in the regression analyzes, which explains why the Carbopol concentration had little effect on the trend $A_m(Q)$. This turned out to be a decisive advantage when comparing the results of Carbopol gels and polymer-water balls.

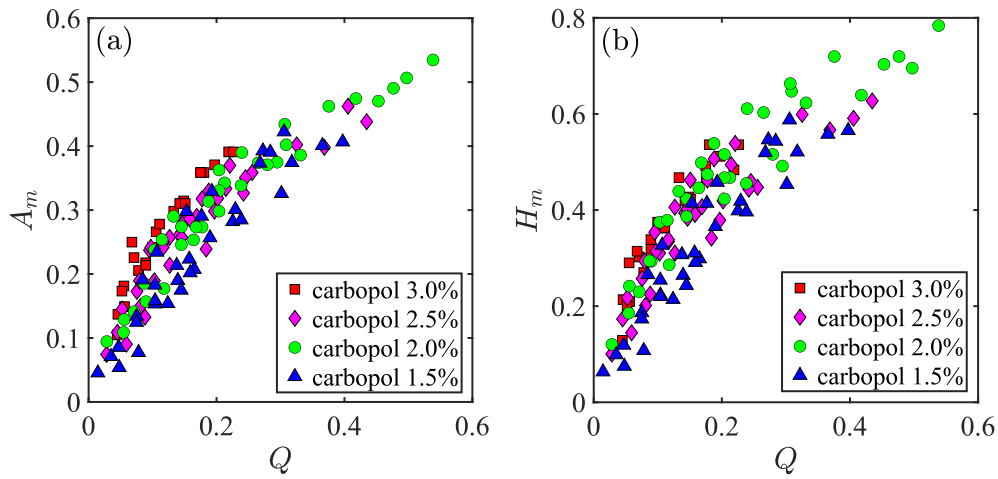

Figure 4.4 – Variations in (a) the scaled maximum wave amplitude A_m and (b) the scaled maximum wave height H_m relative to Q for Carbopol (at concentrations of 3.0%, 2.5%, 2.0%, and 1.5%), respectively.

Figure 4.5 shows the variations in the scaled maximum wave heights H_m relative to the dimensionless groups Π_i ($i = c$ or w) and Q for the Carbopol gels and polymer-water balls. Regardless of the dimensionless group used, Carbopol gels generated larger H_m values than the polymer-water balls. The mean deviation was approximately 50% in our experiments. The

regression curve that best matched the experimental trends for Carbopol gels was:

$$H_m = 1.019\Pi_c, \quad \text{with} \quad \Pi_c = \Pi_1^{0.123}\Pi_2^{0.617}\Pi_3^{1.748} \tag{4.4}$$

and for polymer-water balls:

$$H_m = 0.267\Pi_w, \quad \text{with} \quad \Pi_w = \Pi_1^{0.164}\Pi_2^{0.008}\Pi_3^{1.004} \tag{4.5}$$

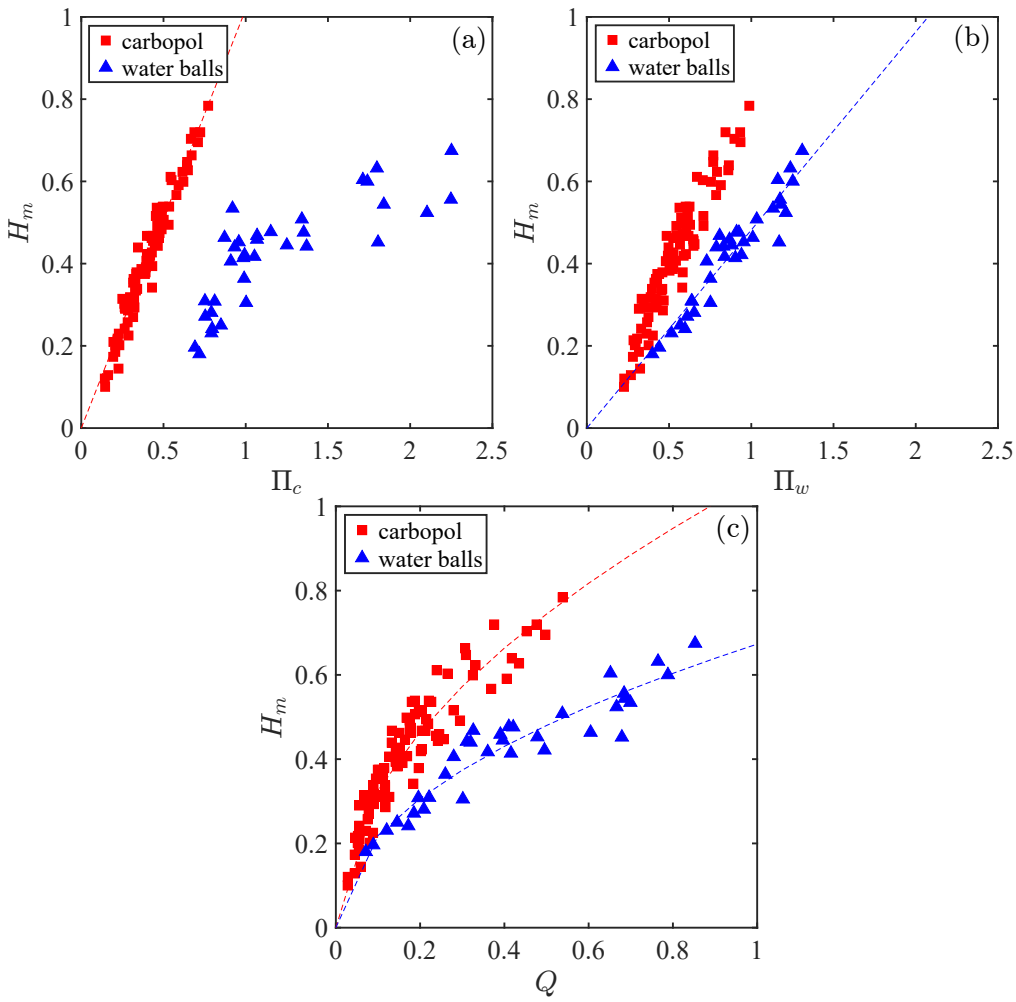

Figure 4.5 – Variations in scaled maximum wave heights H_m relative to three combinations of dimensionless groups: (a) $\Pi_c = \Pi_1^{0.123}\Pi_2^{0.617}\Pi_3^{1.748}$, (b) $\Pi_w = \Pi_1^{0.164}\Pi_2^{0.008}\Pi_3^{1.004}$, and (c) $Q = \mathrm{Fr}\Pi_1$.

The variations in the maximum scaled wave amplitude A_m with Π_i ($i = c$ or w) and Q are shown in Figure 4.6. When using Π_i, we found the regression equations for Carbopol:

$$A_m = 1.538\Pi_c, \quad \text{with} \quad \Pi_c = \mathrm{Fr}^{1.012}\Pi_1^{0.319}\Pi_2^{0.750} \tag{4.6}$$

and for polymer-water balls:

$$A_m = 0.725\Pi_w, \quad \text{with} \quad \Pi_w = \mathrm{Fr}^{0.611}\Pi_1^{0.518}\Pi_2^{0.255} \tag{4.7}$$

The wave amplitudes were 30% higher for the Carbopol gels than for the polymer-water balls.

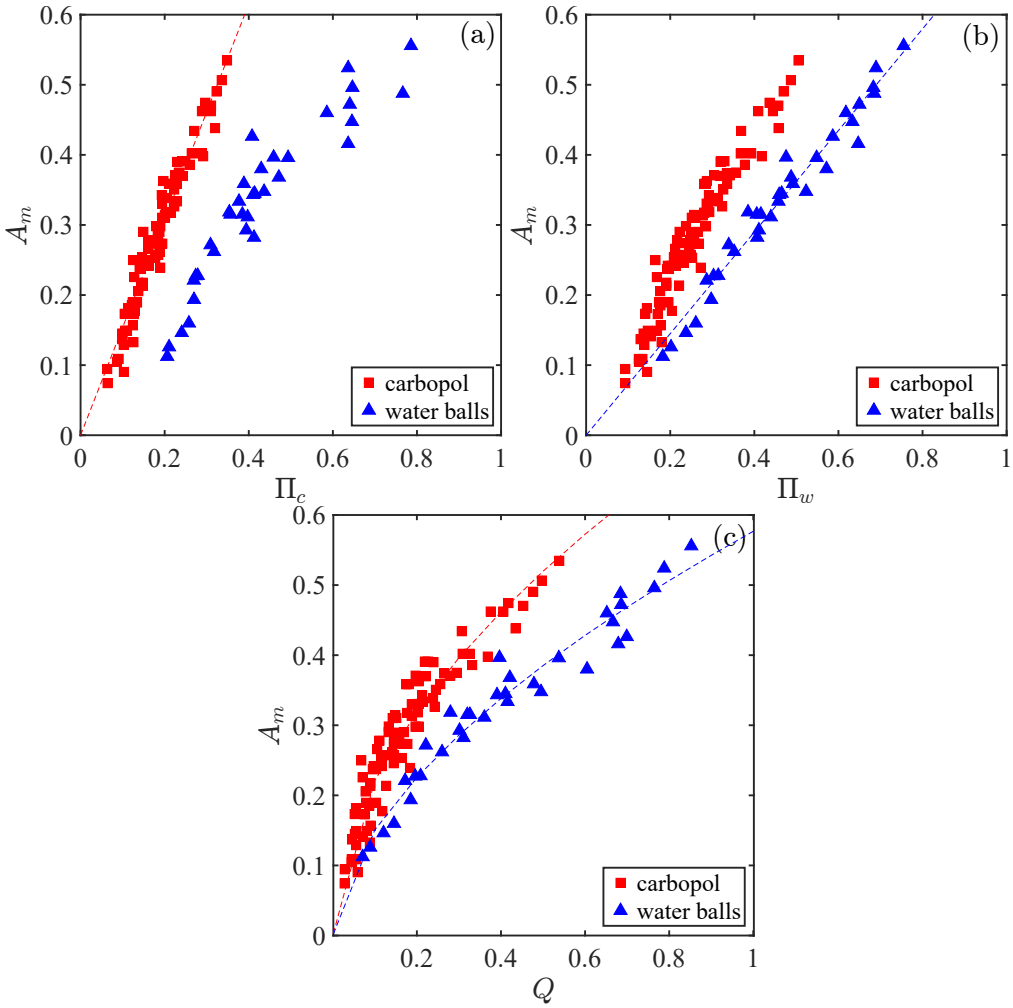

Figure 4.6 – Variations in scaled maximum wave amplitudes A_m relative to three combinations of dimensionless groups: (a) $\Pi_c = \Pi_1^{0.319}\Pi_2^{0.750}\Pi_3^{1.012}$, (b) $\Pi_w = \Pi_1^{0.518}\Pi_2^{0.255}\Pi_3^{0.611}$, and (c) $Q = \mathrm{Fr}\Pi_1$.

Wave nonlinearity

I now examine each material's wave type. The degree of nonlinearity for impulse waves can be qualified using the A_m/H_m and L/H_m ratios (Heller and Hager, 2011). According to Zweifel (2004), strongly nonlinear waves correspond to the range $0.9 < A_m/H_m < 1.0$, moderately nonlinear waves to $0.6 < A_m/H_m < 0.9$, and weakly nonlinear waves to $0.4 < A_m/H_m < 0.6$.

Figure 4.7 (a) shows how scaled maximum wave amplitudes A_m varied relative to the scaled maximum wave heights H_m. The degree of nonlinearity was slightly higher for Carbopol gels than for polymer-water balls (see Figure 4.7 (a)). Figure 4.7 (b) shows the variations in the A_m/H_m ratio relative to Q. As the A_m/H_m ratio fell within the 0.6–0.9 range, the impulse waves generated by the Carbopol gels and polymer-water balls were classified as moderately nonlinear solitary waves.

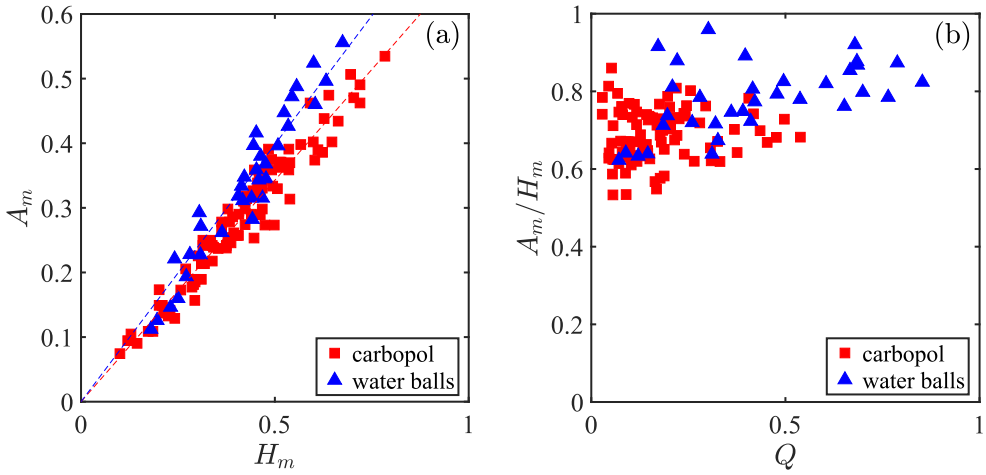

Figure 4.7 – (a) Variations in the scaled maximum wave amplitudes A_m relative to scaled maximum wave heights H_m. (b) Variations in A_m/H_m relative to the dimensionless group Q.

A similar process was used with the ratio between the scaled maximum wave length $L = \ell_m/h_0$ and the scaled maximum wave height H_m (see Figure 4.8). The maximum wave length ℓ_m was defined as the distance between the two points associated with zero crossings (i.e., still-water level). One interesting feature was that waves generated by the Carbopol gels were much more nonlinear than those formed by the polymer-water balls when we consider the L/H_m values in Figure 4.8(b). For the polymer-water balls, we found $4 < L/H_m < 6$, but only $2 < L/H_m < 4$ for Carbopol gels–a significantly lower ratio.

Wave energy

The energy conversion factor estimates how much of the slide's kinetic energy is transferred to the wave. The slide's kinetic energy can be estimated as: $E_I = \frac{1}{2} m_E u_0^2$. The wave's energy involves two terms: its potential energy and kinetic energy. The wave's potential energy results from the displacement of the water surface from its original still position, whereas its kinetic energy is estimated from particle motion in the body of water. The wave's potential and kinetic energies are:

$$E_p = \frac{1}{2}\rho_f g b \int_{x_{\text{ini}}}^{x_{\text{fini}}} \eta^2(x,t)\,\mathrm{d}V_x \tag{4.8}$$

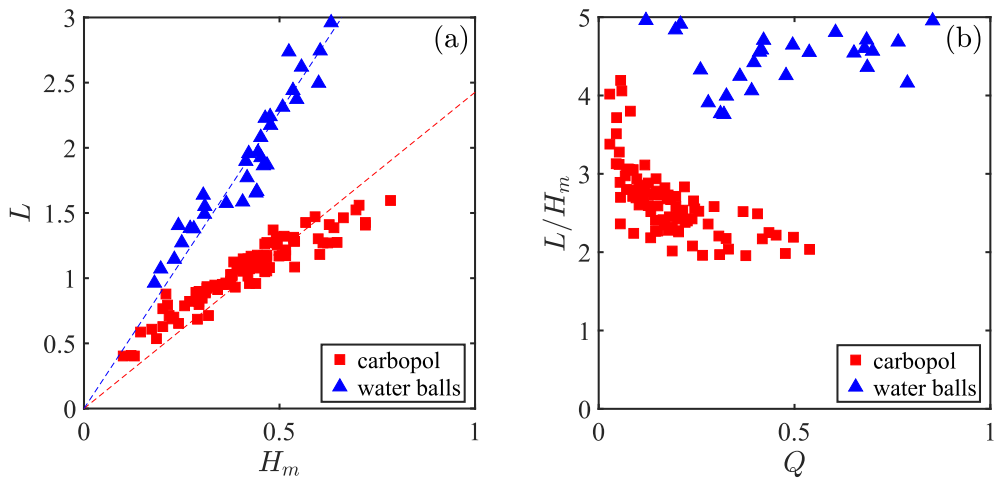

Figure 4.8 – (a) Variations in the scaled maximum wave amplitudes A_m relative to the scaled maximum wave lengths L. (b) Variations in L/H_m relative to the dimensionless group Q.

and

$$E_k = \frac{1}{2}\rho_f g b \int_{x_{\text{ini}}}^{x_{\text{fini}}} (h+\eta)\, \bar{u}_w^2 \mathrm{d}V_x \tag{4.9}$$

where u_0 denotes the slide velocity at impact, ρ_f is the water density, g is the gravity acceleration, and η denotes the water surface. Here, we assumed equipartition of the potential and kinetic energies (as in the case of linear waves) and set $E_k = E_p$ (Mohammed and Fritz, 2012; Zitti et al., 2016).

Figure 4.9 displays how the wave's maximum potential energy E_p varied relative to the slide's kinetic energy E_I. I have also plotted the empirical formulas that captured the experimental trends between the wave's maximum potential energy and the slide's kinetic energy: $E_p = 0.092E_I$ for Carbopol gels and $E_p = 0.096E_I$ for polymer-water balls. The empirical formulas for Carbopol and polymer-water balls were quite close to each other. Previous studies have reported that energy conversion factors ranged from 1 to 85.7% for granular slides (Fritz, 2002a; Heller, 2007), and from 2 to 50% for blocks (Ataie-Ashtiani and Nik-Khah, 2008; Kamphuis and Bowering, 1970). The energy conversion factor also exhibited considerable variations depending on the initial conditions. In our experiments, the energy conversion factors for Carbopol gels and polymer-water balls were similar, ranging from 9 to 30%, with an average of 19%. One possible explanation for the discrepancy between these experiments is that earlier studies used the slide's initial mass when computing its kinetic energy, whereas we used the slide's effective mass.

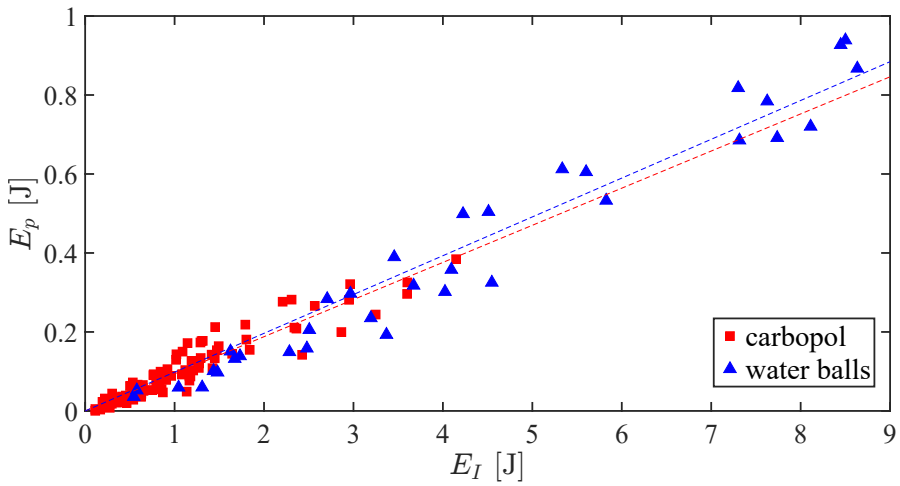

Figure 4.9 – Variation in the wave's maximum potential energy E_p relative to the slide's kinetic energy E_I.

4.2.3 Discussions

Multicollinearity

Multicollinearity is a phenomenon where one explanatory variable in a multiple regression model can be linearly predicted from the others with a substantial degree of accuracy. This may lead to the problem that the multiple regression's coefficient estimates change erratically in response to small changes in the model. The natural logarithmic form of Equation (4.3) can be written as:

$$\ln X = \ln \delta + \beta_1 \ln \Pi_1 + \beta_2 \ln \Pi_2 + \beta_3 \ln \Pi_3 \tag{4.10}$$

The coefficients $\ln\delta$, β_1, β_2, and β_3 were estimated using the least squares (linear regression) method based on experimental data. As length [L] was scaled by the still-water depth h_0, h_0 appears in the three aggregated parameters Π_1, Π_2 ,and Π_3, and specifically, they are correlated with h_0^{-2}, h_0^{-1}, and $h_0^{-1/2}$, respectively. The high correlations among explanatory variables may result in multicollinearity during the linear regression. However, to date, none of the studies using empirical equations has discussed multicollinearity.

To estimate the correlations between each pair of explanatory variables, we calculated their Pearson correlation coefficients r. As illustrated in Figure 4.10, the Pearson correlation coefficient R_P between Π_1 and Π_2 is relatively high ($R_P = 0.69$), however, it is still under the upper limit of 0.8. Furthermore, to determine how influential the water depth h_0 was in wave generation, we determined the sensitivity of the maximum wave amplitude a_m to a ±20% change in each of the following parameters (taken in isolation from the others): slide volume on impact V_s, slide velocity on impact u_0, slide thickness s_0, and still-water depth h_0. We obtained similar results to those obtained by Heller et al. (2009): the a_m variations due to changes in these parameters were smaller than 20%, and a_m was more sensitive to u_0 and V_s rather than h_0. Therefore, we can consider that the multicollinearity lies within an acceptable

range.

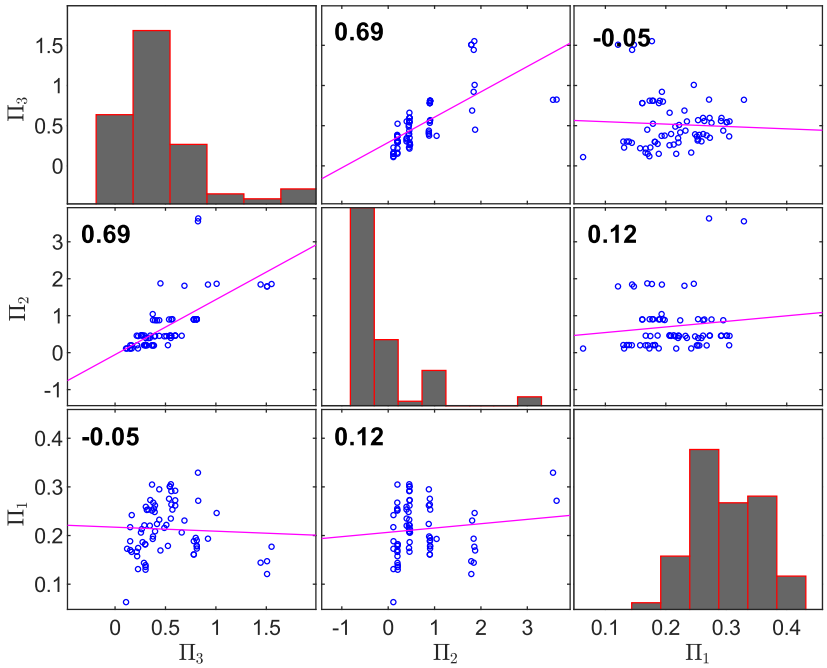

Figure 4.10 – Correlation matrix of explanatory variables Π_1, Π_2, and Π_3 in Equation (4.3).

Effect of slide cohesion

Within the range of Carbopol concentrations tested, no significant rheological effects on wave amplitudes and heights were detected. As presented in Figure 4.6, wave amplitudes generated by Carbopol gels were approximately 30% larger than those generated by polymer-water balls. This behavior was similar to that observed with rigid blocks and granular materials by Ataie-Ashtiani and Nik-Khah (2008): blocks formed waves whose amplitudes were up to 35% larger than for granular slides. Differences in wave characteristics have been considered to arise due to the materials' deformability (for example, blocks are rigid, whereas granular slides are deformable). In the present case, both the Carbopol gels and polymer-water balls were deformable, but Carbopol gels generated the waves with the highest amplitudes. The main difference between Carbopol gels and polymer-water balls lay in their cohesion. Carbopol gels moved as united slides because they were cohesive, whereas polymer-water balls dispersed into numerous particles after entering the body of water. In this respect, material cohesion had more influence on how the slide momentum was transferred to the body of water than did slide deformability.

In addition to the slide cohesion and deformability, the slide permeability, which is related to the material porosity, is likely to influence wave formation. Lindstrøm (2016) compared impulse waves generated by four granular slides with different porosities, and found that

granular slides with smaller porosities generated larger amplitudes. That study deduced that permeability played a key part in wave formation: smaller permeability implies that the water filling the pore space cannot instantaneously drain out upon slide impact, and in this case, the slide tends to behave like a rigid body. By contrast, Heller and Hager (2010) observed that the grain diameter had negligible effects on wave formation, which was why they excluded the grain diameter from the list of governing parameters. Evers and Hager (2015) noted that the waves generated by packed slides were similar to those generated by free granular material.

4.3 Wave prediction under complex configurations

In contrast to empirical equations that specified the mathematical operators in advance, the data-driven approach relies solely on datasets and does not require any assumptions about functional form or physical constraints. The present study applied an artificial neural network (ANN) method, one of the most commonly used data-driven methods, to cope with wave prediction under complex configurations. The dataset consists of experiments conducted using Carbopol, water balls, and mixtures thereof. After validating the ANN model by comparing its prediction accuracy with that of empirical equations, we applied the model to two scenarios: (i) predicting wave characteristics from the parameters of landslides initially at rest on the slope and (ii) integrating the parameters of different categories of slide mass material into one model (the Bingham number for viscoplastic material and the grain diameter for granular material).

4.3.1 Model development

Using the same variables as empirical Equation (4.3), the three neurons in the input layer and the two neurons in the output layer of the artificial neural network (ANN) model were:

- 3 inputs: Π_1, Π_2, and Π_3
- 2 outputs: A_m and H_m

I first selected a dataset of 291 experiments conducted with Carbopol to develop the model. 80% of the samples (233) were selected as training data for model construction and 20% (58 samples) were saved as test data for model validation, providing an independent measure of ANN performance after training. Samples for each group were selected randomly.

I used a basic three-layer network structure; namely, one input layer, one hidden layer, and one output layer. To select the optimal number of neurons in the hidden layer, we set a random number of neurons and ran the program, determining their performance by the coefficient of determination R^2 (see Equation (3.48)). Each run was repeated 5 times and R^2 was calculated by eliminating the maximum and minimum coefficients of determination and averaging the results of the remaining three tests. As shown in Figure 4.11, the R^2 of both H_m

and A_m reached their maximum values when the hidden layer contained 6 neurons. Thus, the optimum network for the present study was a 3–6–2 structure (input–hidden–output).

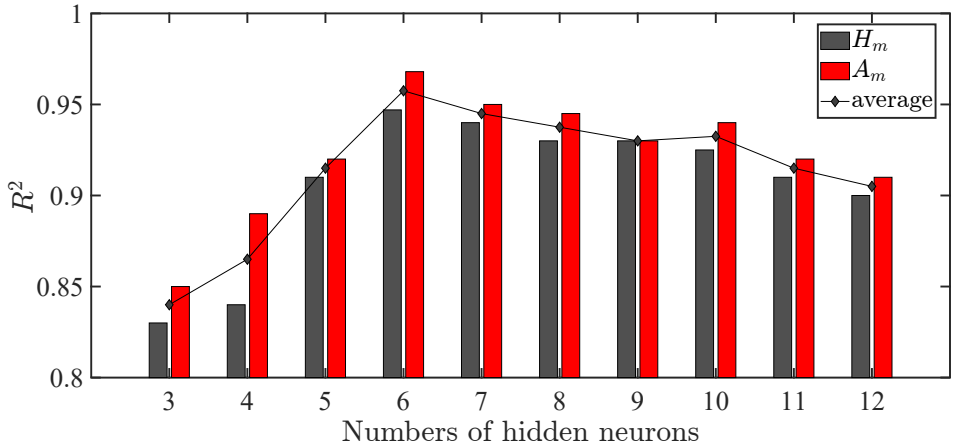

Figure 4.11 – Variation of R^2 versus the number of neurons in the hidden layer.

Model training was constrained by the following indicators: the maximum epoch number was initially set to 100; the objective mean square error (MSE)(see Equation (3.49)) was set to 1×10^{-4}; the minimum gradient was set to 1×10^{-5}; and the maximum number of validation fails, which represents the number of successive iterations that the validation performance fails to decrease, was initially set to 6. Training would stop once one of the indicators mentioned above reached its initial value. In the present study, training stopped when the number of validation fails reached 6. Figure 4.12 illustrates the evolution of these indicators (that is, gradient, validation fails, and MSE) at each epoch until the training is stopped.

In Figure 4.12 (c), the MSEs of the training data and the test data were counted separately. The curves of the evolution of the MSE for these three data series were very close, indicating the model's high level of adaptability. The best validation performance was an MSE = 0.00025337 at epoch 43, and the training terminated at epoch 48 as the number of validation fails reached 6. The gradient = 0.0011736 at epoch 48. Figure 4.13 displays a histogram of the residuals between the predicted A_m and the observed A_m. The probability density of the residuals approximately follows a Gaussian distribution.

Figure 4.14 displays the observed A_m and H_m versus the predicted data modeled using the ANN model and the empirical equations. The empirical equations of A_m and H_m for waves generated by Carbopol were Equation (4.6) and Equation (4.4), respectively. The R^2 of A_m and H_m of the test data in the ANN model were 0.9682 and 0.9479, respectively; the R^2 of A_m and H_m of the test data predicted by the empirical equations were 0.9214 and 0.9062, respectively. As shown in Table 4.2, the ANN model outperformed the best-fitting empirical equation. In addition, the R^2 of A_m was always slightly higher than that of H_m in both models, which may result from measurement errors in the experiments (Meng, 2018; Meng and Ancey, 2019).

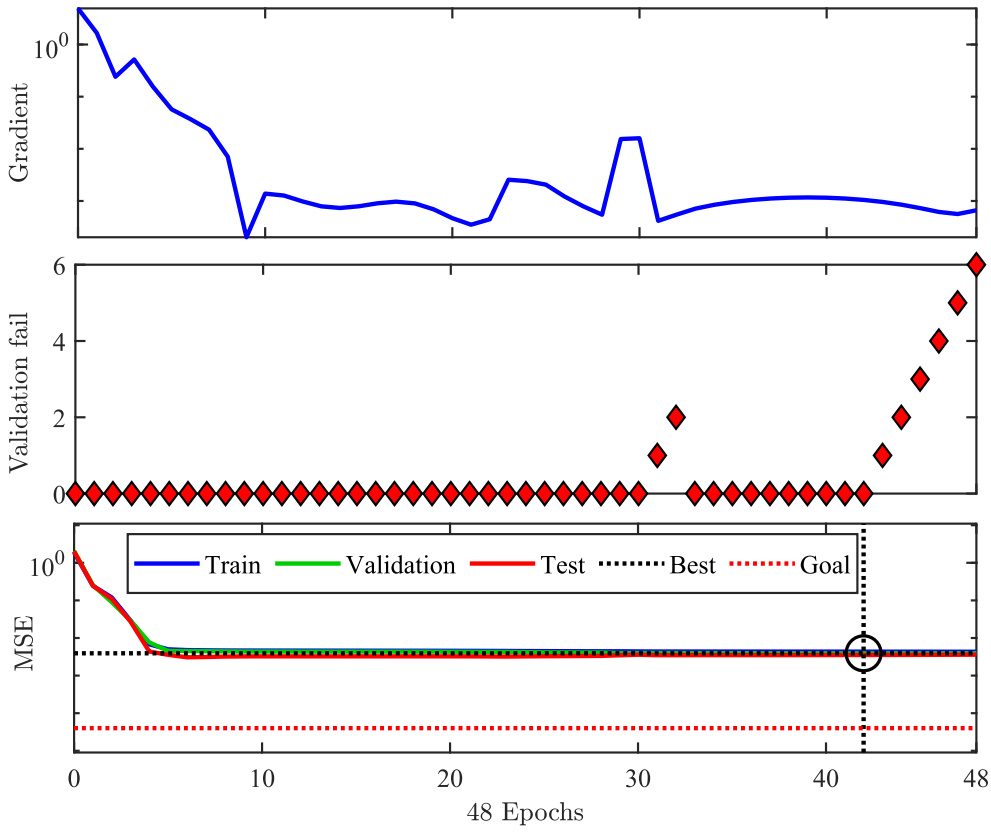

Figure 4.12 – Variations in (a) the gradient, (b) the number of validation fails, and (c) MSE, against epochs.

4.3.2 Prediction of wave characteristics from initial slide parameters

Previously, empirical or semi-empirical equations determined wave characteristics from the mass slide features on impact (illustrated as Stage II in Figure 2.1), and most equations were established in the form of power-law equations of several dimensionless groups (see Equation (4.3)). When we predict the wave characteristics from the slide features at Stage I, it is difficult to provide physical constraints on the mathematical structure of predictive equations because of the complex physical mechanisms involved in the whole process. In this case, assuming a functional form for the prediction equation in advance might be problematic. Therefore, a data-driven approach that relies strictly on the data rather than on a fixed form equation is preferable, and the ANN method fits this requirement. The process involves the following parameters:

$$\eta(x,t) = \eta(\tau_c, K, n, l_0, s_0, l_s, h_0, \theta, \rho_f, \rho_s, t, g) \tag{4.11}$$

The slide mass's rheological parameters include τ_c, K, and n. Although they have little effect on the slide mass–water interaction and wave formation (Meng and Ancey, 2019), they have great effects on the slide mass flowing down the slope. The Pearson correlation coefficients between each pair of these three parameters were all above 0.9 (see Table 4.1), indicating that

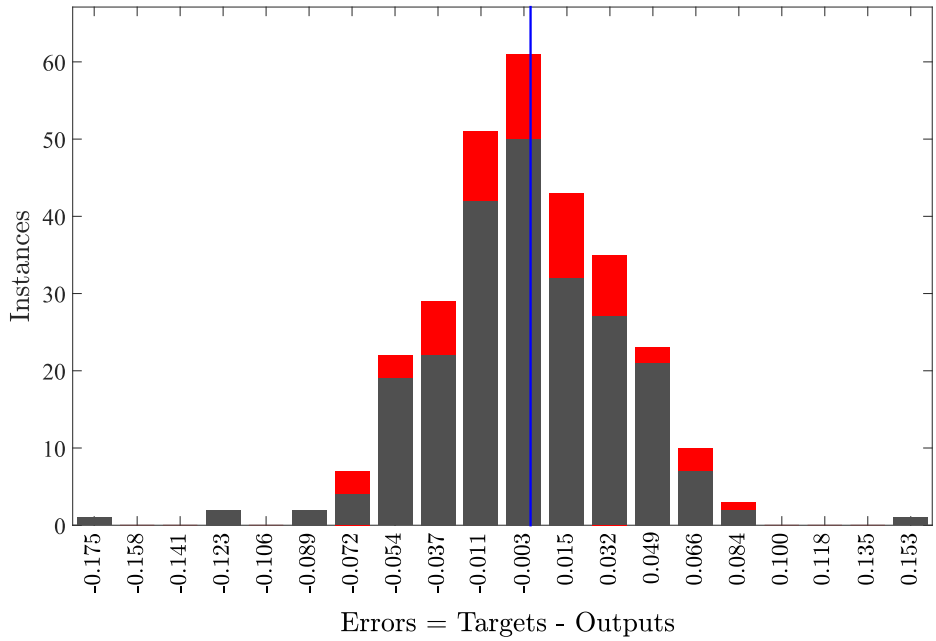

Figure 4.13 – Error histogram of A_m with 20 bins. The red part denotes test data and the grey part denotes training data.

all three parameters correlated highly. Therefore, we selected the yield stress τ_c, namely the stress at which the material starts yielding, to represent the rheological parameters.

Table 4.1 – The Pearson correlation coefficients between τ_c, K, and n.

	τ_c	K	n
τ_c	1	0.9739	0.9604
K	0.9739	1	0.9633
n	0.9604	0.9633	1

Figure 4.15 provides an initial insight into how the wave characteristics depend on the rheological properties of the slide mass and on its parameters at the initial stage. It shows experimental data with the yield stress set at $\tau_c = 41$, 62, and 80 Pa. Overall, the maximum wave amplitude a_m increased with rising yield stress τ_c and initial slide mass m_I, and decreased with the slope length l_s.

$\epsilon = \frac{l_*}{h_*}$ and $\varsigma = \frac{s_*}{h_*}$ are aspect ratios for the l-axis to the y-axis, and for the s-axis to the y-axis, respectively. The natural choice for defining the typical scale introduced by these ratios was to select the dimensions of the reservoir: $l_* = l_0$, $h_* = h_0$, and $s_* = s_g$. The Bingham number can be expressed as $Bi = \frac{\tau_c}{K(v_*/s_*)}$, which is a dimensionless yield stress (relative to the viscous forces). We assumed that the viscoplastic flow reached a near-equilibrium regime, where viscous forces balanced gravity acceleration, and the velocity scale was then $v_* = (\rho_s g \sin\theta / K)^{1/n} s_*^{1+1/n}$. The Bingham number then became $Bi = \frac{\tau_c}{\rho_s g s_g \sin\theta}$ (see Ancey and

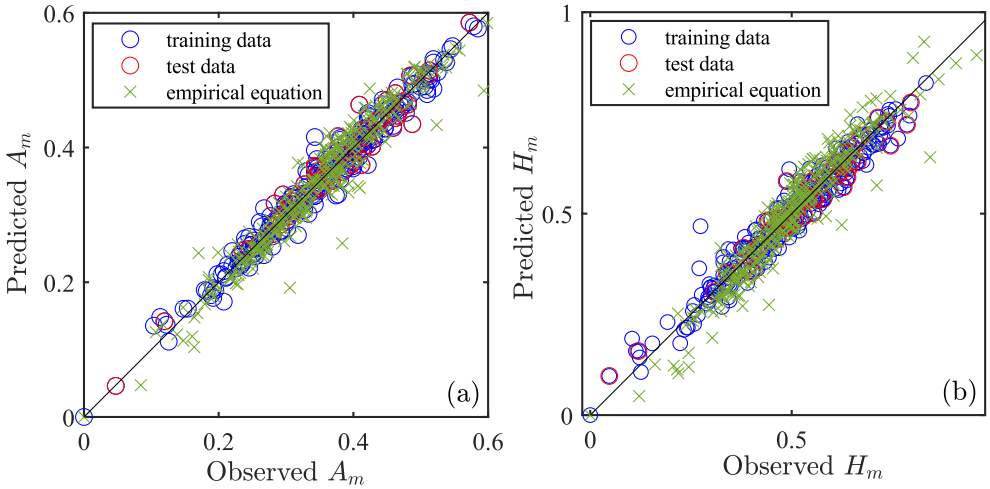

Figure 4.14 – Plot of observed and predicted (a) A_m and (b) H_m, for the empirical equations and the ANN model. Training data and test data in the ANN model are displayed separately.

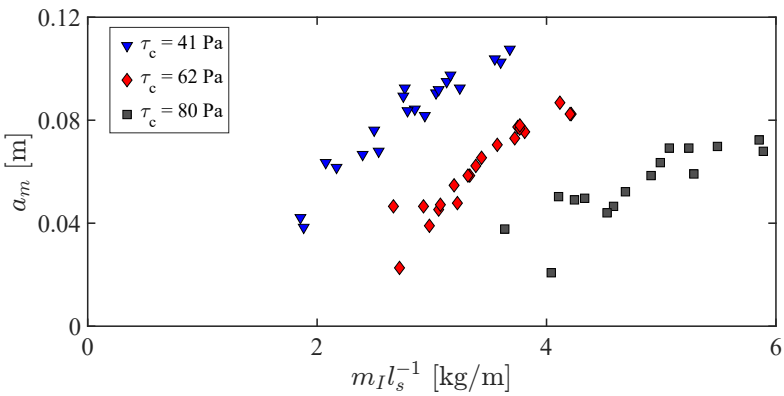

Figure 4.15 – Variations in wave amplitude a_m against $m_I l_s^{-1}$, with the water depth $h_0 = 0.2$ m and slope angle $\theta = 45°$.

Cochard (2009) for further information).

The dimensions involved in Equation (4.11) are length [L], mass [M], and time [T]. We chose three scaling parameters: water density ρ_f, still-water depth h_0, and gravitational acceleration g (Zitti et al., 2015). Thus, the dimensionless form can be expressed as:

$$\eta' = \frac{\eta(x,t)}{h_0} = \eta'\left(\frac{\tau_c}{\rho g s_0 \sin\theta}, \frac{l_0}{h_0}, \frac{s_g}{h_0}, \frac{l_s}{l_0}, \theta, \frac{\rho_s}{\rho_f}\right) \tag{4.12}$$

where η' is the scaled free-water surface elevation. Same as in section 4.3.1, we selected the scaled maximum wave amplitude A_m and height H_m to represent the water surface elevation. As the slide mass density ρ_s and water density ρ_f were constant throughout our experiments, $\frac{\rho_s}{\rho_f}$ can be eliminated. Therefore, there were therefore five neurons in the input layer and two neurons in the output layer:

- 5 inputs: Bi, ϵ, ς, $\frac{l_s}{l_0}$, and θ
- 2 outputs: A_m and H_m

The modeling method used was the same as in section 4.3.1. First, based on the optimal number of hidden neurons determined, a 5–10–2 network structure was developed. The experimental data were then divided into training data and test data. Finally, the ANN model was trained using the training data and validated using the test data. The coefficient of determination R^2, the mean square error (MSE), and the sum of squares due to error (SSE) of A_m were 0.8983, 0.00089, and 0.2591, respectively. The R^2, MSE, and SSE of H_m were 0.8497, 0.00295, and 0.8483, respectively. The expressions of R^2, MSE, and SSE have been introduced in Equations (3.48) to (3.50). Because $R^2 > 0.8$, the present model is validated. However, compared with the scenario that predicted wave characteristics from the slide mass parameters on impact, the prediction accuracy of the ANN method in the present scenario was lower. The more complicated the physical process is, the more information could be lost in the prediction.

4.3.3 Waves generated by viscoplastic-granular mixtures

In this section, I quantified the characteristics of waves generated by viscoplastic-granular mixtures, with the percentage of Carbopol in volume varying symmetrically (0, 20, 50, 80, and 100%). As shown in Figure 4.16, larger waves are generated with higher proportions of Carbopol in the mixture, which implies that the slide mass material's composition influenced wave generation. Here, to provide identical criteria for all slide mass materials, I quantified the slide mass properties using a universal dimensionless group named the *Impulse product parameter* P, which was proposed by Heller and Hager (2010):

$$\mathrm{P} = \Pi_1^{1/4}\Pi_2^{1/2}\Pi_3\cos(6/7\theta)^{1/2} \tag{4.13}$$

where Π_1, Π_2, and Π_3 denote the same parameters as in Equation (4.3). One issue that should be noted is that the properties of granular slides are usually represented by their grain diameters, whereas the rheological behavior of viscoplastic materials is commonly described using the yield stress. It is difficult to integrate these two parameters into one equation in the form of a power-law equation. To overcome this limitation and provide a compatible model for these parameters, I applied the ANN method to avoid assuming the functional form of a prediction equation. Here, I predicted the wave characteristics from the mixture's parameters on impact.

As highlighted above, the dimensionless parameters in modeling experiments with a single material commonly involve the relative slide mass Π_1, relative slide thickness Π_2, and slide Froude number Π_3. To quantify the properties of mixed viscoplastic and granular slides, we introduced the following dimensionless groups: the Bingham number Bi = $\frac{\tau_c}{\rho_s g s_g \sin\theta}$, representing the rheological properties of a cohesive material; the scaled diameter of the

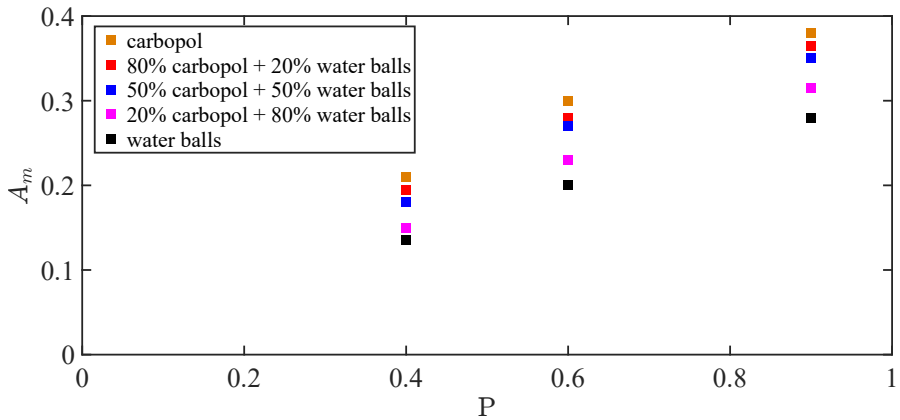

Figure 4.16 – Effects of slide mass material composition on the scaled maximum wave amplitude A_m.

granular slide mass $D_s = \frac{d_g}{h_0}$, where d_g is the diameter of a granular particle; the volume ratio of the viscoplastic material in the mixture $R_V = \frac{V_s}{V_g+V_s}$, where V_s is the volume of the viscoplastic slide mass and V_g is the volume of the granular slides; and the density ratio between the two materials, which is a constant in the present study.

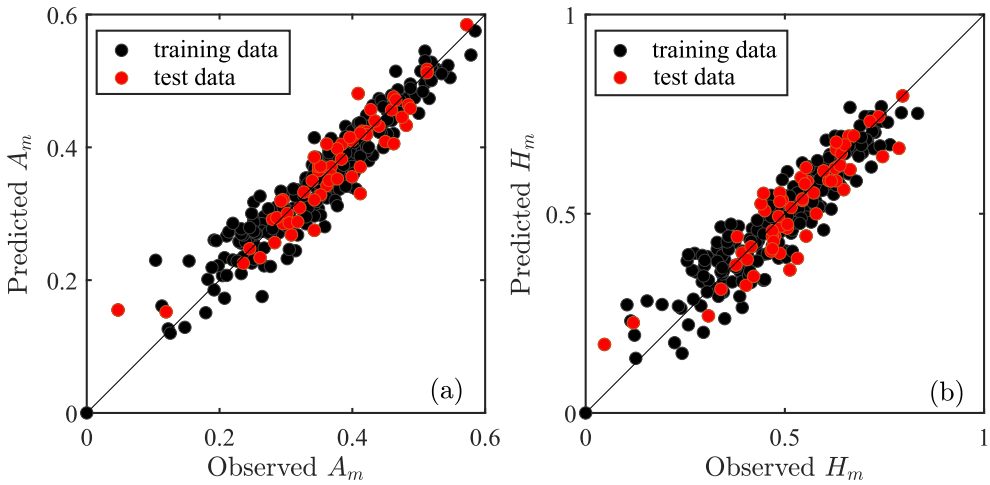

Figure 4.17 – Predicted (a) A_m and (b) H_m with a 6–8–2 ANN model versus experimental data. Training data and test data in the ANN model are displayed separately.

Hence, the input layer contained 6 neurons $\{\Pi_1, \Pi_2, \Pi_3, \text{Bi}, D_s, \text{and } R_V\}$, and the output layer again contained $\{A_m \text{ and } H_m\}$. Using the same method as presented in section 4.3.1, the number of hidden neurons was determined and the network's optimum structure was 6–8–2. The R^2, MSE, and SSE of A_m were 0.9325, 0.0072, and 0.2172, respectively. R^2, MSE, and SSE of H_m were 0.9173, 0.00178, and 0.6154, respectively. As R^2 of both A_m and H_m were greater than 0.8, the model can be considered as valid. The predicted A_m and H_m are illustrated against the experimental data in Figure 4.17.

4.3.4 Discussions

Model adaptability

In sections 4.3.2 and 4.3.3, we presented two applications that were difficult to model using empirical equations with a fixed functional form. One application was predicting wave characteristics from slide mass features at the initial stage I. When doing this, it is difficult to provide physical constraints on the mathematical structure of predictive equations because of the complex physical mechanisms involved in the whole process. In this case, assuming a functional form for the predictive equation in advance might be problematic. Another application was predicting waves generated by viscoplastic–granular mixtures. The properties of granular slides are usually represented by their grain diameters, whereas the rheological behaviors of viscoplastic materials are commonly described using yield stress. It is difficult to integrate these two parameters into one equation in the form of a power-law equation.

Both these scenarios can easily be adapted using the ANN method's high prediction accuracy (see Table 4.2). This clearly demonstrates the advantage of using a purely data-driven method in terms of model adaptability (and this is not limited to an ANN method). Unlike empirical equations with fixed formulae, the ANN method has no external constraints, making it a scalable open system. It also has the ability to self-update and is highly adaptable when new parameters become available or fresh constraints appear (they are not limited to the two scenarios presented in this study). With more information, richer datasets, and stronger correlations can be built from the input layer to the output layer.

Prediction accuracy

Table 4.2 concludes the coefficient of determination R^2, mean square error (MSE), and sum of squares due to error (SSE) values for each of the models. The following features are worth noting:

- The ANN model gives more precise predictions than empirical equations based on regression techniques. Using the same explanatory variables, the coefficient of determination R^2 improved from 0.9214 to 0.9682 for A_m, and from 0.9062 to 0.9479 for H_m. Of course, the improvement in prediction accuracy is not large.

- The prediction precision for A_m was greater than for H_m in predictions made with empirical equations and with the ANN models. This may be because the experimental measurement errors of wave heights h_m were larger than those for wave amplitudes a_m. Prediction precision depends not only on the prediction performance of the model selected but also on experimental accuracy.

- The predictions of wave features from the parameters at impact were better than the predictions from the parameters at the initial stage. Also, prediction precision decreased when the dataset involved combinations of different slide mass materials.

Thus, prediction precision decreased as experimental complexity increased and more parameters were involved.

Table 4.2 – The R^2, MSE, and SSE values of the described models.

	empirical equations		ANN model (i)*		ANN model (ii)**		ANN model (iii)***	
	A_m	H_m	A_m	H_m	A_m	H_m	A_m	H_m
R^2	0.9214	0.9062	0.9682	0.9479	0.8983	0.8497	0.9325	0.9173
MSE	0.00081	0.00197	0.00025	0.00107	0.00089	0.00295	0.00072	0.00178
SSE	0.2571	0.6266	0.0865	0.3088	0.2591	0.8483	0.2172	0.6154

* prediction from dimensionless parameters on impact.
** prediction from the slide's initial parameters.
*** prediction from data with several slide materials.

5 Temporal analysis of the slide-water interaction

Based on the results of PIV experiments conducted with Carbopol, this chapter provides a temporal analysis of how the viscoplastic fluid interacts with water. Section 5.1 presents the time series data of the slide parameters on impact including the thickness and velocity passing through the shoreline and the submerged slide mass. Section 5.2 presents the interaction forces between the slide phase and the water phase as well as the momentum variations of the two phases in a selected control volume. Section 5.3 estimates the time series data of wave characteristics from slide parameters based on the panel data model.

5.1 Temporal slide parameters on impact

Section 3.1.2 presented theoretical expressions for the time series data of the slide's thickness $s(\hat{x}, \hat{t})$ and depth-averaged velocity $u(\hat{x}, \hat{t})$ when it moves along a chute. The sketch of the slide moving along the slope is presented in Figure 3.2. Here, the theoretical expressions of $s(\hat{x}, \hat{t})$ and $u(\hat{x}, \hat{t})$ (Equations (3.24) and (3.28)) were solved numerically using Matlab. Figure 5.1 shows the numerical solutions of $s(\hat{x}, \hat{t})$ and $u(\hat{x}, \hat{t})$ for the following specific case: the slope angle $\theta = \pi/6$ and the yield stress of slide material $\tau_c = 58$ Pa (see the figure caption for the other parameters). Both $s(\hat{x}, \hat{t})$ and $u(\hat{x}, \hat{t})$ increase with $\hat{x}$ and decrease with $\hat{t}$.

The time series data of the slide thickness at the shoreline $s(\hat{x} = l_s, \hat{t})$ is denoted by $s_0(t)$, and the depth-averaged velocity of the sliding mass at the shoreline $u_0(\hat{x} = l_s, \hat{t})$ is denoted by $u_0(t)$. The relation between t and $\hat{t}$ is:

$$t = \hat{t} - t_0 \tag{5.1}$$

where t_0 denotes the time taken from when the slide starts to move until the front of the slide material touches the shoreline. Both $s_0(t)$ and $u_0(t)$ can be measured from the PIV experiments. Figure 5.2 compares the experimental data of $s_0(t)$ and $u_0(t)$ with their theoretical values for the case displayed above. The theoretical results had good agreement with the experimental data. In the selected test, the residual r between the theoretical and experimental data was

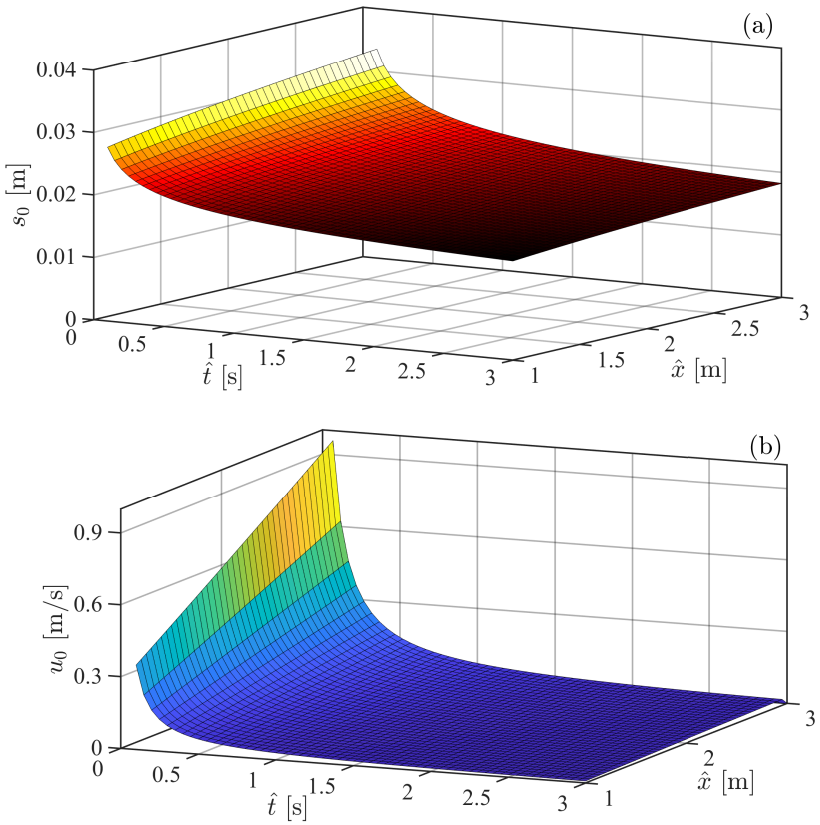

Figure 5.1 – Numerical solution of (a) slide thickness $s(\hat{x}, \hat{t})$ and (b) depth-averaged velocity $u(\hat{x}, \hat{t})$ along the chute (initial setting: $\theta = \pi/6$, $s_g = 0.4$ m, $l_0 = 0.3$ m, $n = 0.33$, $\tau_c = 58$ Pa, $\mu = 18.9$ Pa $\cdot$ s^n, and $g = 9.8$ m/s^2).

fairly low: $|r| < 2 \times 10^{-3}$ m for the slide thickness at shoreline $s_0(t)$, and $|r| < 0.2$ m/s for the depth-averaged velocity $u_0(t)$. The averages of the absolute residuals $|\bar{r}|$ were smaller than 10% of the experimental data for both $s_0(t)$ and $u_0(t)$. In addition, both $s_0(t)$ and $u_0(t)$ follow hyperbola functions. $u_0(t)$ decreased sharply since the front of the sliding mass had passed through the shoreline, whereas the decreasing tendency of $s_0(t)$ was relatively flat.

The slide mass on impact was quantified by the immersed part's mass of the slide material. Figure 5.3 (a) shows the evolution of the submerged slide mass $m_E(t)$, with the initial slide mass m_I ranging from 2.44 to 5.75 kg and the slope length l_s fixed to 0.85 m. Figure 5.3 (b) shows the time evolution of $m_E(t)$, with m_I fixed to 4 kg and l_s systematically varied from 0.80 to 0.90 m. It can be seen that the submerged slide mass $m_E(t)$ increases quickly at the beginning, and then slows down and finally stops. In addition, less than 50% of the initial slide mass has entered the body of water until the slide stops moving, while the rest of the slide material deposits along the slope.

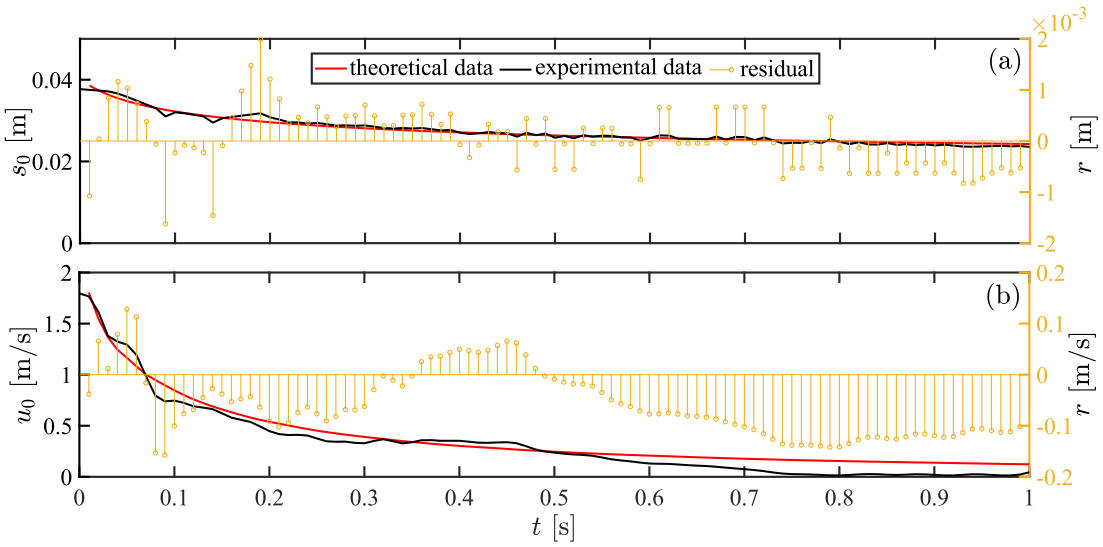

Figure 5.2 – Comparison of theoretical and experimental results of (a) $s_0(t)$ and (b) $u_0(t)$.

5.2 Momentum transfer

This section displays how the momentum is transferred from the slide phase to the water phase, by analyzing the interaction forces engaged in stopping the motion of the slide phase and the momentum variations of the two phases in the observation window.

5.2.1 Interaction forces

The forces governing the momentum transfer from the slide phase to the water phase consist of two parts: the hydrostatic force $\mathbf{F}_P$ and the drag force $\mathbf{F}_D$.

Hydrostatic force

The hydrostatic force $\mathbf{F}_P$ can be experimentally determined from the records of the slide-water interface and free water surface (see Figure 2.8). Due to the complexity of the slide-water interface's evolution, it is difficult to presume a theoretical expression for $\mathbf{F}_P$ directly. The strategy was to determine the force experimentally and then make a mathematical approximation based on the experimental data.

I first selected an observation window with a length of 0.6 m, which corresponds to the control volume V in the theoretical model. I selected four representative experiments as examples, with which I displayed the general tendencies of the results. Table 5.1 shows the initial parameters of the four selected experiments.

Figure 5.4 shows the time variation of the hydrostatic force $\mathbf{F}_P$ acting on the submerged slide material for the four selected experiments. The horizontal projection of the hydrostatic

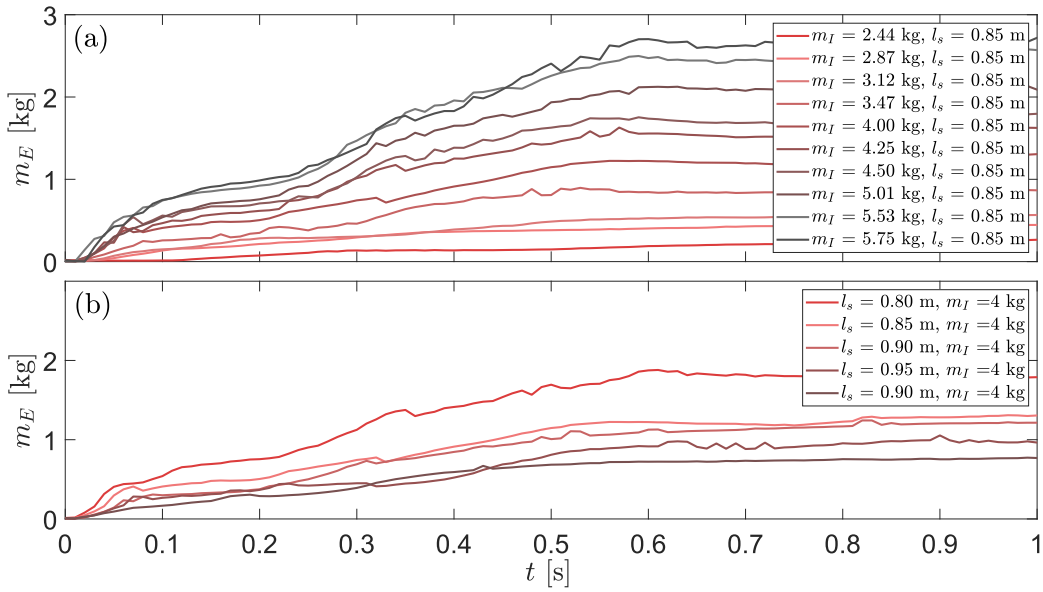

Figure 5.3 – Time variation of the submerged slide mass $m_E(t)$ with varying (a) initial slide mass m_I and (b) slope length l_s.

Table 5.1 – Initial parameters of the selected tests which served as examples.

Test number	C [%]	l_s [m]	α [-]	m_I [kg]	h_0 [m]
Test 32	2.5	1.05	$\pi/4$	3.0	0.2
Test 40	2.5	0.95	$\pi/4$	3.5	0.2
Test 42	2.5	0.85	$\pi/4$	4.0	0.2
Test 46	2.5	0.85	$\pi/4$	4.5	0.2

force $\mathbf{F}_P$ is denoted by $F_{p,x}$, and the vertical projection of $\mathbf{F}_P$ is denoted by $F_{p,y}$. At the very beginning, both $F_{p,x}$ and $F_{p,y}$ increased quickly. Then, $F_{p,x}$ and $F_{p,y}$ begun to decrease, with the submerged slide starting to stop and the leading wave starting to decay. After the slide had stopped, $F_{p,x}$ and $F_{p,y}$ were finally balanced with the gravity and the anchorage force provided by the slope.

As mentioned in section 3.1, the transfer of momentum in horizontal direction plays a key role in wave formation, so I emphasized on the horizontal projection of the hydrostatic force $F_{p,x}$. As shown in Figure 5.4, $F_{p,x}$ approximately follows a parabola function that increases quickly at the beginning and begins to decrease after reaching the maximum value. The axis of symmetry of the parabola curve in Figure 5.4 was defined as acting time t_a, which can be approximated by the time taken from the front of the slide touching the shoreline to the wave reaching its maximum height. Thus, $F_{p,x}$ can be expressed as:

$$F_{p,x} = \begin{cases} \frac{4F_{pmx}}{t_a^2} t(t_a - t) & 0 < t < t_a \\ 0 & x > t_a \end{cases} \tag{5.2}$$

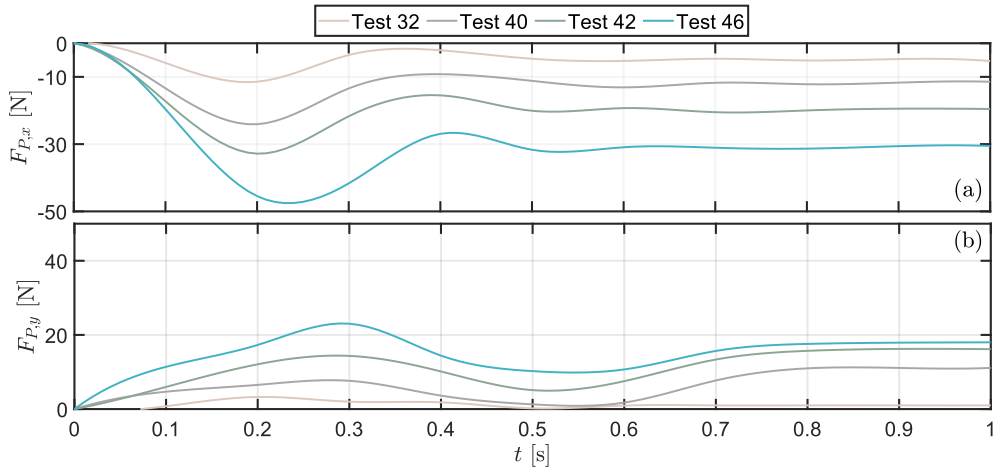

Figure 5.4 – Time variation of the hydrostatic force $\mathbf{F}_P$ acting on the slide phase: (a) horizontal projection $F_{p,x}$ and (b) vertical projection $F_{p,y}$.

where F_{pmx} is the maximum value of $F_{p,x}$. In this simplified equation, F_{pmx} and t_a were unknown. I then developed empirical equations for F_{pmx} and t_a by regressing with experimental data:

$$F_{pmx} = -25.4117 s_0^{0.4802} u_0^{1.0890} m_E^{0.3866} \tag{5.3}$$

$$t_a = 0.3579 s_0^{-0.0506} u_0^{0.2432} m_E^{0.0029} \tag{5.4}$$

Here, the slide thickness s_0, slide velocity u_0 at impact and the effective mass m_E have been routinely used to estimate wave characteristics. Figure 5.5 displays the measured and predicted maximum hydrostatic force in x-direction F_{pmx} and acting time t_a. The coefficient of determination R^2 was 0.884 for F_{pmx} and 0.875 for t_a, which means the F_{pmx} and t_a fitted well with Equations (5.3) and (5.4).

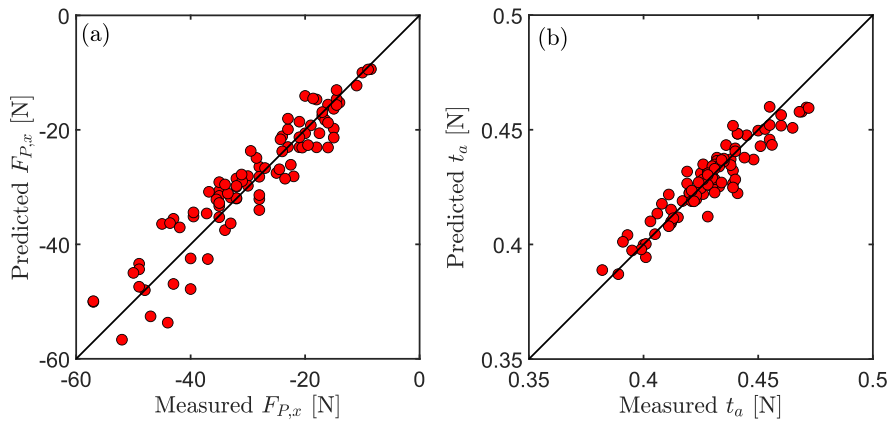

Figure 5.5 – Comparing the measured and predicted (a) F_{pmx} and (b) t_a.

Drag force

The drag force $\mathbf{F}_D$ mainly depends on the velocity difference between the slide material and the body of water. It is also influenced by many other factors, including the shape of the slide-water interface, the slide material's deformability, etc. Equation (3.12) displays the expression of $\mathbf{F}_D$. In the equation, the effective area of the slide-water interface A_f, the velocity of the submerged slide material $\bar{\mathbf{u}}_s$, and the water velocity $\bar{\mathbf{u}}_f$ are lacking.

As shown in Figure 5.6 (a) and (b), both the horizontal and vertical projection of the center of mass of the submerged slide material decreased from $t = 0.2$ s, showing the deformation of the submerged slide material. As the slide is deformable, the velocity at the frontal area is different from the mean velocity of the slide. As a simplification, I estimated the velocity of the two phases by their mean velocity in the control volume. Figure 5.6 (e) and (f) show the $x-$ and $y-$projection of the mean velocity of the submerged slide, respectively.

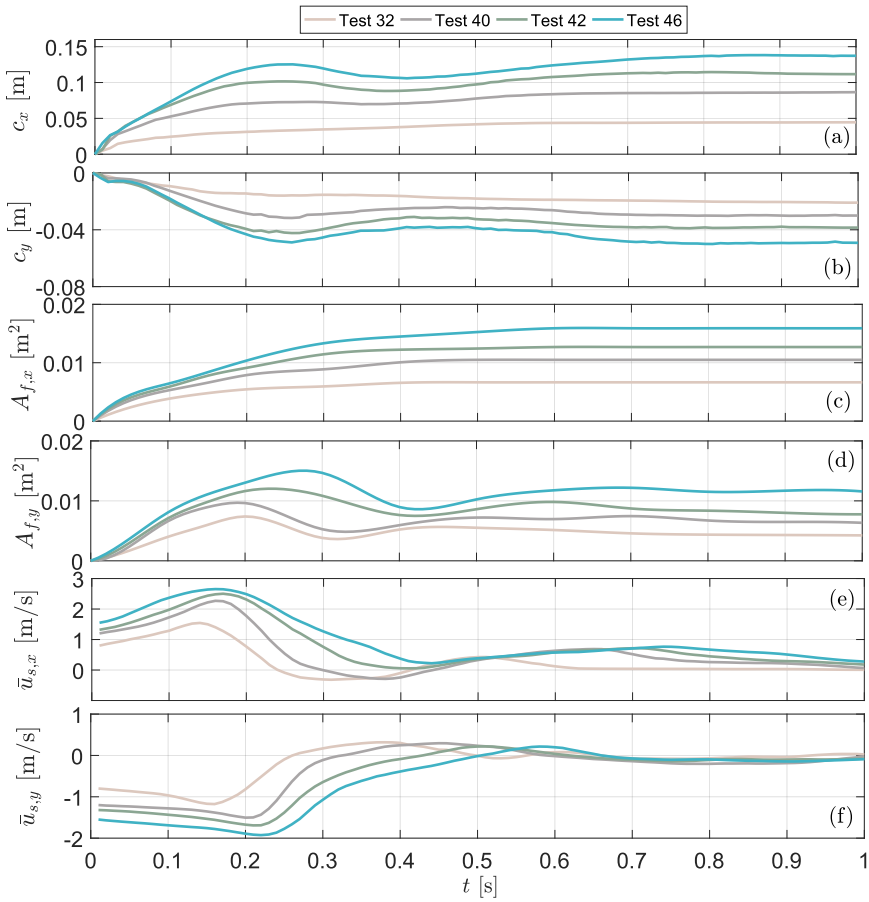

Figure 5.6 – Time variation of the horizontal and vertical projection of: the slide's center of mass (a) c_x and (b) c_y, the frontal area (c) A_x and (d) A_y, and the mean velocity of submerged mass (e) $\bar{u}_x$ and (f) $\bar{u}_x$.

Figure 5.6 (c) and (d) show the time variation of the horizontal and vertical projection of the

frontal area $A_{f,x}$ and $A_{f,y}$. I assumed the $x-$projection of the effective frontal area $A_{f,x}$ follows a parable function. Thus, $A_{f,x}$ can be approximated by:

$$A_{f,x} = \begin{cases} \frac{A_{fxm}}{t_a^2}(t-t_a)^2 + A_{fxm} & 0 < t < t_a \\ A_{fxm} & x > t_a \end{cases} \tag{5.5}$$

where A_{fxm} denotes the maximum value of $A_{f,x}$. The empirical equation of $A_{f,x}$ was obtained by regressed with experimental data using s_0, u_0 and m_E:

$$A_{fxm} = 0.0377 s_0^{0.9846} u_0^{0.0667} m_E^{0.0984} \tag{5.6}$$

Figure 5.7 compares the A_{fxm} measured from experiments and estimated with Equation (5.6). The coefficient of determination $R^2 = 0.891$.

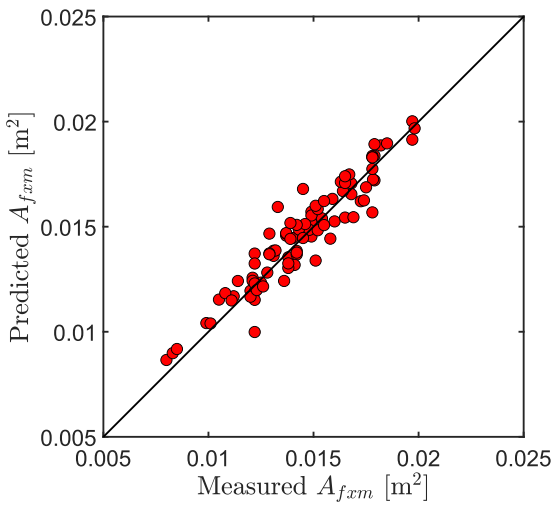

Figure 5.7 – Comparison of the measured and predicted A_{fxm}.

The velocity of the submerged slide material $\bar{\mathbf{u}}_s$ and the velocity of water in the control volume $\bar{\mathbf{u}}_f$ were unknown parameters not only in the drag force equation but also in the momentum balance equations. The horizontal mean velocity of the submerged slide $\bar{u}_s$ and water in the control volume $\bar{u}_f$ can be solved along with the momentum conservation equations.

5.2.2 Momentum variation

Figure 5.8 illustrates the momentum variations of the two phases in the observation window for the four selected tests. See Table 5.1 for the parameters of these four tests. For the momentum of both the slide phase p_s and the water phase p_f, the momentum variations in horizontal direction ($p_{s,x}$ and $p_{f,x}$) are significantly larger than those in vertical direction ($p_{s,y}$ and $p_{f,y}$).

Knowing the governing equations, boundary conditions (i.e., s_0, u_0, $\bar{u}_{f,r}$, η_r) and force applied

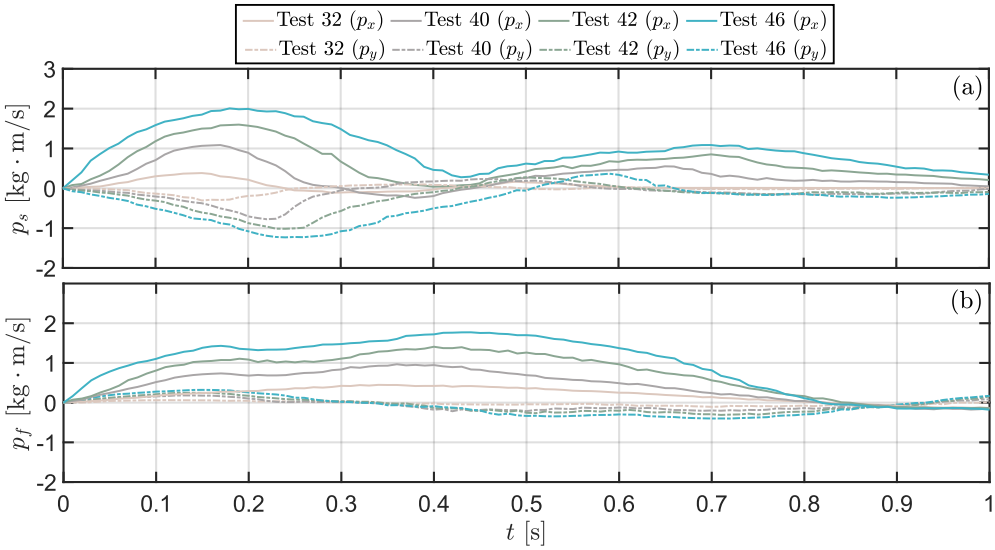

Figure 5.8 – Time variation of the momentum of the (a) slide phase p_s and (b) water phase p_f in the observation window.

on the control volume (i.e., $F_{D,x}$, $F_{P,x}$), we can obtain the momentum of the two phases in the control volume by solving Equations (3.5) to (3.9). Taking test 42 as an example, Figure 5.9 (a) and (b) compare the experimental slide momentum in the x-direction $p_{s,x}$ and water momentum in the x-direction $p_{f,x}$ with their theoretical data. The curves of both $p_{s,x}$ and $p_{f,x}$ fitted well with the theoretical results before they reach their maximum value (i.e., $t < 0.2$ s). The observed $p_{s,x}$ decreased much more sharply than the theoretical curve after $t = 0.2$ s, and had a slight rally from 0.4 to 0.6 s. From Figure 5.9 (c) and (d), it can be seen that, with different initial parameters, all the curves follow similar tendencies. $p_{s,x}$ increases during $0 < t < 0.2$ s, then begins decreasing. $p_{f,x}$ increases until $t = 0.4$ s.

5.2.3 Discussions

Deformation of the submerged slide

Figure 5.10 shows the moving direction of the mean velocity of the submerged slide material for the four selected tests. The time span between each marker is $\Delta t = 0.01$ s. It can be seen that the submerged slide material exhibits significant deformation after it has entered the body of water. The deformation of the slide material unavoidably affects the interaction forces between the slide material and the body of water. For example, both $F_{P,x}$ and $F_{D,x}$ depend greatly on the shape of the slide-water interface which is greatly influenced by the slide deformability.

Figure 5.11 illustrates how the submerged Carbopol is deformed during it intrudes into water. The deformation can be divided into four phases. First, the slide material intrudes into the body of water (phase i), and then it moves upwards due to the buoyancy effect (phases ii and

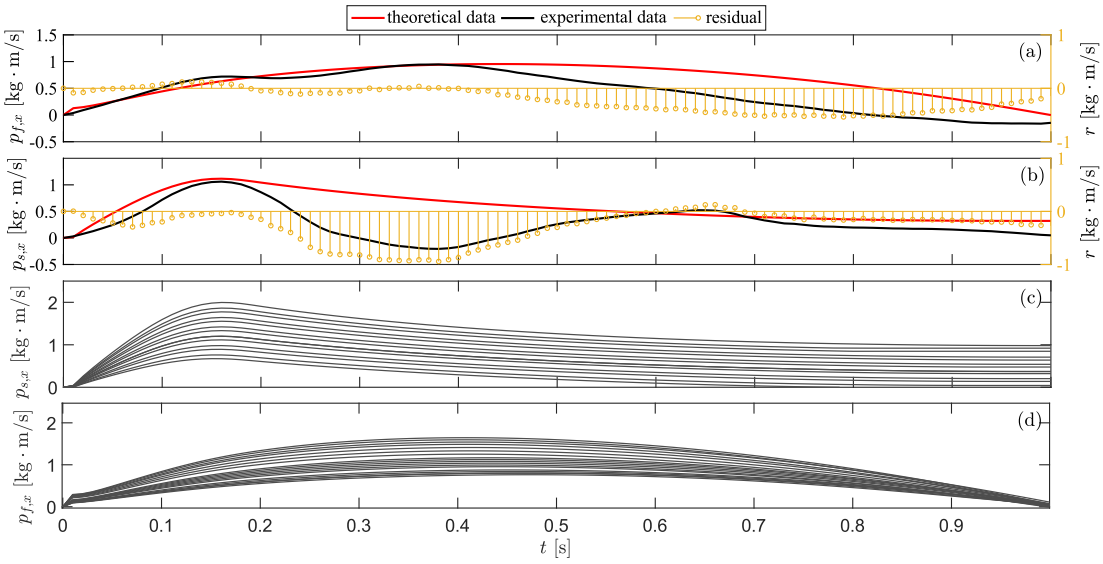

Figure 5.9 – Comparison of (a) $p_{s,x}$ and (b) $p_{f,x}$ obtained from experiments with the theoretical estimation (Test 42). Theoretical estimations of (c) $p_{s,x}$ and (d) $p_{f,x}$, with the initial settings $0.85 < l_s < 1.05$ m, $0.15 < s_g < 0.40$ m, $0.2 < l_0 < 0.4$ m, and $60 < \tau_c < 90$ Pa.

iii), before the slide material finally moves backward due to the water pressure (phase iv). We made simplifications for the expressions of both $F_{P,x}$ and $F_{D,x}$ in this study. The effect of deformation on the efficiency of momentum transfer was not considered due to these simplifications. It remains an open question as to how the deformability of the submerged slide affects the momentum transfer between slide and water.

Temporal wave characteristics

In addition to the interaction forces and momentum variations, the time series data of wave amplitude and wave height were measured from experiments. Figures 5.8 and 5.12 show that the wave amplitude and height follow similar tendencies as the momentum variations of the submerged sliding mass. Both reach their maximum values at approximately $t = 0.15$ s. This produces evidence that the time series data of wave characteristics are particularly reliant on the momentum variation of the slide phase. Further, if we look back at Figure 5.4, it is notable that the increasing stage of $F_{p,x}(t)$ is synchronous with the increasing stage of the wave amplitude $a(t)$. Thus, it would be interesting to provide insights into how the temporal wave characteristics depend on the slide momentum flux passing through the shoreline.

5.3 Prediction of temporal wave characteristics

In this section, I quantified the time series data of wave characteristics from the slide parameters. I first classified the experimental dataset into several groups using a *Gaussian*

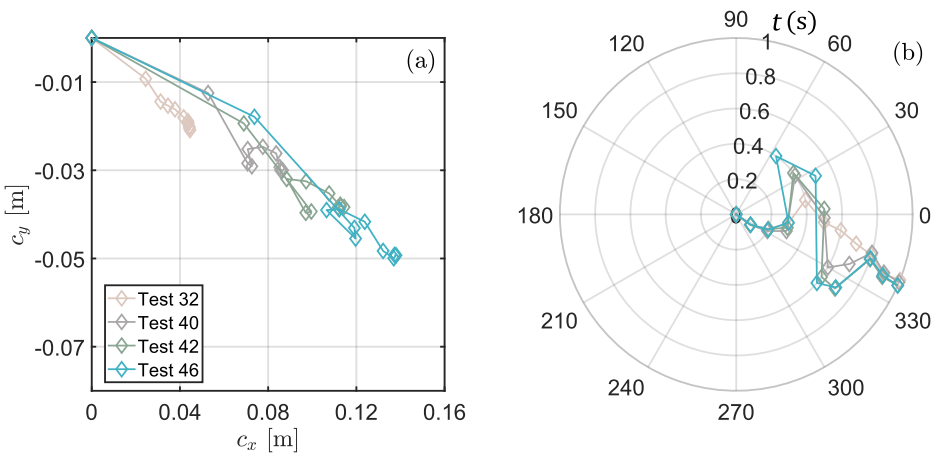

Figure 5.10 – Direction of the mean velocity of the submerged mass.

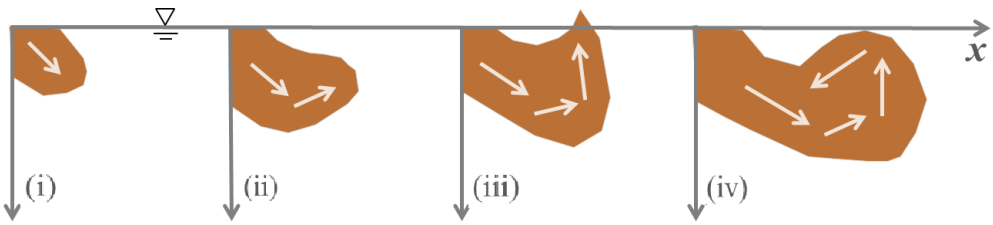

Figure 5.11 – Sketch of the deformation of the submerged slide mass.

mixture model, and then used a panel data model named *random coefficient model* to model the time series data. The principles of the Random coefficient model and the Gaussian mixture model have been presented in section 3.2.2.

5.3.1 Classification of the data samples

I used the 92 experiments conducted with the PIV system as the dataset to develop the model. Using the Gaussian mixture model, I classified the experimental dataset into several groups according to three dimensionless parameters: the slide Froude number Fr, scaled slide thickness S, and scaled effective slide mass M. Figure 5.13 (a) shows the results of the classification. There were 5 Classes in total: 14 experiments in Class 1, 9 experiments in Class 2, 30 experiments in Class 3, 30 experiments in Class 4, and 9 experiments in Class 5.

To verify whether the classification results well reflect the wave characteristics, I displayed the two dimensional distribution of the dataset of each class. Figure 5.14 (a) shows the ratio of the scaled maximum wave amplitude to the scaled maximum wave height A_m/H_m and the impulse product parameter P of all experiments. In addition to A_m/H_m, Figure 5.14 (b) and (c) display the A_m/L_m and H_m/L_m of all experiments. A_m/H_m, A_m/L_m, and H_m/L_m reflect the non-linearity of the impulse wave. The impulse product parameter P reflects the size of waves, as the wave characteristics can be regressed with P for most experiments (see Equation 4.1 for

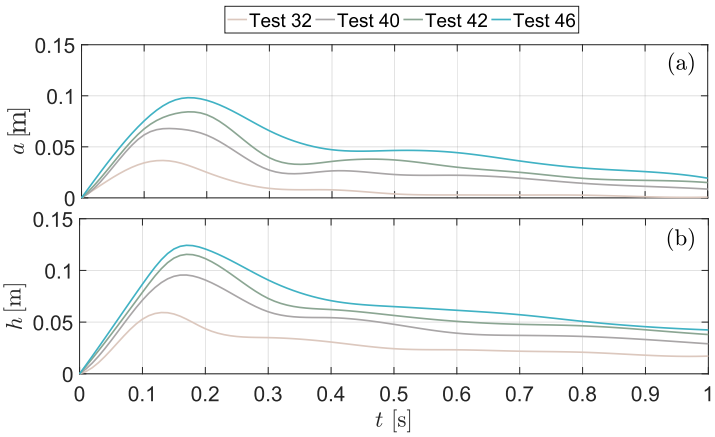

Figure 5.12 – Time variation of (a) wave amplitude $a(t)$ and (b) wave height $h(t)$.

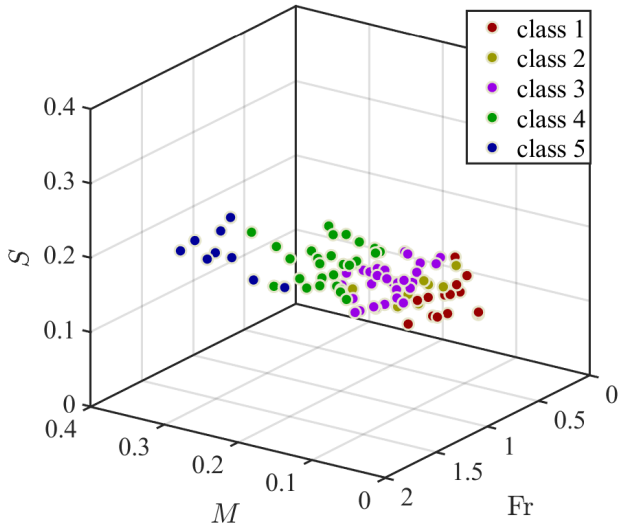

Figure 5.13 – (a) Classification results based on the evaluation criteria Fr, M and S.

details). It can be seen that the classification results based on S, M, and Fr not only reflect the nonlinearity of the waves but also reflects the size of the wave.

5.3.2 Predicting results

As discussed in section 5.2.3, the evolutions of the wave amplitude $a(t)$ and wave height $h(t)$ depend heavily on the momentum of the submerged slide in the x-direction $P_{s,x}$. Based on Equation (3.7), $P_{s,x}$ depends on the momentum flux crossing the shoreline, which can be quantified by the slide thickness on impact $s_0(t)$ and slide velocity on impact $u_0(t)$. Therefore, we may quantify $a(t)$ and $h(t)$ from $s_0(t)$ and $u_0(t)$. Further, as exhibited in section 3.1.2, $s_0(t)$ and $u_0(t)$ can be estimated from the initial settings of the experiments based on the kinematic wave model and lubrication model. The idea of this section is to determine how the time

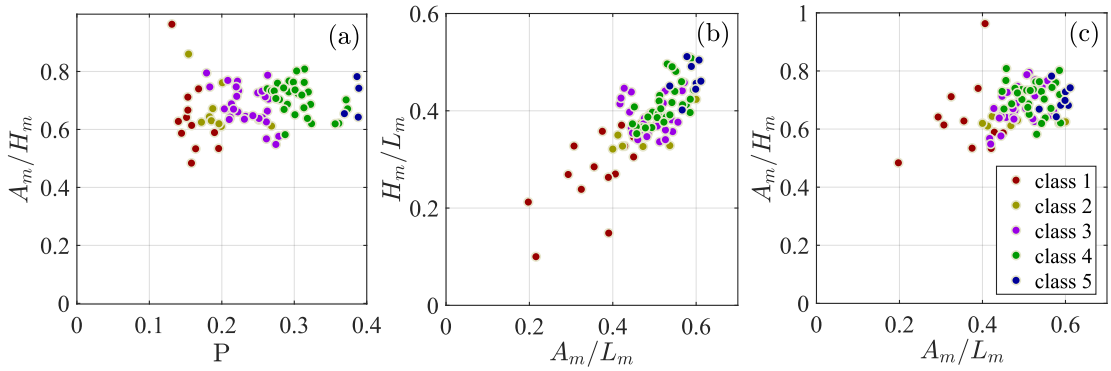

Figure 5.14 – Two dimensional distribution of experiments in each class: (a) P and A_m/H_m, (b) A_m/L_m and H_m/L_m, (c) A_m/L_m and A_m/H_m.

series data of wave characteristics depend on the slide parameters on impact, and how they depend on the initial settings of the experiments.

When predicting the maximum values of wave characteristics from the slide parameters on impact, three dimensionless parameters have been used: the slide Froude number Fr, the scaled thickness S, and the scaled effective mass M (see chapter 4). It is worth-noting that, according to the mass conservation Equation (3.5), the change rate of the submerged slide mass $\frac{dm_E}{dt}$ can be expressed by the thickness and velocity crossing the shoreline:

$$\frac{dm_E}{dt} = \rho_s B s_0(t) u_0(t) \tag{5.7}$$

where the slide density ρ_s and the width of the flume B are constants. This means that the time series data of the submerged slide mass $m_E(t)$ depend on the thickness and velocity of the sliding mass passing through the shoreline ($s_0(t)$ and $u_0(t)$). Therefore, I eliminated the mass term when quantifying the time series data of wave characteristics from slide parameters.

The same temporal dimensionless groups were used as in chapter 4: $A(t) = a(t)/h_0$, $S(t) = s_0(t)/h_0$, and $\mathrm{Fr}(t) = u_0(t)/\sqrt{gh_0}$. Then, time t was scaled as $T = t\sqrt{g/h_0}$. The objective is to estimate the scaled wave amplitude $A(t)$ from the scaled slide thickness on impact $S(t)$ and scaled Froude number $\mathrm{Fr}(t)$. Here, $a(t)$, $s_0(t)$ and $u_0(t)$ can be estimated from experiments.

For the panel data model, I used the random coefficient model, but other panel data models can also be applied to predict time series data. 82 of the 92 experiments were selected randomly to train the model, and the other 10 experiments were used to validate the model. I first quantified the scaled wave amplitude $A(T)$ with the $S(T)$ and $\mathrm{Fr}(t)$ recorded in experiments. Figure 5.15 shows the variation of the scaled wave amplitude A to the scaled time T for the 10 selected validation tests. I only considered the variation of wave amplitude for $t < 1$ s. The experimental and the predicted data of $A(T)$ were illustrated.

As presented in section 5.1, $s_0(t)$ and $u_0(t)$ can be given by the initial experimental settings

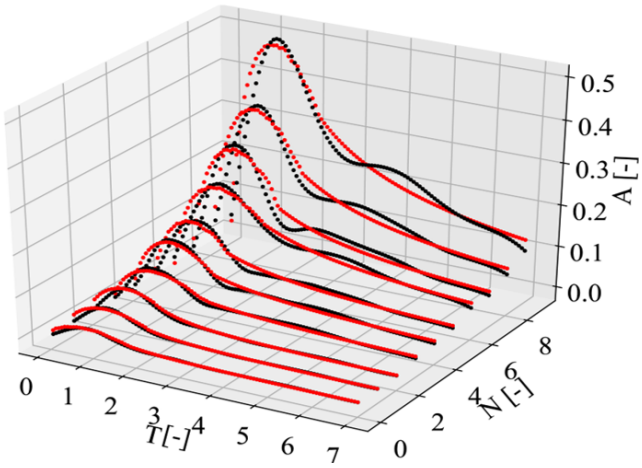

Figure 5.15 – The scaled wave amplitude A versus the scaled time T for the 10 validation tests ($N = 1, 2, ..., 10$). Black dots denote the experimental data and red dots are the predicted A.

based on the lubrication model and the kinematic wave model. I then quantified the wave amplitude with the theoretical approximations of $s_0(t)$ and $u_0(t)$. Table 5.2 shows the prediction accuracy of the two cases. One case predicted $A(T)$ using the $S(t)$ and $\mathrm{Fr}(t)$ given by experimental data, while the other predicted $A(T)$ with $S(t)$ and $\mathrm{Fr}(t)$ given by theoretical approximations. The performance of the prediction was evaluated by its coefficient of determination (R^2) and mean square error (MSE). See Equation (3.48) and (3.49) for the expressions of R^2 and MSE, respectively. The prediction precisions of both series of prediction were quite good, as R^2 of most selected tests were larger than 0.8. In addition, using experimental records of $s_0(t)$ and $u_0(t)$ leads to a better prediction accuracy than using the theoretical approximations of $s_0(t)$ and $u_0(t)$ to predict the time series data of wave amplitudes.

Table 5.2 – R^2 and MSE of the prediction for $s_0(t)$ and $u_0(t)$ given by experimental data (R^2_{EXP} and MSE_{EXP}) and given by theoretical approximation (R^2_{THE} and MSE_{EXP}).

Number	R^2_{EXP}	MSE_{EXP}	R^2_{THE}	MSE_{EXP}
1	0.9269	0.3265	0.8891	0.4022
2	0.9337	0.2729	0.9240	0.2923
3	0.9394	0.1959	0.8940	0.2045
4	0.9275	0.4637	0.9136	0.5062
5	0.9292	0.1350	0.9285	0.1358
6	0.9310	1.4901	0.9054	1.5489
7	0.9212	1.1769	0.8809	1.2515
8	0.8731	1.0479	0.8905	1.1765
9	0.9371	0.6429	0.9296	0.6804
10	0.9225	0.5428	0.9158	0.5658

Figure 5.16 shows the R^2_{THE} and R^2_{EXP} for the whole dataset. It can be seen that for most

experiments, the prediction accuracy of predicting $A(T)$ with giving $S(t)$ and $\mathrm{Fr}(t)$ by experimental data is better than giving $S(t)$ and $\mathrm{Fr}(t)$ by theoretical approximations.

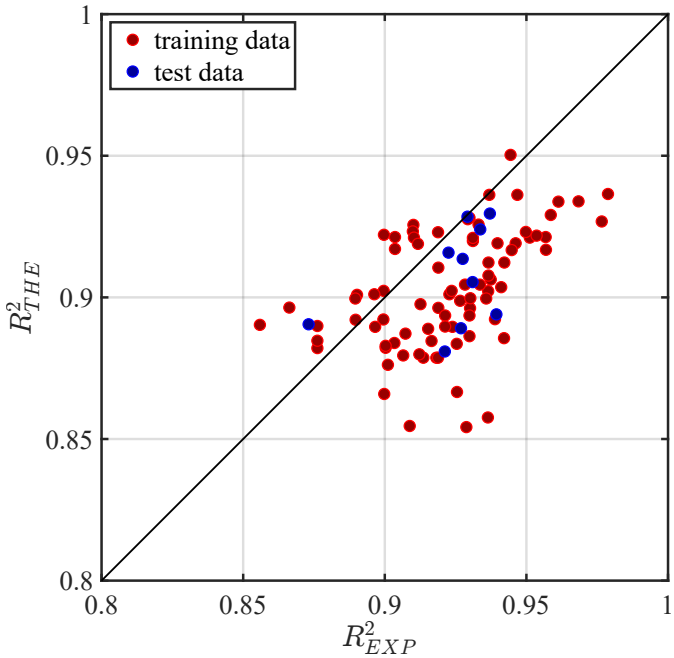

Figure 5.16 – Comparison of R^2_{THE} and R^2_{EXP} for the whole dataset.

5.3.3 Discussions

Momentum transfer rate

Section 4.2 found that waves generated by viscoplastic material are clearly larger than those created by granular slides with identical parameters (see Figures 4.5 and 4.6). I now discuss the effect of slide material's properties on wave generation from the view of momentum transfer rate. The time series response of wave amplitude $a(t)$ mainly relies on the momentum of the submerged slide material $p_s(t)$. As discussed in section 3.1.1, the change rate of p_s relies on two factors: (i) the momentum flux across the shoreline, which is dominated by $s_0(t)$ and $u_0(t)$; and (ii) the forces act on the slide phase, which contain $F_D(t)$ and $F_P(t)$.

Both blocks and viscoplastic slides are continuous fluids, whereas granular slides are non-continuous fluids. Due to the spaces among particles, for granular slides that have the same $s_0(t)$ and $u_0(t)$ as viscoplastic and block materials, its momentum flux crossing the shoreline is lower than blocks and viscoplastic slides. The momentum flux of continuous materials crossing the shoreline can be expressed by $dp = s_0 u_0 \mathbf{n} dt$. However, the momentum flux of granular materials should depreciate with a reduce factor, namely, $dp = r s_0 u_0 \mathbf{n} dt$, where r is the slide porosity. This point of view corresponds to a question that I have not answered in this thesis. I discussed the effect of slide cohesion by comparing waves generated by Carbopol

and water balls in section 4.2, however, I did not exclude the possibility of the slide porosity resulting to the difference in wave features.

Further, the mechanisms governing the impact of granular slides, viscoplastic slides, and blocks are different. For granular slides, the transfer of momentum in horizontal direction mainly relies on the drag force rather than the pressure force differences, as granular slides disperse into numerous particles once they enter into the body of water. Each particle is small and enters the body of water in a very short time, so the pressure differences in horizontal direction is negligible. The hydrostatic pressure (manifested as buoyancy force) in the vertical direction is balanced with the gravity force. For blocks and viscoplastic materials that move as a whole, the transfer of the momentum in horizontal direction is controlled by both the drag force and the pressure force differences.

6 Conclusions

This thesis provides insights to impulse waves generated by viscoplastic fluid. Experiments were conducted using a viscoplastic material called *Carbopol* and a granular material named *polymer-water balls*.

6.1 Concluding remarks

6.1.1 Impulse waves generated by viscoplastic fluid

A common problem among all experimental studies of landslide-generated waves is the choice of the material used for the sliding mass. To avoid the complication of work with real landslides, researchers often use simplified and idealized materials to study the behavior of natural landslides at the laboratory scale. Blocks and granular materials have been routinely used to mimic landslides. Many natural cohesive landslides such as snow avalanche, lava flow, and debris flow were considered as viscoplastic fluids when investigating their rheological behaviors. Numerical studies in the field of landslide-generated waves have used viscoplastic models, but none has applied viscoplastic material in experiments. This thesis took the first step toward experimental study of impulse waves generated by viscoplastic fluid. The originality of this thesis lies in its use of an artificial aqueous micro-gel called Carbopol Ultrez 10, whose rheological behavior can be described using the Herschel-Bulkley model. As a comparison, I also conducted experiments using a granular material called polymer-water balls, whose density is identical to that of Carbopol. The properties of the slide materials were presented in section 2.2.

6.1.2 Effect of slide material on wave characteristics

For most experiments using block or granular slides, the sliding masses entered water at high velocities in a very short period of time. Thus, the slide mass on impact was often considered the same as the initial mass of the slide material in the container box. Observations from high-speed cameras showed that Carbopol developed into a long and thin train of material

along the slope. Due to the long duration of the motion along the slope, only a portion of the sliding mass contributed to the first wave formation, and the leading wave decayed before the slide mass stopped moving. To quantify the characteristics of waves generated by viscoplastic fluid, the first question was how much of the initial slide mass is engaged in the leading wave formation. In section 4.1.2, I defined the slide's *effective mass* on the basis of the momentum conservation equations, defined as the immersed part's mass when the wave height reached its maximum. The effective mass increases with the increase of the initial slide mass and slope angle, and the decrease of the slope length and the yield stress of the slide material. The ratio of the effective mass to the initial slide mass ranged from 10 to 30 percent in our experiments (see Figure 4.3). Replacing the initial slide mass with the effective mass improves the prediction accuracies of empirical equations (see Figure 4.2).

The slide material's properties play a key part in the momentum transfer from the sliding mass to the body of water. The effect of slide deformability and porosity have been discussed by comparing waves generated by rigid blocks and granular materials, and comparing waves generated by granular slides with different diameters, respectively. In section 4.2, I studied the effect of slide material's cohesion by comparing experiments conducted with Carbopol (deformable and cohesive) and water balls (deformable and cohesionless). As shown in Figures 4.5 and 4.6, the wave heights and amplitudes created by the Carbopol gels were approximately 30 percent larger than those obtained using polymer-water balls. Thus, I deduced that slide cohesion does affect wave generation. In addition, the rheological behavior and deformability of Carbopol depended significantly on its concentration, but I noticed no significant effects of these concentrations on impulse wave features (see Figure 4.4). This turned out to be evidence that the effect of slide deformability on wave features is limited. It should be noted that we cannot exclude the effect of slide porosity from this limited set of experiments. In future studies, the results should be examined in parallel with earlier experiments that compared the effects of rigid blocks and granular slides on impulse wave formation.

Empirical equations in the form of power functions have been widely used to express wave parameters from slide parameters on impact. When different slide materials were involved, empirical equations have fit well with experimental data of one slide material, often exhibiting large deviations when being applied to dataset with other slide materials. None of the existing empirical equations can account for the full range of materials used in experiments. Also, applying empirical equations may be problematic if the slide material involves different components. Taking a viscoplastic–granular mixture as an example, the representative parameters of these two materials are the yield stress and grain diameter, respectively. Due to the current lack of understanding about how the materials properties affect the physical mechanism, integrating these two parameters into one equation might be problematic if we have presumed a functional form for that equation in advance. In section 4.3, I used the neural network method, one of the most commonly used data-driven methods, to integrate parameters of different categories of slide mass material into one model. The model was applied to a dataset of experiments conducted with Carbopol, water balls, and Carbopol-water balls mixtures. In contrast to empirical equations which presumed the

functional form with a constraint, the data-driven method predicted the wave characteristics purely from data. Of course, the disadvantage of a data-driven model is that it may suffer from a lack of interpretability, for example, the difficulty in explaining causal relationships between the data, the discrepancy, and the corresponding prediction. This reduces trust in the network relevance because of the lack of visual links between outputs, inputs and neurons.

6.1.3 Temporal analysis of the slide-water interaction

To develop universal predictive models considering the physical constraints, it is necessary to have a better understanding of how the sliding mass interacts with the body of water. There is a gap in experimental observations of the internal dynamics of the slide-water interaction, due to the difficulty of finding a slide material that can be traced using particle image velocimetry (PIV). Carbopol is transparent and can be easily seeded with tracing particles without changing the rheological properties, so that its internal velocity can be measured using PIV (see section 2.3.3). Owing to the use of Carbopol in the experiments, I measured the near-field velocity fields of both the submerged slide and the body of water at the same time (see section 2.5.2).

In section 3.1, I developed a theoretical model to analyze how the viscoplastic fluid interacts with the body of water, by combining Zitti et al. (2016) and Ancey et al. (2012). Following Zitti et al. (2016), I established governing equations based on the mass and momentum conservation equations of two-phase flow in a control volume. For the left boundary of the control volume, Zitti et al. (2016) considered the slide velocity passing through the shoreline as a constant and assumed the thickness by a parabolic function. The model was validated by experiments using granular slides. As the granular slide was replaced by viscoplastic fluid in this study, I provided the velocity and thickness of the sliding mass passing through the left boundary by the lubrication model and kinematic wave model (Ancey et al., 2012). With the support of the PIV technique, I determined the time series data of the interaction forces (that is, hydrostatic force and drag force) between the two phases experimentally, and then approximated the forces with empirical equations, thus completing the theoretical model (see section 5.2.1). The theoretical model quantified the time variation of the momentum of the two phases in the selected control volume, and thereby drawing the picture of how the momentum is transferred from a viscoplastic fluid to a body of water (see section 5.2.2).

I also noticed that the temporal prediction of the wave characteristics is lacking. Theoretical analysis indicated that the momentum exchange between the sliding mass and the body of water heavily relied on the momentum flux of the sliding mass passing the shoreline. In section 5.3, I proposed a statistical-theoretical combined model that can quantify the temporal variation of the wave amplitude from the initial parameters of the slide material in the container box. Using a random coefficient panel data model, I quantified how the temporal wave amplitude depends on the slide's thickness and depth-averaged velocity passing through the shoreline. Using the lubrication model and the kinematic wave model, the slide's momentum flux were expressed theoretically from the initial parameters. The

predictive model showed a good agreement with the experimental data.

6.2 Outlook

Some questions still remain unanswered. Future investigations will be continued in the following aspects:

- The present study only addressed the end-member case in which the materials' densities were close to that of water, and lower than most natural landslides. I was unable to find other materials whose properties are similar with those of Carbopol and water balls but with higher densities. Further investigations will be needed to gain additional insight into how the density affects the impulse wave formation.
- The effective mass was defined to quantify the actual slide mass acting on the leading wave generation, and it was applied to empirical equations and data-driven models. Even though the effective mass exhibits significant dependence with the initial parameters such as initial slide mass, slope length, and yield stress of the slide material, this thesis did not quantify the effective mass from these influential parameters quantitatively. It would be interesting to provide a quantitative expression for the effective mass in future studies.
- The role of slide cohesion in wave generation was discussed by comparing waves generated by viscoplastic slides and granular slides with the same density. However, from this limited set of experiments, the effect of slide porosity can not be excluded. A further comprehensive comparison should be conducted for blocks, viscoplastic slides with different yield stress, and granular slides with different diameters.
- With the help of the PIV technique, I observed the velocity field of the submerged sliding mass and the water body at the same time. The analysis of how the sliding mass interact with the body of water remains at a primary level. Many open questions remain concerning the internal dynamics of the slide-water interaction, such as how the slide properties affect the efficiency of momentum transfer, and how the water momentum depends on the slide momentum.

Bibliography

Abadie, S., Morichon, D., Grilli, S., and Glockner, S. (2010). Numerical simulation of waves generated by landslides using a multiple-fluid Navier–Stokes model. *Coastal Engineering*, 57(9):779–794.

Abraham, A. (2005). *Artificial neural networks: Handbook of measuring system design*. Wiley Online Library.

Ammann, W. (2000). *Der Lawinenwinter 1999: Ereignisanalyse*. Eidgenössisches Institut für Schnee-und Lawinenforschung.

Ancey, C. (2007). Plasticity and geophysical flows: A review. *Journal of Non-Newtonian Fluid Mechanics*, 142(1-3):4–35.

Ancey, C., Andreini, N., and Epely-Chauvin, G. (2012). Viscoplastic dambreak waves: review of simple computational approaches and comparison with experiments. *Advances in Water Resources*, 48:79–91.

Ancey, C. and Bates, B. M. (2017). Stokes' third problem for Herschel–Bulkley fluids. *Journal of Non-Newtonian Fluid Mechanics*, 243:27–37.

Ancey, C. and Cochard, S. (2009). The dam-break problem for Herschel–Bulkley viscoplastic fluids down steep flumes. *Journal of Non-Newtonian Fluid Mechanics*, 158(1-3):18–35.

Andreini, N., Epely-Chauvin, G., and Ancey, C. (2012). Internal dynamics of Newtonian and viscoplastic fluid avalanches down a sloping bed. *Physics of Fluids*, 24(5):053101.

Armaghani, D. J., Mohamad, E. T., Hajihassani, M., Abad, S. A. N. K., Marto, A., and Moghaddam, M. (2016). Evaluation and prediction of flyrock resulting from blasting operations using empirical and computational methods. *Engineering with Computers*, 32(1):109–121.

Ataie-Ashtiani, B. and Nik-Khah, A. (2008). Impulsive waves caused by subaerial landslides. *Environmental Fluid Mechanics*, 8(3):263–280.

Balmforth, N., Craster, R., Perona, P., Rust, A., and Sassi, R. (2007). Viscoplastic dam breaks and the Bostwick consistometer. *Journal of Non-Newtonian Fluid Mechanics*, 142(1-3):63–78.

Balmforth, N. J., Frigaard, I. A., and Ovarlez, G. (2014). Yielding to stress: Recent developments in viscoplastic fluid mechanics. *Annual Review of Fluid Mechanics*, 46:121–146.

Balmforth, N. J. and Provenzale, A. (2001). *Geomorphological fluid mechanics*. Springer Science & Business Media.

Bates, B. and Ancey, C. (2017). The dam-break problem for eroding viscoplastic fluids. *Journal of Non-Newtonian Fluid Mechanics*, 243:64–78.

Bates, B. M., Andreini, N., and Ancey, C. (2016). Basal entrainment by Newtonian gravity-driven flows. *Physics of Fluids*, 28(5):053101.

Bessette-Kirton, E., Allstadt, K., Pursley, J., and Godt, J. (2017). Preliminary analysis of satellite imagery and seismic observations of the Nuugaatsiaq landslide and tsunami, Greenland. *US Geological Survey-Landslide Hazards Program*.

Bolin, H., Yueping, Y., Xiaoting, C., Guangning, L., Sichang, W., and Zhibing, J. (2014). Experimental modeling of tsunamis generated by subaerial landslides: Two case studies of the Three Gorges Reservoir, China. *Environmental Earth Sciences*, 71(9):3813–3825.

Bonacucina, G., Martelli, S., and Palmieri, G. F. (2004). Rheological, mucoadhesive and release properties of Carbopol gels in hydrophilic cosolvents. *International Journal of Pharmaceutics*, 282(1-2):115–130.

Bonn, D., Denn, M. M., Berthier, L., Divoux, T., and Manneville, S. (2017). Yield stress materials in soft condensed matter. *Reviews of Modern Physics*, 89(3):035005.

Bullard, G., Mulligan, R., Carreira, A., and Take, W. (2019). Experimental analysis of tsunamis generated by the impact of landslides with high mobility. *Coastal Engineering*, 152:103538.

Chambon, G., Ghemmour, A., and Naaim, M. (2014). Experimental investigation of viscoplastic free-surface flows in a steady uniform regime. *Journal of Fluid Mechanics*, 754:332–364.

Chanson, H., Jarny, S., and Coussot, P. (2006). Dam break wave of thixotropic fluid. *Journal of Hydraulic Engineering*, 132(3):280–293.

Ciabatti, M. (1964). *La dinamica della frana del Vajont*. Museo geologico Giovanni Capellini.

Cochard, S. (2007). *Measurements of time-dependent free-surface viscoplastic flows down steep slopes*. PhD thesis, EPFL Lausanne.

Cochard, S. and Ancey, C. (2009). Experimental investigation of the spreading of viscoplastic fluids on inclined planes. *Journal of Non-Newtonian Fluid Mechanics*, 158(1-3):73–84.

Contreras, M. F., Diéguez, A. R., and Soriano, M. J. (2001). Rheological characterization of hydroalcoholic gels-15% ethanol-of Carbopol® Ultrez™ 10. *Il Farmaco*, 56(5-7):437–441.

Cremonesi, M., Frangi, A., and Perego, U. (2011). A lagrangian finite element approach for the simulation of water-waves induced by landslides. *Computers & Structures*, 89(11-12):1086–1093.

Dent, J. and Lang, T. (1983). A biviscous modified Bingham model of snow avalanche motion. *Annuals of Glaciology*, 4:42–46.

Dou, J., Yamagishi, H., Pourghasemi, H. R., Yunus, A. P., Song, X., Xu, Y., and Zhu, Z. (2015). An integrated artificial neural network model for the landslide susceptibility assessment of Osado Island, Japan. *Natural Hazards*, 78(3):1749–1776.

Engel, M., Oetjen, J., May, S. M., and Brückner, H. (2016). Tsunami deposits of the Caribbean towards an improved coastal hazard assessment. *Earth-Science Reviews*, 163:260–296.

Evers, F. (2017). *Spatial propagation of landslide generated impulse waves*. PhD thesis, ETH Zurich.

Evers, F. and Hager, W. (2015). Impulse wave generation: Comparison of free granular with mesh-packed slides. *Journal of Marine Science and Engineering*, 3(1):100–110.

Fernández-Nieto, E. D., Bouchut, F., Bresch, D., Diaz, M. C., and Mangeney, A. (2008). A new Savage–Hutter type model for submarine avalanches and generated tsunami. *Journal of Computational Physics*, 227(16):7720–7754.

Fresno, M., Ramırez, A., and Jiménez, M. (2002). Systematic study of the flow behaviour and mechanical properties of Carbopol® Ultrez™ 10 hydroalcoholic gels. *European Journal of Pharmaceutics and Biopharmaceutics*, 54(3):329–335.

Fresno, M. C., Ramírez, A. D., and Jiménez, M. S. (2001). Viscosity and temperature relationship in ethanol/water mixtures gelified with Carbopol Ultrez 10. *Farmaco (Societa Chimica Italiana: 1989)*, 56(5-7):443–445.

Freydier, P., Chambon, G., and Naaim, M. (2016). Internal dynamics of a free-surface viscoplastic flow down an inclined channel. *International Journal of Erosion Control Engineering*, 9(3):101–106.

Fritz, H., Hager, W. H., and Minor, H.-E. (2004). Near field characteristics of landslide generated impulse waves. *Journal of Waterway, Port, Coastal, and Ocean Engineering*, 130(6):287–302.

Fritz, H. M. (2002a). *Initial phase of landslide generated impulse waves*. PhD thesis, ETH Zurich.

Fritz, H. M. (2002b). PIV applied to landslide generated impulse waves. In *Laser techniques for fluid mechanics*, pages 305–320. Springer.

Fritz, H. M., Hager, W. H., and Minor, H.-E. (2003). Landslide generated impulse waves. *Experiments in Fluids*, 35(6):505–519.

Fritz, H. M., Hillaire, J. V., Molière, E., Wei, Y., and Mohammed, F. (2013). Twin tsunamis triggered by the 12 January 2010 Haiti earthquake. *Pure and Applied Geophysics*, 170(9-10):1463–1474.

Fritz, H. M., Mohammed, F., and Yoo, J. (2009). Lituya Bay landslide impact generated mega-tsunami 50th anniversary. In *Tsunami Science Four Years after the 2004 Indian Ocean Tsunami*, pages 153–175. Springer.

Fuchs, H. and Hager, W. H. (2015). Solitary impulse wave transformation to overland flow. *Journal of Waterway, Port, Coastal, and Ocean Engineering*, 141(5):04015004.

Gauthier, D., Anderson, S. A., Fritz, H. M., and Giachetti, T. (2018). Karrat fjord (Greenland) tsunamigenic landslide of 17 June 2017: Initial 3D observations. *Landslides*, 15(2):327–332.

Gedik, N. (2018). Least squares support vector mechanics to predict the stability number of rubble-mound breakwaters. *Water*, 10(10):1452.

Genevois, R. and Ghirotti, M. (2005). The 1963 vaiont landslide. *Giornale di Geologia Applicata*, 1(1):41–52.

Greeman, A. (2015). Norway's record tunnel. *World Highways/Routes du Monde*, 24(1).

Grilli, S. T., Grilli, A. R., David, E., and Coulet, C. (2016). Tsunami hazard assessment along the north shore of hispaniola from far-and near-field Atlantic sources. *Natural Hazards*, 82(2):777–810.

Gylfadóttir, S. S., Kim, J., Helgason, J. K., Brynjólfsson, S., Höskuldsson, Á., Jóhannesson, T., Harbitz, C. B., and Løvholt, F. (2017). The 2014 Lake Askja rockslide-induced tsunami: Optimization of numerical tsunami model using observed data. *Journal of Geophysical Research: Oceans*, 122(5):4110–4122.

Heller, V. (2007). *Landslide generated impulse waves: Prediction of near field characteristics*. PhD thesis, ETH Zurich.

Heller, V., Bruggemann, M., Spinneken, J., and Rogers, B. D. (2016). Composite modelling of subaerial landslide–tsunamis in different water body geometries and novel insight into slide and wave kinematics. *Coastal Engineering*, 109:20–41.

Heller, V., Chen, F., Brühl, M., Gabl, R., Chen, X., Wolters, G., and Fuchs, H. (2019). Large-scale experiments into the tsunamigenic potential of different iceberg calving mechanisms. *Scientific Reports*, 9(1):861.

Heller, V. and Hager, W. H. (2010). Impulse product parameter in landslide generated impulse waves. *Journal of Waterway, Port, Coastal, and Ocean Engineering*, 136(3):145–155.

Heller, V. and Hager, W. H. (2011). Wave types of landslide generated impulse waves. *Ocean Engineering*, 38(4):630–640.

Heller, V. and Hager, W. H. (2014). A universal parameter to predict subaerial landslide tsunamis? *Journal of Marine Science and Engineering*, 2(2):400–412.

Heller, V., Hager, W. H., and Minor, H.-E. (2008). Scale effects in subaerial landslide generated impulse waves. *Experiments in Fluids*, 44(5):691–703.

Heller, V., Hager, W. H., and Minor, H.-E. (2009). *Landslide generated impulse waves in reservoirs: Basics and computation.* Versuchsanstalt fur Wasserbau.

Heller, V. and Spinneken, J. (2013). Improved landslide-tsunami prediction: effects of block model parameters and slide model. *Journal of Geophysical Research: Oceans*, 118(3):1489–1507.

Heller, V. and Spinneken, J. (2015). On the effect of the water body geometry on landslide-tsunamis: Physical insight from laboratory tests and 2D to 3D wave parameter transformation. *Coastal Engineering*, 104:113–134.

Huber, A. (1980). *Schwallwellen in Seen als Folge von Felsstürzen.* PhD thesis, ETH Zurich.

Huber, A. and Hager, W. (1997). Forecasting impulse waves in reservoirs. In *Transactions of The International Congress on Large Dams*, volume 1, pages 993–1006.

Iverson, R. M. (1997). The physics of debris flows. *Reviews of Geophysics*, 35(3):245–296.

Iverson, R. M. and Vallance, J. W. (2001). New views of granular mass flows. *Geology*, 29(2):115–118.

Jing, H., Gao, Y., Liu, C., and Hou, J. (2020). Far-field characteristics of linear water waves generated by a submerged landslide over a flat seabed. *Journal of Marine Science and Engineering*, 8(3):196.

Kamphuis, J. and Bowering, R. (1970). Impulse waves generated by landslides. In *Coastal Engineering*, pages 575–588.

Kim, D. H. and Park, W. S. (2005). Neural network for design and reliability analysis of rubble mound breakwaters. *Ocean Engineering*, 32(11-12):1332–1349.

Kranzer, H. C. and Keller, J. B. (1959). Water waves produced by explosions. *Journal of Applied Physics*, 30(3):398–407.

Le Méhauté, B. and Wang, S. (1996). *Water waves generated by underwater explosion*, volume 10. World Scientific, Singapore.

Lee, A., Geem, Z. W., and Suh, K.-D. (2016). Determination of optimal initial weights of an artificial neural network by using the harmony search algorithm: application to breakwater armor stones. *Applied Sciences*, 6(6):164.

Lindstrøm, E. K. (2016). Waves generated by subaerial slides with various porosities. *Coastal Engineering*, 116:170–179.

Liu, J., Chang, H., Hsu, T., and Ruan, X. (2000). Prediction of the flow stress of high-speed steel during hot deformation using a bp artificial neural network. *Journal of Materials Processing Technology*, 103(2):200–205.

Liu, J., Zang, C., Tian, S., Liu, J., Yang, H., Jia, S., You, L., Liu, B., and Zhang, M. (2013). Water conservancy projects in China: achievements, challenges and way forward. *Global Environmental Change*, 23(3):633–643.

Luu, L.-H., Philippe, P., and Chambon, G. (2015). Experimental study of the solid-liquid interface in a yield-stress fluid flow upstream of a step. *Physical Review E*, 91(1):013013.

McFall, B. C. and Fritz, H. M. (2017). Runup of granular landslide-generated tsunamis on planar coasts and conical islands. *Journal of Geophysical Research: Oceans*, 122(8):6901–6922.

McFall, B. C., Mohammed, F., Fritz, H. M., and Liu, Y. (2018). Laboratory experiments on three-dimensional deformable granular landslides on planar and conical slopes. *Landslides*, 15(9):1713–1730.

Meng, Z. (2018). Experimental study on impulse waves generated by a viscoplastic material at laboratory scale. *Landslides*, 15(6):1173–1182.

Meng, Z. and Ancey, C. (2019). The effects of slide cohesion on impulse-wave formation. *Experiments in Fluids*, 60(10):151.

Miller, D. J. (1960). The Alaska earthquake of July 10, 1958: giant wave in Lituya Bay. *Bulletin of the Seismological Society of America*, 50(2):253–266.

Miller, G. S., Take, A. W., Mulligan, R. P., and McDougall, S. (2017). Tsunamis generated by long and thin granular landslides in a large flume. *Journal of Geophysical Research: Oceans*, 122(1):653–668.

Mohammed, F. and Fritz, H. M. (2012). Physical modeling of tsunamis generated by three-dimensional deformable granular landslides. *Journal of Geophysical Research: Oceans*, 117(C11).

Møller, P. C., Mewis, J., and Bonn, D. (2006). Yield stress and thixotropy: on the difficulty of measuring yield stresses in practice. *Soft Matter*, 2(4):274–283.

Müller, A., Dreyer, M., Andreini, N., and Avellan, F. (2013). Draft tube discharge fluctuation during self-sustained pressure surge: Fluorescent particle image velocimetry in two-phase flow. *Experiments in Fluids*, 54(4):1514.

Mulligan, R. P. and Take, W. A. (2017). On the transfer of momentum from a granular landslide to a water wave. *Coastal Engineering*, 125:16–22.

Noda, E. (1970). Water waves generated by landslides. *Journal of the Waterways, Harbors and Coastal Engineering Division*, 96(4):835–855.

Panizzo, A., De Girolamo, P., and Petaccia, A. (2005). Forecasting impulse waves generated by subaerial landslides. *Journal of Geophysical Research: Oceans*, 110(C12).

Poupardin, A., Heinrich, P., Frère, A., Imbert, D., Hébert, H., and Flouzat, M. (2017). The 1979 submarine landslide-generated tsunami in Mururoa, French Polynesia. *Pure and Applied Geophysics*, 174(8):3293–3311.

Ruffini, G., Heller, V., and Briganti, R. (2019). Numerical modelling of landslide-tsunami propagation in a wide range of idealised water body geometries. *Coastal Engineering*, 153:103518.

Santiago, J. G., Wereley, S. T., Meinhart, C. D., Beebe, D., and Adrian, R. J. (1998). A particle image velocimetry system for microfluidics. *Experiments in Fluids*, 25(4):316–319.

Skvortsov, A. and Bornhold, B. (2007). Numerical simulation of the landslide-generated tsunami in Kitimat Arm, British Columbia, Canada, 27 April 1975. *Journal of Geophysical Research: Earth Surface*, 112(F2).

Suzuki, K. (2013). *Artificial neural networks: Architectures and applications*. BoD–Books on Demand.

Swamy, P. A. (1970). Efficient inference in a random coefficient regression model. *Econometrica: Journal of the Econometric Society*, 38(2):311–323.

Tang, G., Lu, L., Teng, Y., Zhang, Z., and Xie, Z. (2018). Impulse waves generated by subaerial landslides of combined block mass and granular material. *Coastal Engineering*, 141:68–85.

Viroulet, S., Cébron, D., Kimmoun, O., and Kharif, C. (2013). Shallow water waves generated by subaerial solid landslides. *Geophysical Journal International*, 193(2):747–762.

Walder, J. S., Watts, P., Sorensen, O. E., and Janssen, K. (2003). Tsunamis generated by subaerial mass flows. *Journal of Geophysical Research: Solid Earth*, 108(B5).

Watts, P. (1997). *Water waves generated by underwater landslides*. PhD thesis, California Institute of Technology, Los Angeles.

Yavari-Ramshe, S. and Ataie-Ashtiani, B. (2016). Numerical modeling of subaerial and submarine landslide-generated tsunami waves-recent advances and future challenges. *Landslides*, 13(6):1325–1368.

Yavari-Ramshe, S. and Ataie-Ashtiani, B. (2017). A rigorous finite volume model to simulate subaerial and submarine landslide-generated waves. *Landslides*, 14(1):203–221.

Yavari-Ramshe, S. and Ataie-Ashtiani, B. (2019). On the effects of landslide deformability and initial submergence on landslide-generated waves. *Landslides*, 16(1):37–53.

Yegnanarayana, B. (2009). *Artificial neural networks*. PHI Learning Pvt. Ltd.

Zhao, L., Mao, J., Bai, X., Liu, X., Li, T., and Williams, J. (2016). Finite element simulation of impulse wave generated by landslides using a three-phase model and the conservative level set method. *Landslides*, 13(1):85–96.

Zitti, G., Ancey, C., Postacchini, M., and Brocchini, M. (2015). Impulse waves generated by snow avalanches falling into lakes. In *Proceedings of the 36th IAHR World Congress*.

Zitti, G., Ancey, C., Postacchini, M., and Brocchini, M. (2016). Impulse waves generated by snow avalanches: Momentum and energy transfer to a water body. *Journal of Geophysical Research: Earth Surface*, 121(12):2399–2423.

Zitti, G., Ancey, C., Postacchini, M., and Brocchini, M. (2017). Snow avalanches striking water basins: Behaviour of the avalanche's centre of mass and front. *Natural Hazards*, 88(3):1297–1323.

Zweifel, A. (2004). *Impulswellen: Effekte der Rutschdichte und der Wassertiefe*. PhD thesis, ETH Zurich.

Zweifel, A., Hager, W. H., and Minor, H.-E. (2006). Plane impulse waves in reservoirs. *Journal of Waterway, Port, Coastal, and Ocean Engineering*, 132(5):358–368.

Notation

Global variables

Alphabetical symbols

a	wave amplitude
a_m	maximum wave amplitude
A_f	cross-sectional area of the slide interface
$A_{f,x}$	horizontal projection of A_f
A_{fxm}	the maximum value of $A_{f,x}$
A_s	area of the slide-water interface
B	width of the flume
B_i	Bingham number
c	concentration of Carbopol
C	phase speed of water
C_d	drag coefficient
(c_x, c_y)	coordinates of the center of mass of the submerged slide material
d_g	diameter of a granular particle
D_s	scaled diameter of the granular slide
Fr	slide Froude number
$\mathbf{F}$	force applied on the control volume
$\mathbf{F}_D$	drag force applied on the submerged slide material
$\mathbf{F}_P$	hydrostatic force applied on the submerged slide material
$F_{D,x}$	horizontal projection of $\mathbf{F}_D$
$F_{P,x}$	horizontal projection of $\mathbf{F}_P$
$F_{D,y}$	vertical projection of $\mathbf{F}_D$
$F_{P,y}$	vertical projection of $\mathbf{F}_P$
g	gravity acceleration
h	wave height
h_0	still water depth
h_m	maximum wave height
h_{sf}	vertical distance between the surface of the slide phase to the water surface
l_0	initial length of the slide material

l_s	slope length
M	scaled effective mass
m_I	initial slide mass
m_E	effective slide mass
$\mathbf{n}$	normal vector
n	power-law index that reflects the shear thinning
P	impulse product parameter
R^2	coefficient of determination
s_0	slide thickness on impact
s_g	initial slide depth at the lock gate
S	scaled slide thickness
$s(\hat{x}, \hat{t})$	thickness of the sliding mass moving along the slope
S_r	surface of the outgoing flow at the right boundary of the control volume
s_c	critical flow depth of the slide material
R_P	Pearson correlation coefficient
R_V	volume ratio of viscoplastic material in granular-viscoplastic mixtures
t	time
T	scaled time
$\hat{t}$	time
t_a	acting time
u_0	slide velocity on impact
$u(\hat{x}, \hat{t})$	stream-wise velocity of the sliding mass moving along the slope
$\bar{\mathbf{u}}_s$	volume-averaged velocity of the slide phase
$\bar{\mathbf{u}}_f$	volume-averaged velocity of the water phase
$\bar{u}_s$	horizontal projection of $\bar{\mathbf{u}}_s$
$\bar{u}_f$	horizontal projection of $\bar{\mathbf{u}}_f$
$\bar{u}_{f,r}$	horizontal depth-averaged water velocity at the right boundary of the control volume
V	control volume
$\bar{v}_s$	vertical projection of $\bar{\mathbf{u}}_s$
$\bar{v}_f$	vertical projection of $\bar{\mathbf{u}}_f$
$\bar{v}_{f,r}$	vertical depth-averaged water velocity at the right boundary of the control volume
V_s	volume of slide phase in the control volume
V_f	volume of water phase in the control volume
V_I	initial volume of the slide material
V_E	effective slide volume
V_S	volume of the submerged slide material
(x, y)	coordinate system
$(\hat{x}, \hat{y})$	coordinate system
Y_0	position of the yield surface

Greek symbols

α_s	fraction of the volume occupied by the slide phase
α_f	fraction of the volume occupied by the water phase
μ	consistency
$\dot{\gamma}$	shear rate
η	free-water surface elevation
η_r	water surface elevation at the right boundary of the control volume
θ	slope angle
Π_1	scaled effective mass
Π_2	scaled slide thickness
ρ_f	water density
ρ_s	slide density
τ	shear stress
τ_c	yield stress

Abbreviations

ANN	artificial neural network
MSE	mean square error
PIV	p
SSE	sum of squares

Local variables in Section 3.2.1

Local variables are merely defined and used in a local Section.

Alphabetical symbols

E	residual between expected and actual output values
e_k	residual of each output node
f	activation function
r	number of iterations
t_k	predefined target value
W	weighting matrix
w	weighting
x	input variables
x_i	input layer
X_j	temporal computing results of input layers before using the activation function
X	raw data
Y	normalized data
y_i	hidden layer
$y_{p,i}$	predicted data

$y_{o,i}$	observed data
$\bar{y}_0$	average of the observed data
Y_k	temporal computing results of hidden layers before using the activation function
z_i	output layer
$\hat{z}$	output variables
z	expected output variables

Greek symbols

β	bias vector
Δw_{jk}	weighting adjustment
η	learning rate
ϵ	number of experiment

Local variables in Section 3.2.2

Alphabetical symbols

i	serial number of data's dimension
k	explanatory variable index
k_n	unknown class tag for nth test
N	number of the cross-sectional panel
n	serial number of data sequence
P	posterior probability
p_k	kth prior probability
S_{ni}	ith parameter at time n of the slide
t	time
T	test number in each panel
u	random interference term
W_{nj}	jth parameter at time n of the wave
x_{kit}	explanatory variable
$x-y$	data panel
y_{it}	cross-sectional data in a data panel

Greek symbols

β	common mean coefficient vector
$\hat{\beta}_{GLS}$	effective estimation of β
γ	an operator from individual data to the common mean value
μ_k	mean value of Gaussian distribution
π_k	weighting
σ	variance of Gaussian distribution

MENG Zhenzhu

D.O.B: 17/11/1990
Email: zhenzhu.meng@epfl.ch
Language: Chinese, English, French
Address: EPFL-ENAC-LHE, Station 18, CH-1015 Lausanne, Switzerland

EDUCATION

09.2015-05.2020	**École Polytechnique Fédérale de Lausanne, Switzerland** Phd student at the Environmental Hydraulics Laboratory Supervisor: Christophe Ancey
10.2013-06.2015	**Hohai University, China** Master's degree in Water Conservancy and Hydropower Engineering
03.2011-09.2013	**Ecole des Mines de Douai, France** Engineer's degree in Energy Engineering
09.2008-03.2011	**Hohai University, China** Bachelor's degree in Geographic Information System

EMPLOYMENT HISTORY

07.2015-09.2015	**Yellow River Conservancy Commission, China**
intern	Analysis of the water discharge of Yellow River
05.2014-10.2014	**China Academy of Urban Planning & Design, China**
intern	Analysis of the terrain utilization
03.2013-09.2013	**Maia Eolis, Lille, France**
intern	Analysis of the energy consumption in buildings
05.2012-09.2012	**Renault, Factory at Douai, France**
intern	Feasibility analysis of the surplus heat recovery of a boiler
07.2011-08.2011	**City Hall of Douai, France**
intern	Assistance with fieldworks

TEACHING ASSISTANT at EPFL

Master Courses: Hydraulics (3 credits), Statistical hydrology (3 credits)
Bachelor Course: Fluid Mechanics (5 credits)
Supervised 8 masters and 2 bachelors semester projects (17 students in total)
Supervised 1 research internship

PERSONAL SKILLS

Familiar with *MATLAB*, *VB*, *Python*, C
Familiar with image processing, machine learning algorithm programming, and software development

Research output list

Publications

1. **Meng, Z.**, Hu, Y., & Ancey, C. (2020). Using a data driven approach to predict waves generated by gravity driven mass flows. *Water*, 12(2), 600.

2. **Meng, Z.**, & Ancey, C. (2019). The effects of slide cohesion on impulse-wave formation. *Experiments in Fluids*, 60(10), 151.

3. **Meng, Z.** (2018). Experimental study on impulse waves generated by a viscoplastic material at laboratory scale. *Landslides*, 15(6), 1173-1182.

Conference proceedings

1. **Meng, Z.**, Ancey, C., & Maeder, I. (2020). Experimental study on tsunamis generated by landslides. EGU General Assembly, Vienna, Austria.

2. **Meng, Z.**, & Ancey, C. (2019). The effects of slide cohesion on impulse waves generated by landslides. 17th Swiss Geoscience Meeting, Fribourg, Switzerland. (oral presentation)

3. **Meng, Z.**, Hu, Y., & Ancey, C. (2019). Viscoplastic fluid impacting a body of water: predicting wave features from the fluid properties. VPF8 Viscoplastic Fluids: from Theory to Application, Cambridge, UK. (oral presentation)

4. **Meng, Z.**, & Ancey, C. (2018). Experimental study of viscoplastic avalanches striking a water body using PIV techniques. EGU General Assembly, Vienna, Austria. (PICO presentation)

5. **Meng, Z.**, & Ancey, C. (2018). Experimental comparison of tsunami generated by viscoplastic and granular slides. EGU General Assembly, Vienna, Austria. (poster)